

Abstract

Title of Thesis: Shock-Based Waverider Design with Pressure Corrections, and Computational Simulations

Marie-Laure Chauffour, Master of Science, 2004

Thesis Directed By: Professor Mark J. Lewis
Department of Aerospace Engineering

Waveriders demonstrate good aerodynamic performance and thus are of special interest for hypersonic applications, especially for engine-airframe integration. The osculating cones waverider method is a generic shock-based derived waverider design method that allows prescribing a wide variety of flowfields at the inlet of the engine of the hypersonic vehicle. Previous osculating cones waveriders methods assumed that along the streamlines within the waverider shock layer, the pressure gradients in the azimuthal direction were negligible, and thus neglected it into the design process. The focus of this work is to investigate the magnitude of those pressure gradients, and integrate those into a new osculating cones waverider design method by modifying the derivation of the lower surface (streamsurface). The geometries resulting from the design code are to be compared with the previous solutions. The flowfield and aerodynamic performance predicted by the design code are compared with the results from Computational Fluid Dynamics simulations.

Shock-Based Waverider Design with Pressure Gradient Corrections and
Computational Simulations

By

Marie-Laure Chauffour

Thesis submitted to the Faculty of the Graduate School of the
University of Maryland, College Park, in partial fulfillment
of the requirements for the degree of
Master of Science
2004

Advisory Committee:

Professor Mark J. Lewis, Chairman/ Advisor
Assistant Professor James D. Baeder
Visiting Professor Robert H. Korkegi

© Copyright by
Marie-Laure Chauffour
2004

Acknowledgements

I would want firstly to address a special thanks to Dr. Ryan Starkey which helped me all along my research with a good deal of advice and motivation support. I am also grateful to my advisor, Dr. Mark Lewis for his encouragement and technical support throughout this work.

To my family and my friends, without whose support this work could not have been done, I am grateful to you to be there for the good times as well as the bad times.

I will not forget of course all the people from my lab and others: you have made those two years a rich human experience.

I dedicate that work to my grandparents; you will always be by my side.

Table of Contents

Acknowledgements	ii
Table of Contents.....	iii
List of Tables	v
Introduction.....	1
1.1 Motivation	1
1.2 Previous Work.....	2
1.2.1 Waverider Concept	2
1.2.1 Waverider Validation.....	6
1.3 Present Work	8
Shock-Based Waverider Design	10
2.1 Waverider Design	10
2.1.1 Waverider Concept	10
2.1.2 Shock-Based Inverse Waverider Design.....	11
2.1.3 Wedge-Derived Waveriders.....	13
2.1.4 Cone-Derived Waveriders.....	14
2.1.5 Osculating Cones Waveriders.....	19
2.2 Present Osculating Cones Waverider Design.....	22
2.2.1 Prescribed Parameters.....	22
2.2.2 Leading Edge, Shockwave and Upper Surface Derivation.....	25
2.2.4 Pressure Gradients Corrections	28
2.2.5 Lower Surface Derivation.....	29
2.2.6 Comparison of Waverider Geometries for Corrected and Uncorrected Osculating Cones Waverider Method.....	30
Hypersonic On-Design Performances.....	36
3.1 Hypersonic Performances Prediction.....	36
3.2 Computational Method	38
3.2.1 Numerical Method	38
3.2.2 Computational grid.....	38
3.2.3 Boundary conditions and initial conditions.....	41

3.2.4	Solutions convergence criteria	41
3.3	CFD Simulations	43
3.3.1	Wedge-Derived Waverider M=6.....	43
3.3.2	Cone-Derived Waverider M=6.....	46
3.3.3	Osculating Cones Waverider M=3.....	54
3.3.4	Osculating Cones Waverider M=6.....	62
3.3.5	Osculating Cones Waverider M=10.....	70
3.3.6	Osculating Cones Waverider M=15.....	78
	Summary and Conclusions	85
	Appendix A.....	88

List of Tables

3.1 Design conditions of a Mach 6 waverider	43
3.2 Aerodynamic performance of a Mach 6 waverider	46
3.3 Design conditions of a Mach 6 waverider	46
3.4 Comparison of aerodynamic performance of a Mach 6 waverider, Euler simulation	50
3.5 Comparison of aerodynamic performance of a Mach 6 waverider, Navier-Stokes simulation	53
3.6 Design conditions of a Mach 3 waverider	54
3.7 Comparison of aerodynamic performance of a Mach 3 waverider with lower surface corrected for pressure-gradients	62
3.8 Comparison of aerodynamic performance of a Mach 3 waverider with lower surface non-corrected for pressure-gradients	62
3.9 Design conditions of a Mach 6 waverider	63
3.10 Aerodynamic performance comparison of a Mach 6 waverider with lower surface corrected for pressure gradients	69
3.11 Aerodynamic performance comparison of a Mach 6 waverider with lower surface non-corrected for pressure gradients	70
3.12 Design conditions of Mach 10 osculating cones waverider	70
3.13 Aerodynamic performance of Mach 10 waverider with lower surface corrected for pressure gradients	77
3.14 Aerodynamic performance of Mach 10 waverider with lower surface non-corrected for pressure gradients	77
3.15 Design conditions of Mach 15 waverider	78

3.16 Aerodynamic performance of Mach 15 waverider with lower surface corrected for pressure gradients	83
3.17 Aerodynamic performance of Mach 15 waverider with lower surface non-corrected for pressure gradients	84

List of Figures

1.1 Nonweiler caret waverider prescribed geometry, planform view	3
1.2 Nonweiler caret waverider	4
1.3 Mach 6 osculating cones waverider wind tunnel model	7
2.1 Waverider geometry derivation from generating flowfield	12
2.2 Mach 6 wedge-derived waverider	14
2.3 Mach 6 cone-derived waverider	19
2.4 Waverider design methods relationships	20
2.5 Osculating cones in the base plane	21
2.6 Prescribed shock wave profile curve and upper surface profile curve geometry in the base plane	24
2.7 Osculating cone derivation, base plane	26
2.8 Osculating cones waverider design in a local osculating plane	26
2.9 Mach 3 osculating cones waverider	32
2.10 Mach 6 osculating cones waverider	33
2.11 Mach 10 osculating cones waverider	34
2.12 Mach 15 osculating cones waverider	35
3.1 Surface elements for force and area calculation	36
3.2 Computational grid in the base plane	39
3.3 Magnified grid near sharp leading edge	39
3.4 Computational grid, top view	40
3.5 Computational grid, bottom view	40
3.6 Boundary conditions, front view of the computational grid	42
3.7 Boundary conditions, rear view of the computational grid	42
3.8 Mach 6 wedge-derived waverider	44

3.9 Comparison of normalized pressure contours over Mach 6 waverider	45
3.10 Mach 6 cone-derived waverider	47
3.11 Comparison of normalized pressure contours over Mach 6 waverider, Euler simulation	48
3.12 Comparison of normalized pressure contours over lower surface of Mach 6 waverider, Euler simulation	49
3.13 Comparison of normalized pressure contours over Mach 6 waverider, base plane, Euler simulation	49
3.14 Comparison of normalized pressure contours over Mach 6 waverider, Euler simulation	50
3.15 Comparison of normalized pressure contours over Mach 6 waverider, Navier-Stokes simulation	51
3.16 Comparison of normalized pressure contours over lower surface of Mach 6 waverider, Navier-Stokes simulation	52
3.17 Comparison of normalized pressure contours over Mach 6 waverider, base plane, Navier-Stokes simulation	52
3.18 Comparison of normalized pressure contours over Mach 3 waverider	55
3.19 Comparison of normalized pressure contours over Mach 3 modified waverider, base plane	56
3.20 Comparison of normalized pressure contours over Mach 3 non-modified waverider, base plane	56
3.21 Comparison of azimuthal velocity contours over Mach 3 modified waverider, base plane	58
3.22 Comparison of azimuthal velocity contours over Mach 3 non-modified waverider, base plane	58
3.23 Comparison of normalized pressure contours over lower surface of Mach 3 modified waverider	59

3.24 Comparison of normalized pressure contours over lower surface of Mach 3 non-modified waverider	59
3.25 Streamlines at the lower surface of a Mach 3 waverider	60
3.26 Comparison of normalized pressure contours over Mach 6 modified waverider	64
3.27 Comparison of normalized pressure contours over Mach 6 modified waverider, base plane	64
3.28 Comparison of normalized pressure contours over Mach 6 non-modified waverider, base plane	64
3.29 Comparison of azimuthal velocity contours over Mach 6 modified waverider, base plane	65
3.30 Comparison of azimuthal velocity contours over Mach 6 non-modified waverider, base plane	65
3.31 Comparison of normalized pressure contours over lower surface of Mach 6 modified waverider	66
3.32 Comparison of normalized pressure contours over lower surface of Mach 6 non-modified waverider	67
3.33 Streamlines at the lower surface of a Mach 6 waverider	68
3.34 Comparison of normalized pressure gradients over Mach 10 waverider	71
3.35 Comparison of normalized pressure contours, base plane of Mach 10 modified waverider	72
3.36 Comparison of normalized pressure contours, base plane of Mach 10 non-modified waverider	72
3.37 Comparison of azimuthal velocity contours over Mach 10 modified waverider, base plane	73
3.38 Comparison of azimuthal velocity contours over Mach 10 non-modified waverider, base plane	73

3.39 Comparison of normalized pressure contours over lower surface of Mach 10 modified waverider	74
3.40 Comparison of normalized pressure contours over lower surface of Mach 10 non-modified waverider	75
3.41 Streamlines at the lower surface of a Mach 10 waverider	76
3.42 Comparison of normalized pressure contours over Mach 15 waverider	79
3.43 Comparison of normalized pressure contours over Mach 15 modified waverider, base plane	80
3.44 Comparison of normalized pressure contours over Mach 15 non-modified waverider, base plane	80
3.45 Comparison of azimuthal velocity contours over Mach 15 modified waverider, base plane	81
3.46 Comparison of azimuthal velocity contours over Mach 15 non-modified waverider, base plane	81
3.47 Comparison of normalized pressure contours over lower surface of Mach 15 modified waverider	82
3.48 Comparison of normalized pressure contours over lower surface of Mach 15 non-modified waverider	82

List of Symbols

A_w	= wetted area
D	= drag
C_D	= drag coefficient
C_L	= lift coefficient
L/D	= lift-to-drag ratio
M	= Mach number
R	= Radius of curvature
P	= pressure
S	= surface area
T	= temperature
V	= velocity
Z	= flight altitude
r, θ	= radial coordinates
x, y, z	= cartesian coordinates
u, v, w	= velocity cartesian components
q	= dynamic pressure
θ	= shock angle
δ	= deflection angle
γ	= ratio of specific heat
ρ	= density, kg/m^3

Subscripts

avg = refers to average value

max = maximum

o = denotes total conditions

u = refers to property at the upper surface

s = refers to property at the shockwave

= freestream conditions

Superscripts

' = differentiation

Chapter 1

Introduction

1.1 Motivation

Among the broad choice of possible propulsion systems, a RLV could be designed as an air-breathing vehicle. The main advantage of that propulsion system is the reduced weight of the vehicle associated with the fact that the fuel that needs to be carried on board is less- the oxidizer is simply the atmospheric oxygen of the incoming airflow into the inlet. An air-breathing vehicle will take off horizontally and thus gives the advantage, over conventional vertical launch rockets, firstly to offer a low turn-around time (close to those of the airliners), and secondly does not require as much infrastructure. Air-breathing vehicles are integrated systems for which the inlet design and airframe design need to be couple to get a viable design. Contrary to conventional rockets, air-breathing vehicles do not fight gravity and use the atmospheric oxygen as fuel, which is why those vehicles accelerate within the atmosphere.

Hypersonic cruisers and reentry vehicles will benefit from high lift over drag (L/D) ratio; accelerators such as access-to-space airbreathers also benefit from high L/D when it is achieved with minimal drag and lift matched to weight. For an airbreathing engine, the flow entering the inlet should most likely present the most highly uniform flow possible with high efficiency. Those properties are determined in large measure by the choice of the forebody of the vehicle: the design of a hypersonic vehicle couples the engine and the airframe. The different shapes considered as the forebody of hypersonic air-breathing vehicles include wedge shaped inlet, star-shaped inlet, cone-shaped, and waveriders.

Waveriders geometries have been of special interest for hypersonic missions since they tend to provide higher L/D at high Mach numbers than conventional hypersonic forms. A waverider is any geometry such that its bow shock is attached to the entire leading edge. Waveriders design methods are generally “inverse”, meaning that a flowfield is first identified, then the corresponding surface is determined. This permits direct specification of optimal desired inlet properties for an engine (i.e. no shock entering the engine, two-dimensional flowfield, etc.). Those qualities explain why today those geometries raise high interest for a wide range of high-speed mission applications: hypersonic cruise vehicle¹⁻², hypersonic accelerator, aero-gravity assist mission³, and lower stage of TSTO⁴⁻⁵.

The most flexible waverider design technique is the generic osculating-cones waverider design method proposed by Sobieczky in 1990. This technique is a shock-based approach, which allows great flexibility in the design process, including the specifications of the inlet performances and good volumetrics and packaging.

The osculating cones method makes implicit assumptions about the generating flowfield of those waveriders. This work has investigated those assumptions, and compared the geometries resulting from a new modified osculating cones waverider method with the geometries resulting from previous osculating cones waverider methods.

1.2 Previous Work

1.2.1 Waverider Concept

Nonweiler was the first to introduce the concept of waverider geometries in 1959 as a new concept of high-speed winged atmosphere reentry vehicles⁶ promising high lift coefficient. The advantage of those shapes would be to generate lift at high

altitude where the density of the atmosphere is still low. Considering the re-entry heating issue raised for Space vehicles, the fact that the deceleration takes place at a high altitude offers the major advantage to decrease the heating rate (which varies as atmospheric density). Thus comparing waveriders to ballistic shapes, the re-entry peak heating rate would be lower. Nonweiler derived various waverider shapes from a two-dimensional analytical solution for an oblique shock over a wedge. One of the first shapes derived with this method was a delta-wing planform over a planar shock⁷. As can be seen in Fig. 1.1-1.2, the cross-section of the resulting vehicle looks like the caret (^) typographical character, and is so-named.

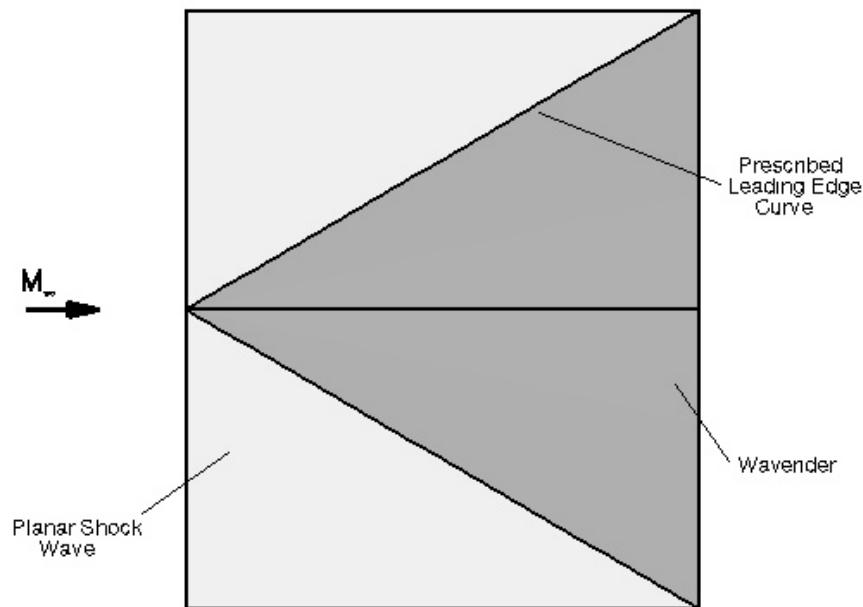


Fig. 1.1 Nonweiler caret waverider prescribed geometry, planform view

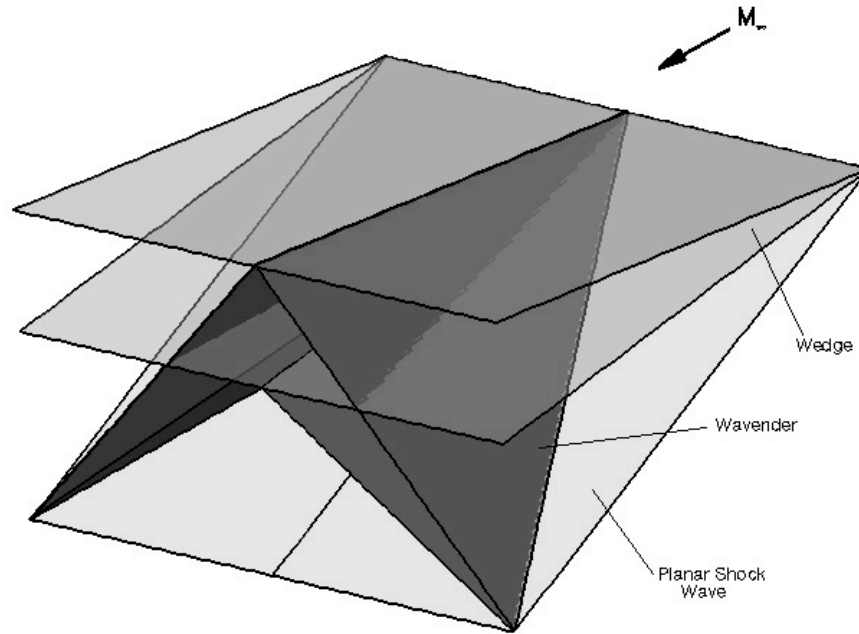


Fig. 1.2 Nonweiler caret waverider

In a similar manner, Jones derived various waveriders from inviscid conical flowfields⁸. Rasmussen generated waveriders from even more complex flowfield. He first theorized the elliptical cone flowfield⁹ with the hypersonic small-disturbance theory, and was so then able to derive waveriders from such flowfield. These early waveriders shapes had large wetted surface areas, so that the reduction of wavedrag was counteracted by an increase in viscous drag on the surface.

Rasmussen renewed the interest in this family of aerodynamic shapes by studying a new class of waveriders that were optimized for skin friction effects. As a follow-on, Bowcutt, Anderson and Capriotti¹⁰ optimized waveriders based on three-dimensional compression shapes accounting for viscous effects. The vehicle shapes were based on cone-derived shock surfaces, the flowfield being determined from an analytical solution of the Taylor-Maccoll solutions. According to their analysis, this class of vehicles showed increased lifting performances, as well as decreased wavedrag compared to the simpler two-dimensional wedge-derived waveriders.

For all these waverider designs, the vehicle was derived from a prescribed leading edge shape with streamsurfaces that intersected either a planar or axisymmetric shock. Therefore the vehicle and inlet prescribed configurations were somewhat limited. A remaining question was how to select the generating body which would form the initial shockwave in order to form the most optimal waverider shape. This is a challenging question, because only a small portion of the original generating flowfield is used in the final waverider. As such, a minimum-drag axisymmetric body would not necessarily produce the lowest-drag waverider from among the class of axisymmetric forms. As an example, extensive studies were performed on conically derived waveriders in such solutions the initial generating cone angle, and thus conical shock strength, could be varied. Similarly, axisymmetric powerlaw shapes were investigated¹¹ as generating bodies under the assumption that their lower drag as compared to cones would yield higher L/D waverider forms. This proved not to be the case. One approach to the selection of an optimal generator was pursued by Takashima and Lewis¹², who constructed waveriders from the flowfield of a blended cone-wedge. This shape was formed by slicing a cone in half and filling the space between the halves with a wedge. The flowfield was calculated with an Euler solver, then an optimizer was used to find the best waverider forms. The idea was that the blended wedge-cone generator would permit greater flexibility in choosing the final waverider form – for a more two-dimensional shape, the wedge section would be increased relative to the cone radius; for more conical flow, the wedge would be reduced in size. This also provided the advantage that the centerline shockwave could be mostly planar, to aide in engine integration.

Even the cone-wedge hybrid solver had the drawback that there was no clear way to insure the shape of the shockwave precisely, or to be certain that the selected waverider had been formed in an optimal flowfield. An elegant solution to this

problem was formulated by Sobieczky, who developed the osculating (Latin for “kissing”) cone solution which defines waveriders directly from a prescribed shockwave¹³. This inverse design method prescribes a desired leading edge shape and shockwave shape which can have a specified spanwise variation of curvature. This results in better control of the integrated vehicle design.

Previous work with osculating cone waveriders has shown that they are ideal for engine integration because of the flexibility in specifying the shockwave, and can have higher overall L/D than either cone or wedge shapes. In addition, they can be formed with pod-like structures for auxiliary engine mounting, and generally have high volume and volumetric efficiency.

1.2.1 Waverider Validation

In order to validate the waverider method, there has been a number of computational and experimental studies on waverider shapes. The present section will review the available studies before the present work, but for a more detailed review on general waverider concept it is advised to refer to the detailed waverider history review by Takashima¹⁴.

A variety of studies have been performed throughout the years on cone-derived waveriders. Yoon studied computationally the inviscid flowfield around elliptic-cone derived waveriders at on and off-design conditions¹⁵. Stecklein, and Hasen, computed the inviscid flow around a cone-derived waverider¹⁶. Lin and Shen looked at the inviscid and viscous flowfield around a cone-derived waverider with multi-directional curvature¹⁷. Cockrell and Huebner evaluated computationally and experimentally the vehicle integration of two Mach 4 cone-derived waveriders¹⁸. All those studies confirmed the general shock wave location of those cone-derived waveriders. The on-design aerodynamic performance predicted by the theory was

confirmed within 3% for the most accurate study. Lobbia, performed both experimental and computational study on cone derived waveriders¹⁹. This work demonstrated again that at on-design conditions CFD and experiments showed good L/D ratio, and the same flowfield properties distribution than the analytical solution.

The computational and experimental verification of the osculating cones waveriders design is still being investigated, as only few studies have been made. Takashima performed in his work¹⁴ some numerical simulations on osculating cone waverider shapes in order to integrate those as the forebody of a hypersonic vehicle. The computational results for the on-design conditions agreed with the general map of the analytical predicted flowfield. Miller and Argrow, tested two aluminum models of a Mach 4 and Mach 6 osculating cones geometries²⁰ (see Fig. 1.3) in the Mach 4 Unitary Plan Wind Tunnel and the Mach 6 blow down Tunnel of the Langley Research Center. At on-design conditions the experimental results confirmed both the attachment of the shock wave along the entire leading edge and its location. The measured surface pressure distributions generally agree with the analytical predictions. That study also confirmed that the osculating cones waveriders provided better L/D performances than other waverider configurations. By performing direct simulations Monte-Carlo²¹, Graves and Argrow confirmed that osculating cones designed for high altitudes performed as expected, and got some general agreement of the flowfield distribution with the theory.

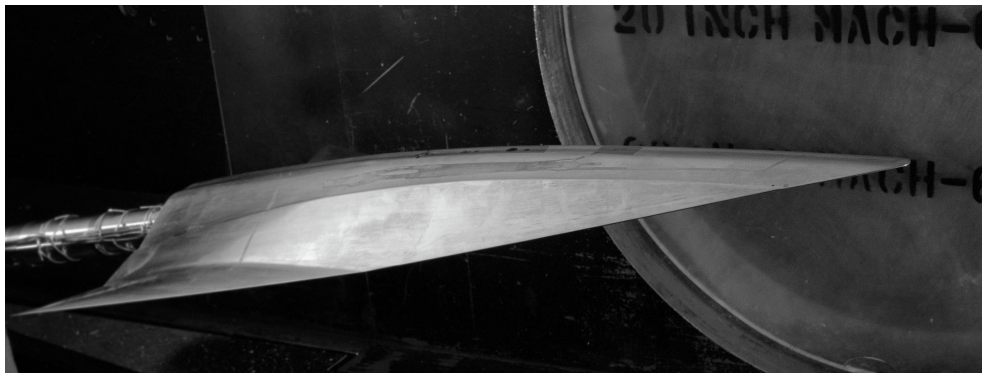


Fig. 1.3 Mach 6 Osculating cones waverider wind tunnel model

Even if the osculating cones waverider seem to be good candidates for various hypersonic missions, there is a fundamental discrepancy with this method. Osculating cones waverider designs are not exact solutions, and as such it is required to make assumptions during the design process. This is explained in more detail in the following chapter on waverider design. In short, previous osculating cones waverider works assumed that the azimuthal pressure gradients in the original generating flowfield were minimal, and thus neglected those in order to simplify the design process.

1.3 Present Work

In this work, the azimuthal pressure gradients in an osculating cone solution are calculated and introduced into the final flow solution. These are then applied to a class of shapes that are similar to those derived and optimized as the forebody of an RBCC-powered engine-integrated vehicle²² by O'Brien.

The first objective of this research was to evaluate the influence of the azimuthal pressure gradients, by integrating it inside the osculating-cone waverider solutions. The differences between the corrected and non-corrected solutions are compared for different prescribed configurations. The goal of this was to determine the magnitude of errors in previous osculating cone work.

The second objective was to validate the new design method with precise on-design CFD simulation of the inviscid flowfield around osculating cones waverider at on-design conditions. Those simulations are run for waverider geometries from the modified waverider design method and for waverider geometries from previous works. The simulations give a precise map of the flowfield, and thus comparison with the analytical flowfield distribution can be performed. Consequently accurate aerodynamic performance comparison was also to be done.

The third objective was to evaluate the previous osculating cones waverider designs against the assumption of minimal cross-flow. Indeed one of the motivations of this work was to determine how far off were the previous osculating cones waverider designs.

Chapter 2

Shock-Based Waverider Design

2.1 Waverider Design

2.1.1 Waverider Concept

By definition a waverider is any supersonic or hypersonic geometry such that the bow shock generated by the body is attached all along its leading edge at on-design conditions (Mach number and freestream flowfield conditions). As a result the flow past the shock wave is enclosed between the shock surface and the lower surface of the body. The flow over the high-pressure lower surface and the low-pressure higher surface are isolated. The flow cannot be spilled around the side of the vehicle, and thus maximum advantage is taken of the compression process that takes place across the shock. The flow can only progress toward the rear of the waverider, either the base of a full vehicle, or the inlet plane of the engine for an integrated vehicle with a waverider forebody. The interesting result is that waveriders accomplish high L/D at high C_L , thus waveriders can generate more lift than traditional rounded leading edge vehicle designs at a given dynamic pressure. Of particular interest is that this class of vehicles can generate substantial lift at higher altitude, where the air density is lower, as confirmed computationally by Graves and Argrow²¹. Considering reentry vehicles and heating issues, the fact that the deceleration takes place at a high altitude presents a main advantage for the thermal protection systems: the heating rate is less severe than for ballistic vehicles.

Although a wide variety of waverider design methods exist, a general waverider design approach can be underlined. The lower surface and the upper surface can be designed independently, as the flow over the high-pressure lower

surface and the flow over the low-pressure upper surface are isolated by the shock wave attached to the leading edge.

The lower surface of a waverider is designed to generate a desired shock wave and flowfield. This is why the waverider design is inherently an inverse design. According to the inviscid theory a streamsurface can be replaced with a solid boundary of identical geometry, this surface generating an identical shock wave. This property of inviscid flow is the reason why the lower surface of a waverider is derived as a streamsurface.

The upper surface design is arbitrary, and can be designed to fulfill performance and internal volume requirements. The upper surface can be constructed as a freestream surface (aligned to the freestream direction), expansion surface, or compression surface, or as any hybrid surface comprised of the previous surfaces.

2.1.2 Shock-Based Inverse Waverider Design

In order to meet the requirement of an attached shock wave at the leading edge, waveriders are generally constructed by an inverse design method. With that method, prescribing flowfield conditions (Mach number and freestream conditions) and vehicle design parameters (generating flowfield and vehicle geometrical parameters) determine a unique shape.

A common step to any waverider inverse design method is the choice of the generating flowfield from which the waverider geometry will be 'carved' - that is the supersonic or hypersonic flowfield over a given body.

In this work, the choice was made to input the desired flowfield properties in the base plane. The waverider is envisioned as the forebody of a hypersonic vehicle, and the base plane of the waverider would be the inlet plane of the vehicle. This

approach (shock-based inverse design approach) creates waveriders for application to scramjet inlets. The inlet design parameters define the desired flowfield at the entry of the air-breathing engine. The prescribed input geometry for this shock based waverider design technique includes the shock wave profile curve (SWPC) and the upper surface profile curve (USPC) in the base plane. In this work, it was chosen to construct the upper surface of the waverider as a surface parallel to the freestream.

The waverider shape is derived by the method summarized in Fig. 2.1. Projecting upstream the upper surface profile curve creates the upper surface, starting at the base plane until this projected surface intersects the shock wave (1). The intersection curve defines the leading edge of the waverider (2). Finally, the streamlines are traced within the generating flowfield from the leading edge up to the base plane (3). Those streamlines define the lower surface of the waverider.

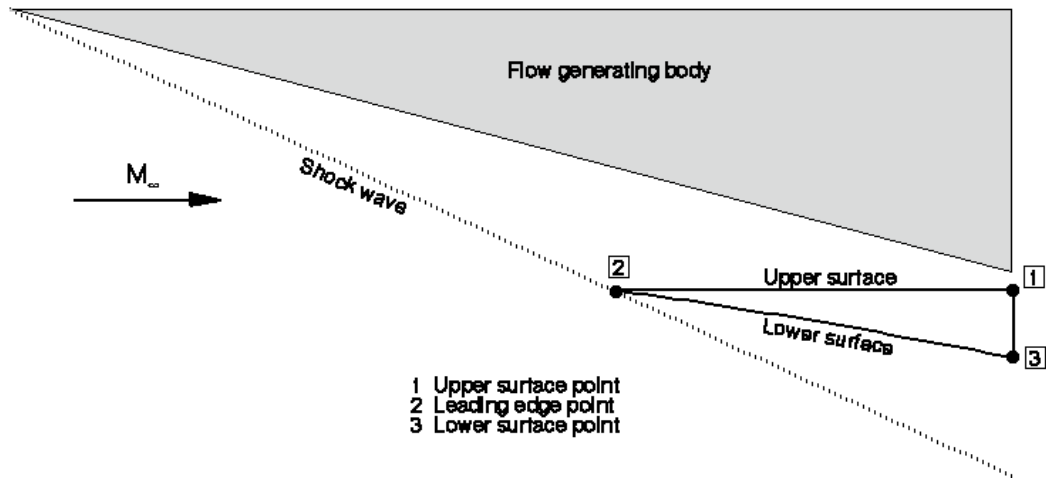


Fig. 2.1 Waverider geometry derivation from generating flowfield

In the following sections designs methods for waveriders derived from different generating flowfield are presented.

2.1.3 Wedge-Derived Waveriders

For wedge-derived waveriders, the generating flowfield is uniquely determined by a shockwave angle θ and a freestream Mach number M . From the following oblique shock relations²³ the wedge surface angle θ , and the uniform flowfield properties of the shock layer are derived (Mach number M_2 , pressure P_2 , temperature T_2 , density ρ_2)

$$\tan \theta = 2 \cot \theta \frac{M^2 \sin^2 \theta - 1}{M^2 (\theta + \cos 2\theta) + 2} \quad (2.1)$$

$$M_2 = \frac{M_{n2}}{\sin(\theta)} \quad (2.2)$$

where the normal Mach number after the shock M_{n2} , and before the shock M_n are

$$M_{n2} = \sqrt{\frac{M_n^2 + [2/(\theta - 1)]}{2M_n^2/(\theta - 1) - 1}} \quad (2.3)$$

and

$$M_n = M \sin \theta \quad (2.4)$$

$$P_2 = P \left[1 + \frac{2\theta(M_n^2 - 1)}{\theta + 1} \right] \quad (2.5)$$

$$\rho_2 = \rho \frac{(\theta + 1)M_n^2}{(\theta - 1)M_n^2 + 2} \quad (2.6)$$

$$T_2 = T \frac{P_2}{P} \frac{\rho}{\rho_2} \quad (2.7)$$

As described in the previous section, in the present shock-based waverider design method, two curves are prescribed in the base plane: the USPC and the SWPC. The shock wave generated by the waverider is defined by the SWPC and the shock wave angle θ . Projecting upstream the USPC until it intersects the shock wave creates the upper surface of the vehicle. The lower surface is derived as a wedge-

flow streamsurface. As an example Fig. 2.2 presents a waverider derived from a Mach 6.0 flow over a wedge with a 30° shock wave angle.

Initially those geometries raised interest for hypersonic applications as they generate a uniform flowfield. This property is advantageous to integrate the waverider inside a high-speed air-breathing vehicle. The drawback of the planar nature of the geometry is a low volumetric efficiency, which limits the capacity to carry fuel on board, and thus vehicle range.

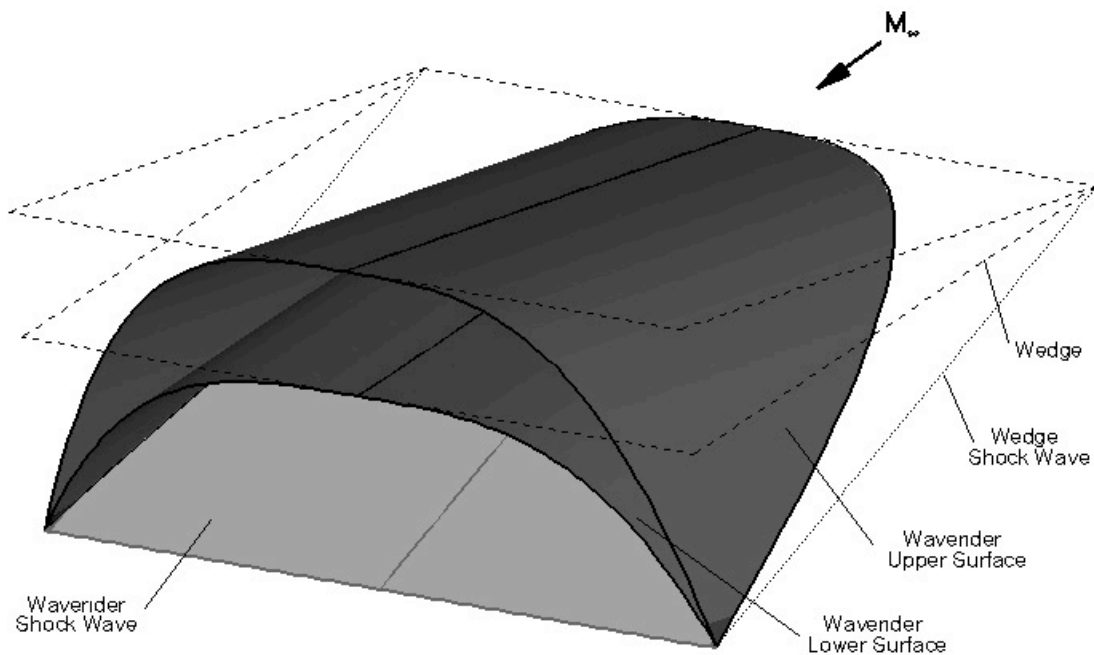


Fig. 2.2 Mach 6 wedge-derived waverider

2.1.4 Cone-Derived Waveriders

For this class of waveriders, the generating flowfield is the three-dimensional supersonic flow over a cone at a zero angle of attack. Contrary to the two-dimensional flow over a wedge, the axisymmetric supersonic flow is nonlinear and

thus cannot be solved with an exact solution. A numerical solution for the conical flowfield can be obtained by numerically integrating the Taylor-Maccoll equations²⁴.

Taylor-Maccoll conical flow formulation

$$\frac{\sin \theta}{2} \left(\frac{V_r}{V_{\max}} \right)^2 \left[\frac{dV_r}{d\theta} \right]^2 + \frac{dV_r}{d\theta} \cot \theta + \frac{d^2 V_r}{d\theta^2} \frac{dV_r}{d\theta} + \frac{dV_r}{d\theta} \frac{d^2 V_r}{d\theta^2} = 0 \quad (2.8)$$

where V_r is the radial velocity component, θ is the angle from the cone axis and the ray considered for the solution, and V_{\max} is the velocity that the flow would achieve if it were to be expanded to zero temperature

$$V_{\max} = \sqrt{2h_o} = \sqrt{2C_p T_o} \quad (2.9)$$

The normal component of velocity is derived by

$$V_{\theta} = V_r' = \frac{dV_r}{d\theta} \quad (2.10)$$

Defining a nondimensional velocity as

$$\bar{V} = \frac{V}{V_{\max}} \quad (2.11)$$

the previous differential equation becomes

$$\frac{\sin \theta}{2} \bar{V}_r^2 + \bar{V}_{\theta} \cot \theta + \frac{d^2 \bar{V}_r}{d\theta^2} \bar{V}_{\theta} + \bar{V}_{\theta} \frac{d^2 \bar{V}_r}{d\theta^2} = 0 \quad (2.12)$$

$$\theta = \frac{\sin \theta}{2} \left(1 - \bar{V}_r^2 - \bar{V}_{\theta}^2 \right) \quad (2.13)$$

This equation can be rearranged as an ordinary differential equation of the second derivative of the radial velocity

$$\frac{d^2 \bar{V}_r}{d\theta^2} = \frac{\bar{V}_r \bar{V}_{\theta}^2 - 2\theta \bar{V}_r \bar{V}_{\theta} \cot \theta}{\sin \theta \bar{V}_{\theta}^2} \quad (2.14)$$

In other terms, that equation can be rewritten as

$$\frac{d^2 \bar{V}_r}{d\bar{r}^2} = f(\bar{r}, \bar{V}_r, \bar{V}_r') = f(\bar{r}, \bar{V}_r, \bar{V}_r'') \quad (2.15)$$

Behind the shock, the equation of conservation of total enthalpy relates the local

Mach number M to the non-dimensionalized velocity \bar{V}

$$\bar{V} = \frac{2}{(\bar{r} - 1) M_2^2} + 1 \quad (2.16)$$

Thus the derivation of the non-dimensionalized velocity flowfield throughout the cone shock layer enables to derive all other flowfield properties.

Numerical solution of the axisymmetric supersonic flowfield

The transformed Taylor-Maccoll equation is numerically integrated using the fourth order Runge-Kutta method. The numerical solution of the supersonic flowfield over a cone is calculated by an inverse approach where the input parameters are the shock wave angle \bar{r} and freestream Mach number M . Starting immediately behind the shock, the flow deflection angle \bar{r} Mach M_2 , and flowfield properties (total temperature, total pressure, total density) are derived from the oblique shock relations. After the shock wave, the total flowfield properties are constant in the shock layer since the flow is isentropic. The total flowfield variables behind the shock are derived from the following compressible flow relations²³

$$P_o = P_2 \left[\frac{\bar{r}}{\bar{r} - 1} + \frac{\bar{r} - 1}{2} M_2^2 \right]^{\frac{\bar{r}}{\bar{r} - 1}} \quad (2.17)$$

$$\rho_o = \rho_2 \left[\frac{\bar{r}}{\bar{r} - 1} + \frac{\bar{r} - 1}{2} M_2^2 \right]^{\frac{1}{\bar{r} - 1}} \quad (2.18)$$

$$T_o = T_2 \left[\frac{\bar{r}}{\bar{r} - 1} + \frac{\bar{r} - 1}{2} M_2^2 \right] \quad (2.19)$$

The numerical solution is started with the non-dimensionalized radial velocity right behind the shock:

$$\bar{V}_r = \bar{V} \cos(\theta) \quad (2.20)$$

Where \bar{V} is related to the Mach number M_2 by Eq. 2.16. At each ray, the radial velocity is solved by the fourth-order Runge-Kutta method. The following equations give the tangential velocity, and flow properties (pressure, temperature and density) derived from the isentropic relations²³, throughout the conical flowfield

$$P = P_o \left[\frac{1}{2} + \frac{\theta}{2} M^2 \right]^{1/\gamma} \quad (2.21)$$

$$T = T_o \left[\frac{1}{2} + \frac{\theta}{2} M^2 \right]^{1/\gamma} \quad (2.22)$$

$$\rho = \rho_o \left[\frac{1}{2} + \frac{\theta}{2} M^2 \right]^{1/\gamma} \quad (2.23)$$

where the local Mach number M is calculated from the local velocity (Eq. 2.16). The Taylor-Maccoll equation is numerically integrated until $\bar{V}_\theta = 0$ -this corresponds to the surface of the cone, θ of the current ray is then the cone semi-vertex angle.

Cone-derived waverider design

The generating flowfield is uniquely determined prescribing a cone shock wave angle θ , a freestream Mach number M_∞ , and freestream conditions (flight altitude Z).

From the prescribed waverider base plane geometry (USPC and SWPC), the shape is derived according to the generic method presented in Sec. 2.1.2. After the derivation of the leading edge, the streamlines (which define the lower surface) are traced within each radial plane, from the leading edge to the base plane according to the following equation:

$$\frac{dy}{dx} = \frac{V_\theta}{V_r} \quad (2.24)$$

where x , y , V_θ and V_r are local to each radial plane. The tracing of those streamlines is more challenging than for wedge-derived waveriders. Indeed, within a supersonic axisymmetric flowfield, contrary to a supersonic wedge flowfield, the streamlines curve continuously downstream of the shock wave. From a waverider design standpoint, this property requires to know at each point of the lower surface the local radial and tangential flow velocities. Thus at each new derived point on a streamline, the design method has to determine the angular position θ of this point within the generating conical flowfield, according to the following equation,

$$\theta = \tan^{-1} \left(\frac{R \sin \theta}{R / \tan(\theta)} \right) \quad (2.25)$$

where r is the radial coordinate of the local point in the generating flowfield cone coordinates, and R the local radius of the cone.

Once the method has determined on which ray of the conical flowfield the point is located, the flowfield properties can be derived from the generating flowfield. As an example, Fig. 2.3 presents a waverider derived from a Mach 6.0 flow over a cone with a 30° shock wave angle.

Cone-derived waveriders, contrary to wedge-derived waveriders have higher volume efficiency. The volume is concentrated around the centerline of the vehicle thus it can carry a decent amount of fuel on board. The drawback of those shapes is that the flow is three-dimensional which makes those less attractive to integrate into an air-breathing engine vehicle than wedge-derived waveriders.

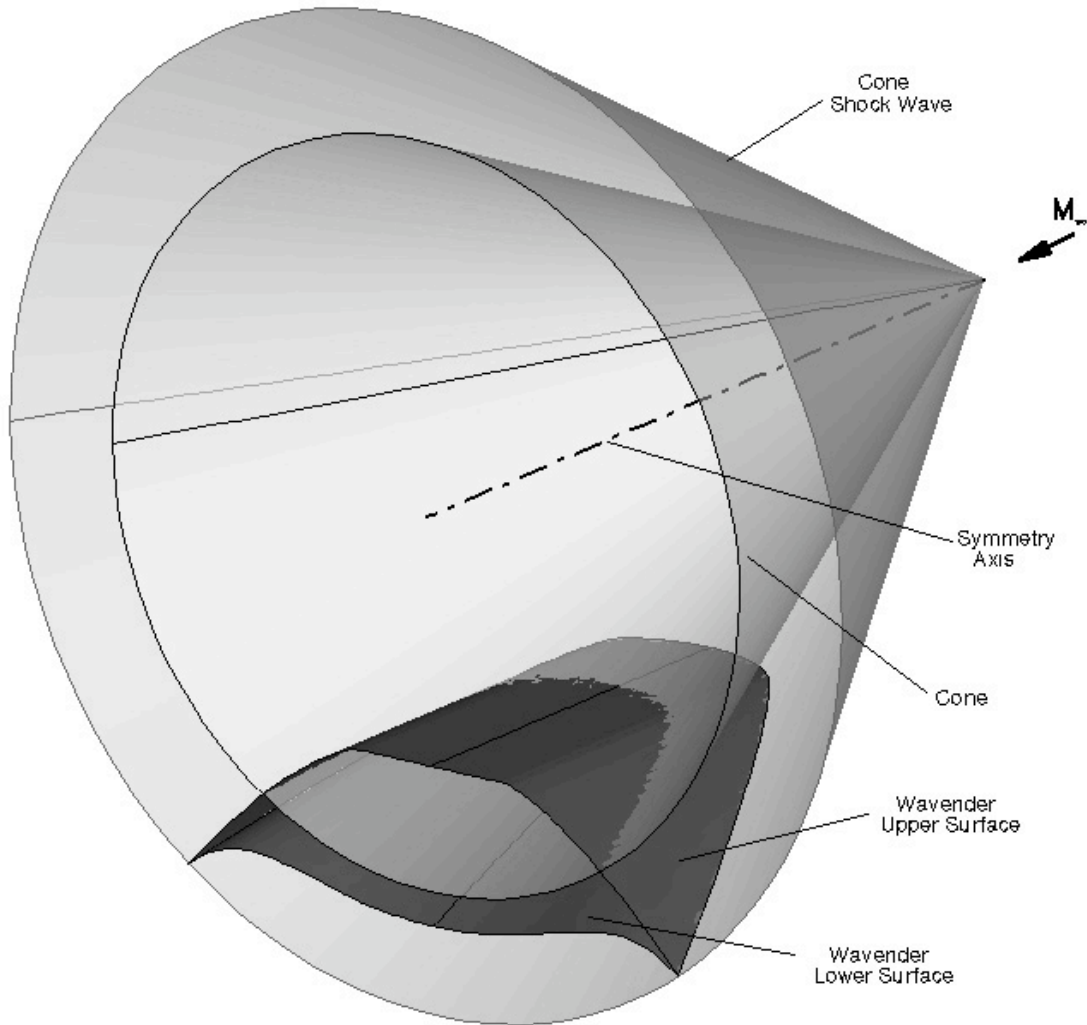


Fig. 2.3 Mach 6 cone-derived waverider

2.1.5 Osculating Cones Waveriders

As it was explained in the previous sections, the waverider derived from a two-dimensional and three-dimensional flowfield both present advantages from the vehicle design standpoint, but each of those carry inherent drawbacks. These classical waveriders shapes present the disadvantage that the generator must be chosen first, which leaves less freedom of choice for the design of the inlet flowfield. With the osculating cones waverider method²⁵⁻²⁷, Sobieczky created a design method

that starts with a desired shockwave shape, and thus makes the waverider more flexible to designers need. Conical slices of different radii are spliced together to form a complete shock layer. This method produces a virtual flowfield generator, but the designer needs not identify this directly. With that method, a combination of a shockwave profile curve and upper surface profile curve in the base plane, enable to derive uniquely a full geometry at on-design parameters from the following method. Wedge-derived waveriders and cone-derived waveriders are indeed limiting cases of the osculating cones waveriders method; wedge-derived forms prescribe a SWPC with an infinite radius of curvature, and cone-derived ones prescribe a SWPC with a constant radius of curvature. Thus the osculating cones method can be seen as a generic waverider design method, as schematized in Fig. 2.4.

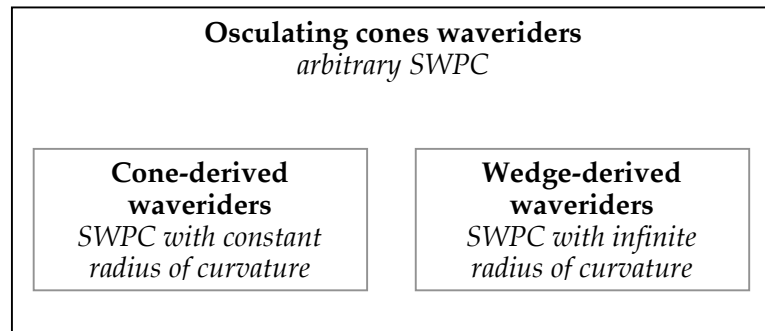


Fig. 2.4 Waverider design methods relationships

The osculating cones waverider solution is a strip method. At each azimuthal location along the shockwave surface, the flow is determined from the local osculating (i.e. “kissing”) cone properties. In order to derive a shock surface of constant strength all the osculating cones have the same shockwave angle, but different radii depending on the local shockwave curvature. An infinite radius of curvature means that the flow will be two-dimensional, and a finite radius of curvature means that the flow will be three-dimensional. In Fig. 2.5, the azimuthal

distribution of the radius of curvature along the shockwave is presented for a shock wave profile curve in the base plane with a uniform section at the centerline and an outboard curved section.

However, as it was pointed out in the introduction, there is one fundamental problem with the osculating cones method. Unlike the earliest waveriders, osculating cones waveriders are not exact solutions. Shapes such as the inviscid

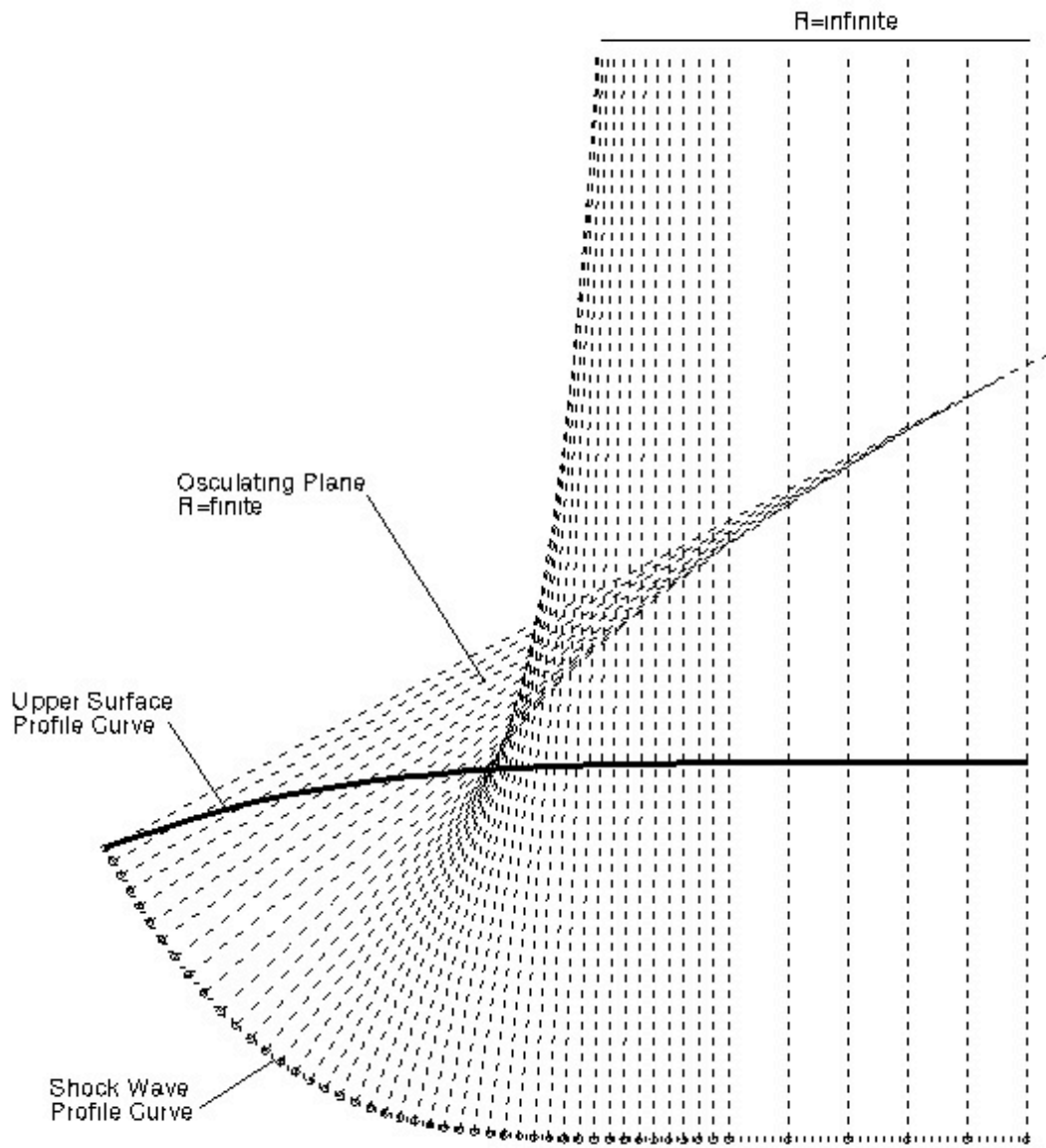


Fig. 2.5 Osculating cones in the base plane

wedge-derived waveriders are exact because the flowfield is mathematically hyperbolic. A waverider in these classes will recover the relevant portion of the original generating flowfield exactly. In contrast the osculating cone solutions neglect pressure gradients in the original generating flowfield exactly, so the resulting waveriders will not exactly recover the original flowfield. This discrepancy results because it has been assumed that since the cross-flow between the osculating cones was minimal, the azimuthal pressure gradients could be neglected. This assumption greatly simplifies the design process, as the flow can be calculated independently within each osculating cone slice.

In this work, the azimuthal pressure gradients in an osculating cone solution are calculated and introduced into the derivation of the waverider lower surface. These are then applied to a class of shapes that are similar to those derived and optimized as the forebody of an RBCC-powered engine-airframe integrated vehicle.

2.2 Present Osculating Cones Waverider Design

2.2.1 Prescribed Parameters

For purposes of vehicle design, certain parameters can be selected in order to specify the desired osculating-cone waverider. The freestream conditions (on-design Mach number M , and flight altitude Z) are chosen depending on the mission to be achieved by the vehicle. The freestream flowfield properties (density ρ , temperature T , pressure P) are determined from the on-design flight altitude, in the present work using the 7-layer model of the 1976 Standard Atmosphere²⁸. The length of the waverider L , and the shockwave angle of the generic cone shock wave θ have also to be specified. The choice of the cone shockwave angle can have a significant impact on the resulting shape of the waverider, as it determines the strength of the shock

surface. The design range for the shock wave angle θ is limited by the Mach angle, for the conical flow to exist:

$$\theta \geq \sin^{-1} \left[\frac{1}{M} \right] \quad (2.26)$$

The cone half angle, as well as the flow properties of the shock layer for the generic cone are derived from the numerical solution of the Taylor-Maccoll equations as presented in the previous section.

As explained previously, this work was motivated by waveriders designed for application to scramjets inlets. Two geometry functions define the desired flowfield at the entry of the air-breathing engine subject to freestream conditions: the shock wave profile curve (SWPC) and the upper surface profile curve (USPC) in the base plane of the waverider. In order to obtain a uniform inlet flow the central section of the SWPC is chosen to be planar (two-dimensional flow). For the outboard section the SWPC is curved in order both to generate regions of accessible volume (storing space), and to get a shock wave with strong gradients in curvature. This design choice was motivated by the fact that gradients in the shock wave shape result in pressure gradients. The curved section of the SWPC is a power-law curve ($y=Ax^n$), as detailed below:

$$\text{Shockwave profile curve flat portion: } \begin{cases} 0 \leq z_s \leq L_s \\ y_s = H = L \tan(\theta) \end{cases} \quad (2.27)$$

$$\text{Shockwave profile curve curved portion: } \begin{cases} z_s \geq L_s \\ y_s = H + \frac{z_s - L_s}{A} \left[\frac{z_s - L_s}{L_s} \right]^n \end{cases} \quad (2.28)$$

The USPC of the waverider is also chosen to be a power-law curve:

$$\text{Upper surface profile curve flat portion: } \begin{cases} 0 \leq z_u \leq L_u \\ y_u = 0 \end{cases} \quad (2.29)$$

Upper surface profile curve curved portion:
$$y_u = \frac{z_u - L_u}{B} L_u^{1/q} \quad (2.30)$$

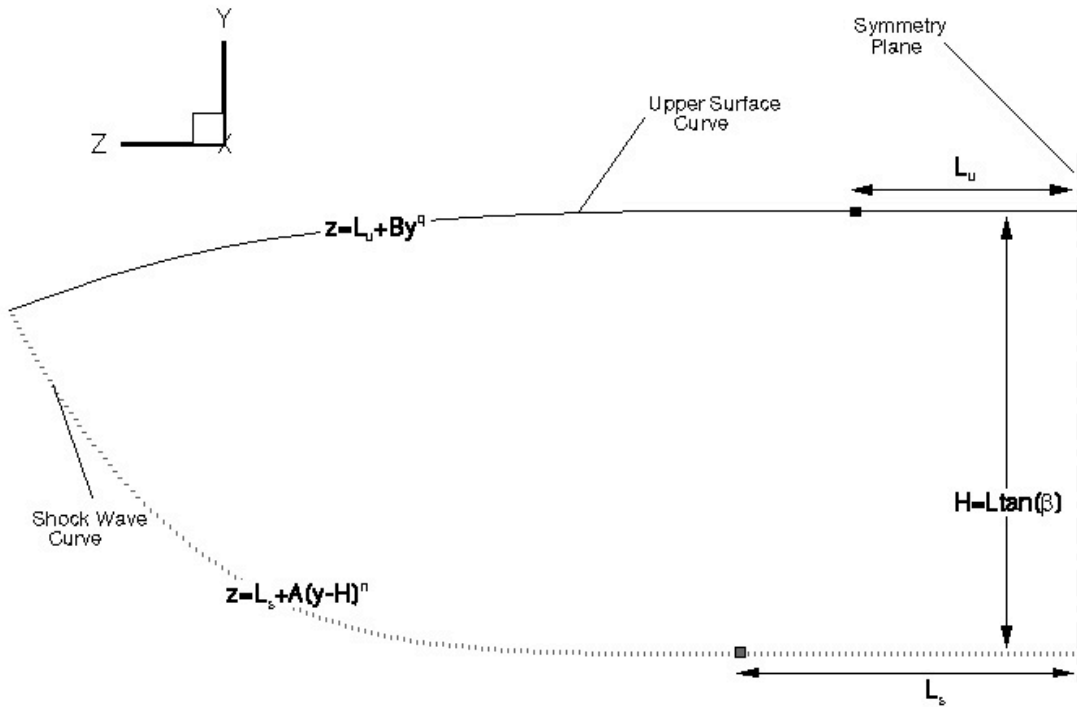


Fig. 2.6 Prescribed shock wave profile curve and upper surface profile curve geometry in the base plane

An example of a prescribed geometry in the base plane is presented in Fig. 2.6.

The upper surface of the waverider is chosen to be parallel to the freestream direction, i.e. it is designed as a freestream surface. The lower surface of the vehicle (the compression surface for the engine of the vehicle) is classically a stream surface. The streamlines defining the lower surface are traced from the leading edge to the base plane.

As it can be observed on Fig. 2.6, the class of waveriders studied for this work presents a strong gradient in the shock wave curvature in the azimuthal direction.

This was indeed not an optimal choice from the vehicle integration standpoint, but was motivated to generate waverider shapes with strong azimuthal pressure gradients.

2.2.2 Leading Edge, Shockwave and Upper Surface Derivation

Once the flowfield is defined in the base plane by the prescribed SWPC and the freestream conditions, the next step in the design is to derive the first elements of the geometry of the waverider (leading edge, upper surface, and shockwave shape). In the base plane, local osculating cones are traced along the SWPC at each discrete point. The radius of the osculating cone is the local radius of curvature of the shockwave profile curve in the base plane, which is given by:

$$R = \frac{\left[\left(\frac{dy}{dz} \right)^2 \right]^{3/2}}{\frac{d^2y}{dz^2}} \quad (2.31)$$

The axis of symmetry of the cone is traced from the vertex of the cone, parallel to the freestream direction. The local osculating plane (perpendicular to the base plane) passes by the axis of symmetry of the cone and the cone local radius (i.e. locally normal to the SWPC). The angle between the osculating plane and the vertical xy plane is given by:

$$\theta = \frac{\theta}{2} \tan^{-1} \left[\frac{dz}{dy} \right] \quad (2.32)$$

For each discrete point of the SWPC, the point at the intersection of the prescribed USPC and the local osculating plane has to be determined. This discrete process is summarized in Fig. 2.7.

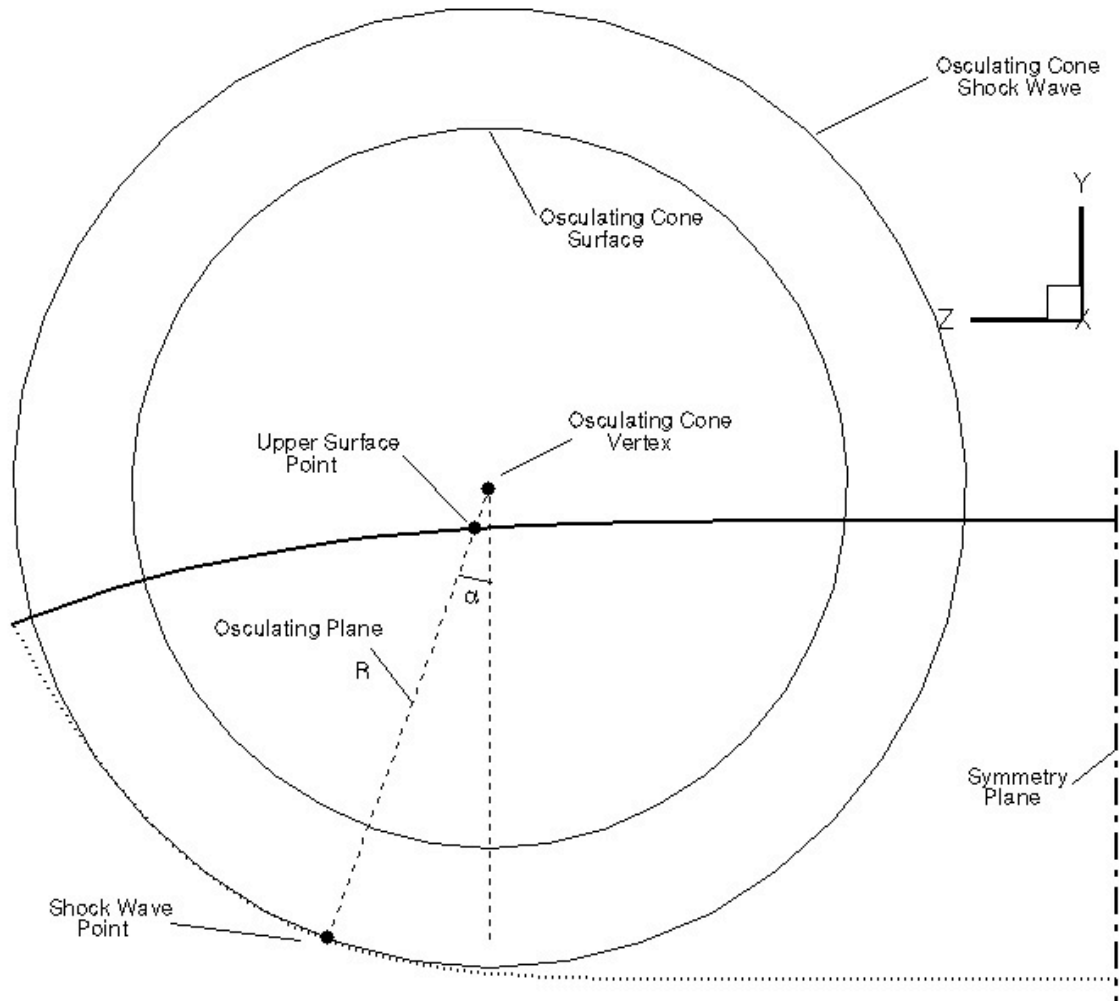


Fig. 2.7 Osculating cone derivation, base plane

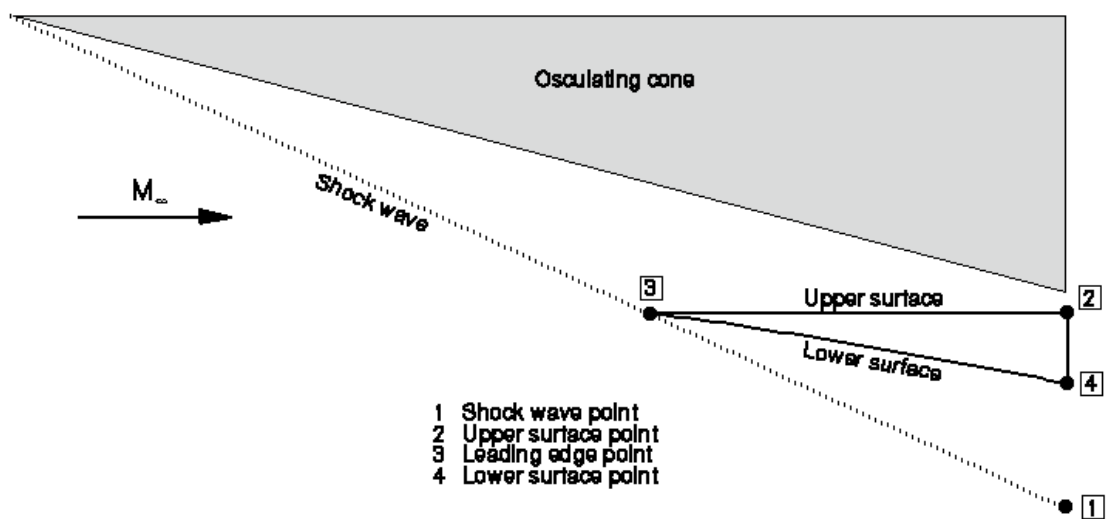
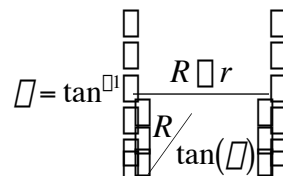


Fig. 2.8 Osculating cones waverider design in a local osculating plane

In the present design method the derivation of the upper surface, shock wave surface and leading edge are identical to previous osculating cones waverider design methods, and is summarized in Fig. 2.8. The upper surface of the waverider is constructed by projecting upstream the USPC in the freestream direction. The shock wave generated by the waverider is determined by developing upstream in the streamwise direction the SWPC, along each local osculating cone surface. Both the shock wave and the upper surface are projected upstream, beginning at the base plane, until these two surfaces intersect. This intersection defines the leading edge of the waverider. The lower surface derivation presented in Fig. 2.8 is illustrating the method used by previous studies: the lower surface is derived independently within each osculating cone stripe.

2.2.3 Osculating Cones Generating Flowfield Derivation

The following step of the waverider design is to derive the inviscid flowfield properties for points located between the upper surface and the shockwave of the geometry (“shock layer” of the waverider). In other words, the generating osculating cones flowfield has to be derived. At each streamwise location, flowfield properties (velocity V , pressure P , temperature T , and density ρ) are derived from the conical flow solution within each local osculating cone stripe. Within each local osculating plane, flowfield properties are derived depending on the angular position θ of the considered point in the local conical stripe:

$$\theta = \tan^{-1} \left(\frac{R - r}{R / \tan(\theta)} \right) \quad (2.33)$$


where r is the radial coordinate of the local point in the generating flowfield cone coordinates, and R the local radius of the osculating cone. A cubic spline

interpolation of the generic conical flowfield evaluated at the ray defined by φ gives P, T, φ , the local radial velocity V_r and the local tangential velocity V_t . The velocities components are transformed into the waverider coordinates, as detailed by the following equations

$$u = V_r \cos(\varphi) + V_t \sin(\varphi) \quad (2.34)$$

$$v = \cos(\varphi) [V_r \sin(\varphi) + V_t \cos(\varphi)] \quad (2.35)$$

$$w = \sin(\varphi) [V_r \sin(\varphi) + V_t \cos(\varphi)] \quad (2.36)$$

Importantly, the resulting osculating cones generating flowfield does not account for any pressure gradients between the osculating cones. As the osculating cones are adjacent in the azimuthal direction, the pressure gradients that were neglected in the previous waverider designs solutions are azimuthal.

2.2.4 Pressure Gradients Corrections

The present work has produced a new methodology to account for the azimuthal pressure distribution, and associated gradients. In order to account for pressure gradients, it was desirable to input corrections of the pressure field within the shock layer. The correction applied in this work has been derived from the Euler's incompressible flow equation (Eq. 2.37), applied to the local flowfield pressure gradients.

$$dV^2 = \varphi \frac{2}{\varphi} dP \quad (2.37)$$

More precisely, those corrections are implemented inside the osculating cones waverider design method, after the inviscid osculating cones generating flowfield has been derived. At each streamwise plane, a correction in velocity is applied between points adjacent in the azimuthal direction:

$$\left(\Delta V_i^2\right)_{corr} = \Delta \frac{2}{\Delta_i} \Delta P_i = \Delta \Delta \frac{2}{\Delta_i} \frac{\Delta P_{i+1} - \Delta P_{i-1}}{2} \Delta \quad (2.38)$$

$$V_i = V_i + \sqrt{\left(\Delta V_i^2\right)_{corr}} \quad (2.39)$$

2.2.5 Lower Surface Derivation

The lower surface is constructed from the leading edge of the waverider up to its base plane, by tracing streamlines within the previously derived osculating cones generating flowfield. As mentioned in the cone-derived waverider method, the design of the lower surface of the waverider is the sensitive part of the design. As for the cone-derived waverider method, to trace the streamline within the three-dimensional osculating-cones generating flowfield, the flowfield properties have to be determined at each streamline point.

Beginning at the leading edge point, at each azimuthal location (i.e. location perpendicular to the freestream direction), the location of the following point downstream on a streamline is derived according to Eq. 2.40-2.41.

$$y_k = y_{k-1} + \frac{v_{k-1}}{u_{k-1}} (x_k - x_{k-1}) \quad (2.40)$$

$$z_k = z_{k-1} + \frac{w_{k-1}}{u_{k-1}} (x_k - x_{k-1}) \quad (2.41)$$

Once the location of the next point on the streamline has been determined, flowfield properties at this point are derived in order to trace the next segment of the streamlines. Contrary to the previous waverider solutions, the streamlines tracing does not occur in the same constant plane (osculating plane), since the azimuthal pressure gradients correction induce velocities components in the azimuthal direction (i.e. outward the osculating plane). For each azimuthal location, at each streamwise point the flowfield variables (u , v , w , P , T and Δ) are determined with an

inverse distance weighted interpolation (Shepard's method) from the closest neighboring "reference points". Those points are the one where the generating osculating cones flowfield has been derived. As an example, the following equation shows the inverse distance weighed interpolation for the x -component of velocity,

$$u = \frac{\sum_{i=1}^{10} \frac{u_i}{\left[(x - x_i)^2 + (y - y_i)^2 + (z - z_i)^2 \right]}}{\sum_{i=1}^{10} \frac{1}{\left[(x - x_i)^2 + (y - y_i)^2 + (z - z_i)^2 \right]}} \quad (2.42)$$

An example of a complete waverider is shown in Fig 2.9. As it can be observed on that figure, the transition from a two-dimensional flow at the central section of the waverider, to a three-dimensional flow at the outboard section, results for the lower surface in a surface closer to the shockwave. This is classically known as the "three-dimensional relieving effect"²⁴: the flow has an additional dimension to move through, and thus expands more over a given distance than over the equivalent planar geometry. For the conical pressure flowfield to match the wedge flow pressure, the compression surface needs to sit closer to the shock wave at the outboard section of the waverider.

2.2.6 Comparison of Waverider Geometries for Corrected and Uncorrected Osculating Cones Waverider Method

For different prescribed waverider flowfield conditions and base plane geometry, both pressure-gradient corrected and uncorrected vehicle geometries were generated and are presented in Fig. 2.9-2.13.

Overall, the pressure corrections have been found to induce very small modifications on the geometry of the streamlines. The compression surface

(streamsurface) is thus very moderately impacted by the azimuthal pressure gradients.

For the Mach 3 waveriders, some geometric differences between the corrected lower surface and the non-corrected lower surface can be observe in Fig. 2.9. The modifications introduced by the current design method are occurring in the region where the gradients of shock wave curvature are the highest, which is where the pressure gradients are located.

For the Mach 6 waveriders, some differences are still visible between the two different designs. Compared to the Mach 3 waveriders, the corrections are of much less amplitude for this configuration.

As observed for the Mach 10 and Mach 15 waveriders, the effect of the modifications are decreasing with increasing Mach number. The geometries for those two configurations are almost geometrically identical.

Comparing the osculating cones waverider geometries of Fig. 2.9 and Fig. 2.12, it can be noted that the modifications are noticeable for the Mach 3 waverider, but are not perceptible for the Mach 15 waverider. This decrease in the corrections introduced by the present design code underlines that the azimuthal pressure gradients are negligible at high Mach numbers

For this research other waverider geometries were derived, with a SWPC with smaller shock curvature gradients. The resulting geometries from the new design method and previous design methods did not present any perceptible difference. Consequently for validation purposes of the present design method, it was chosen to run CFD simulations only on the waverider geometries presented in the following figures. The class of waveriders studied presents high gradients in the shock wave curvature, which is not an optimal choice for vehicle design purposes, but rather an extreme case, chosen to generate the highest possible azimuthal pressure gradients.

Mach 3 Waverider

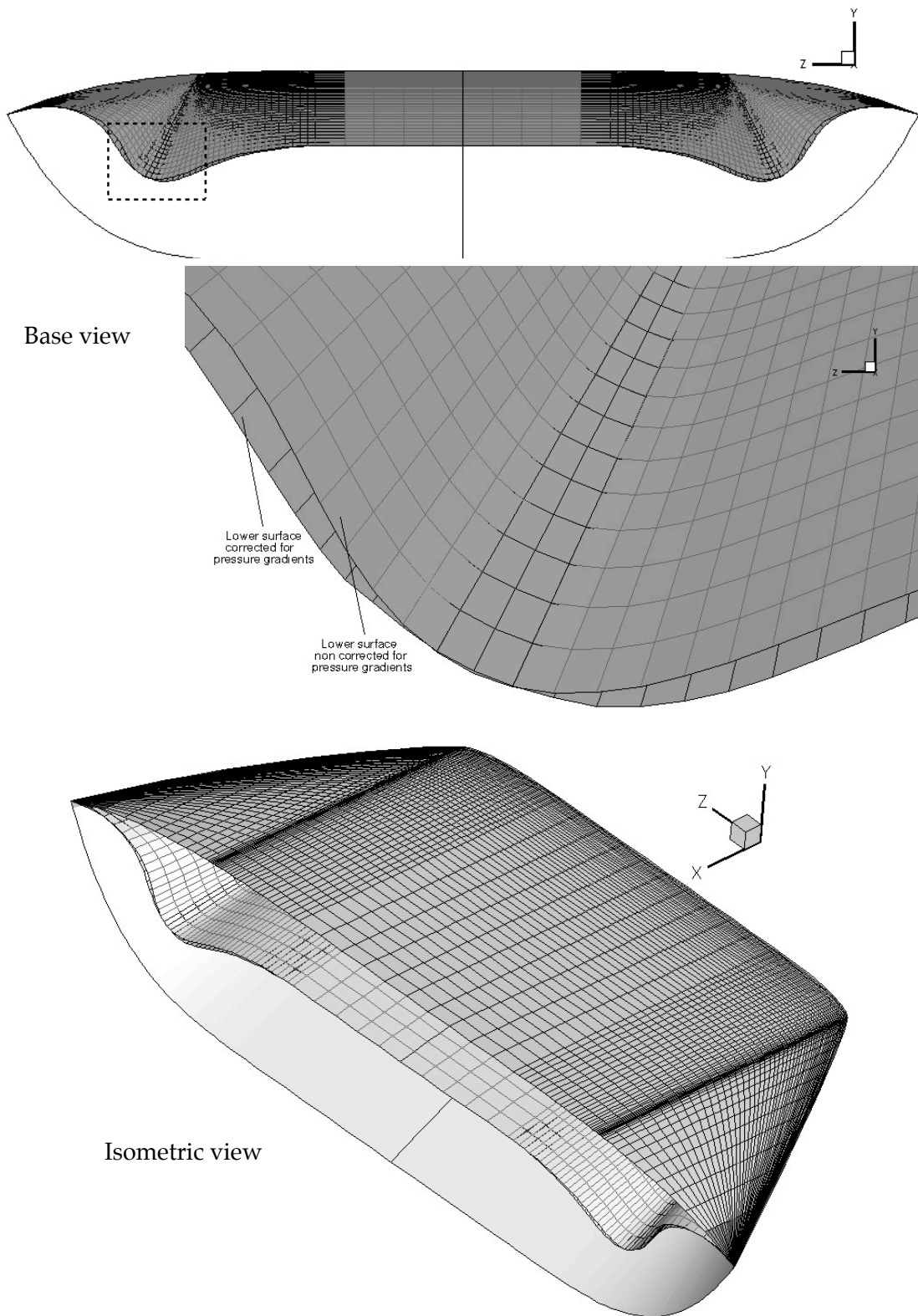


Fig. 2.9 Mach 3 osculating cones waverider

Mach 6 Waverider

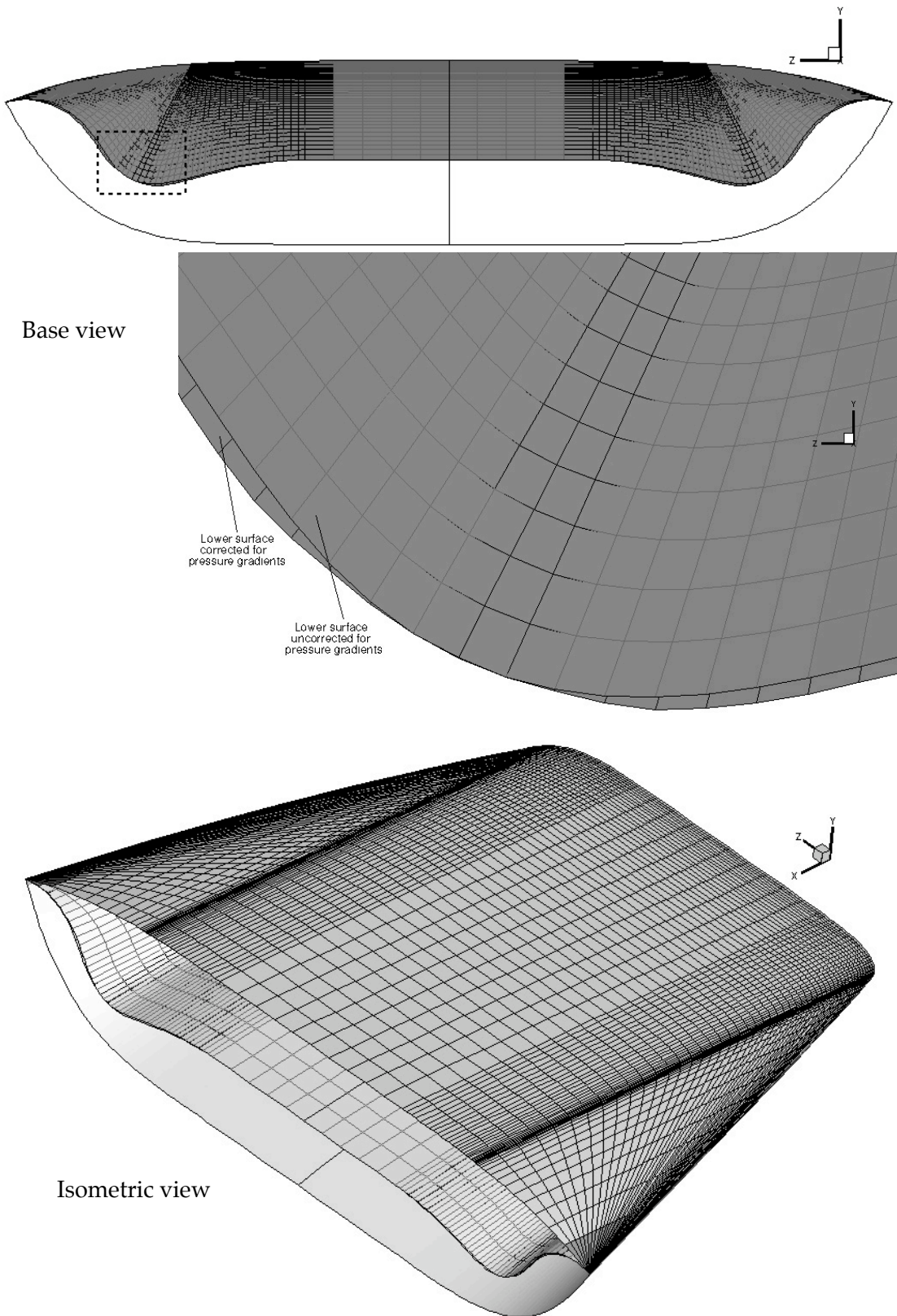
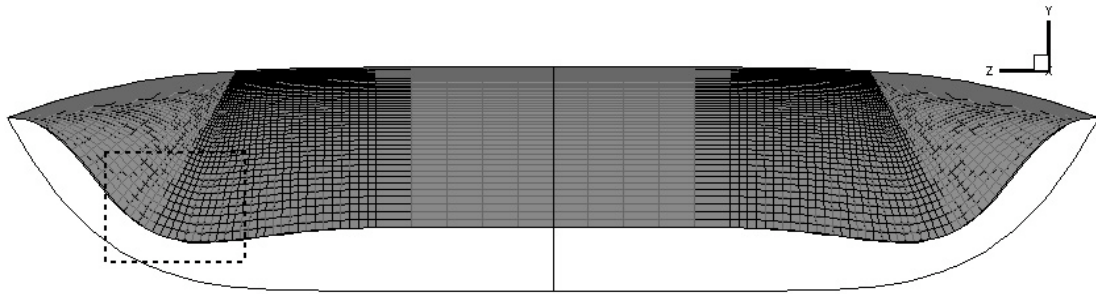
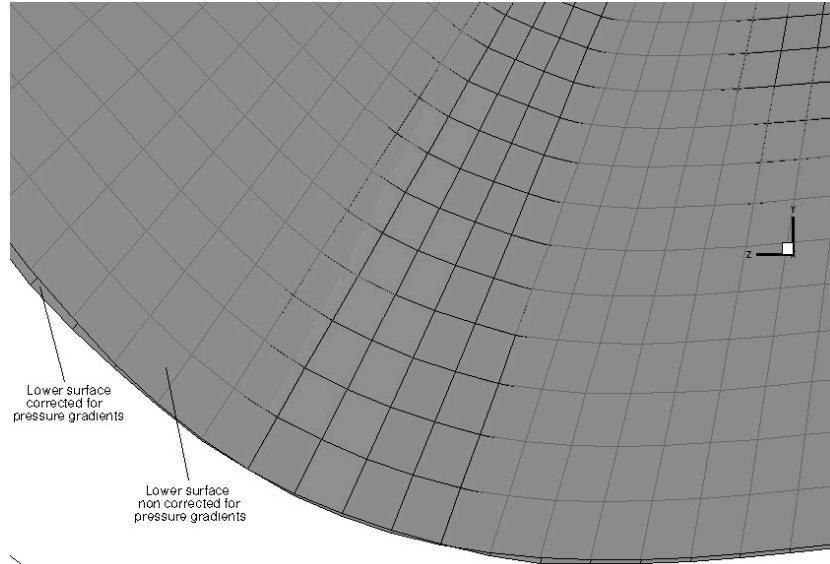


Fig. 2.10 Mach 6 osculating cones waverider

Mach 10 Waverider



Base view



Isometric view

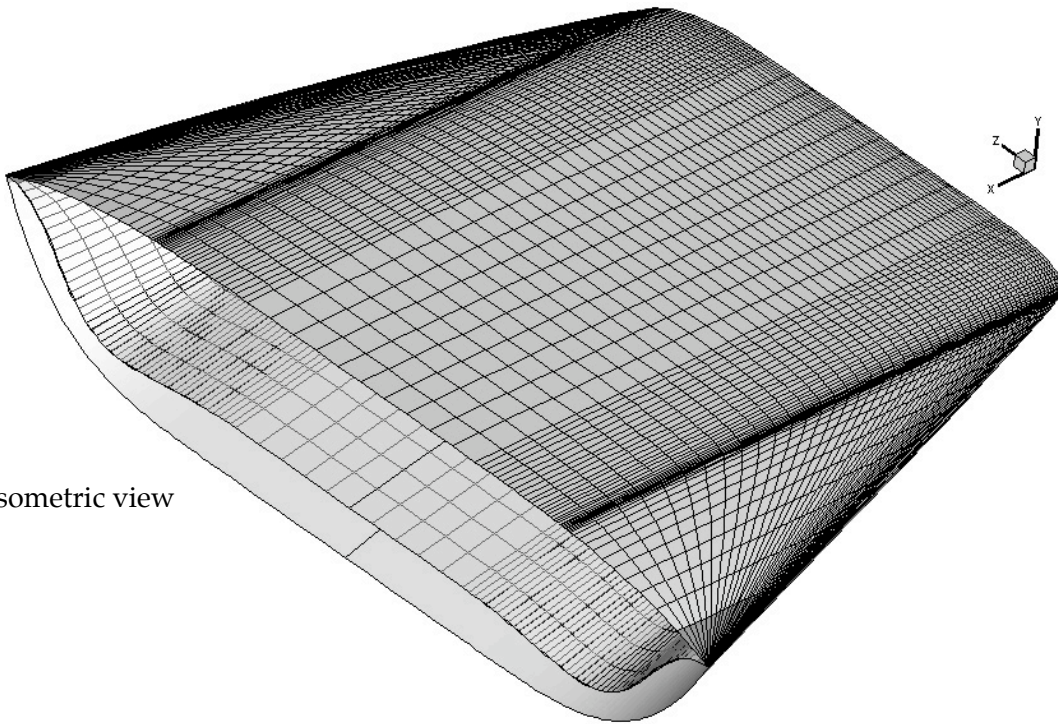
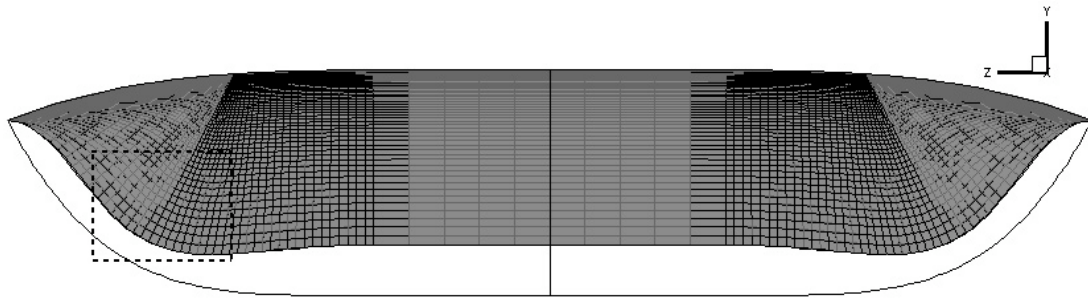
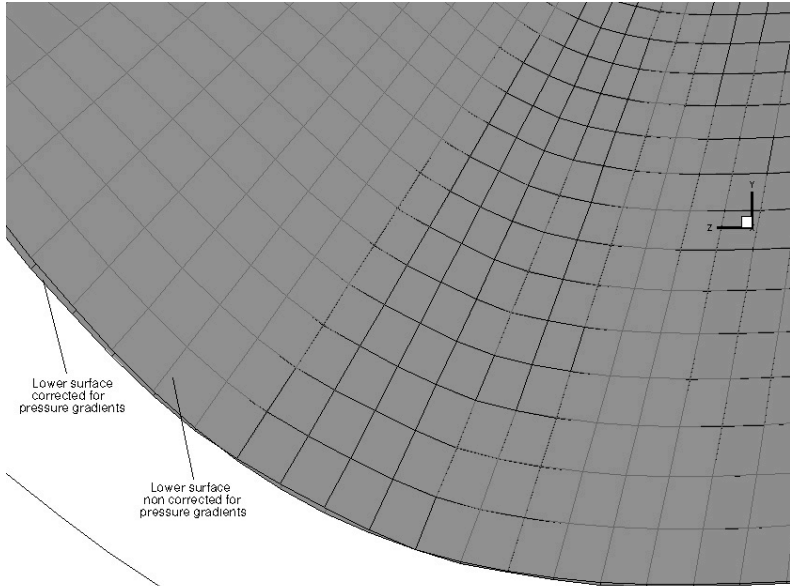


Fig. 2.11 Mach 10 osculating cones waverider

Mach 15 Waverider



Base view



Isometric view

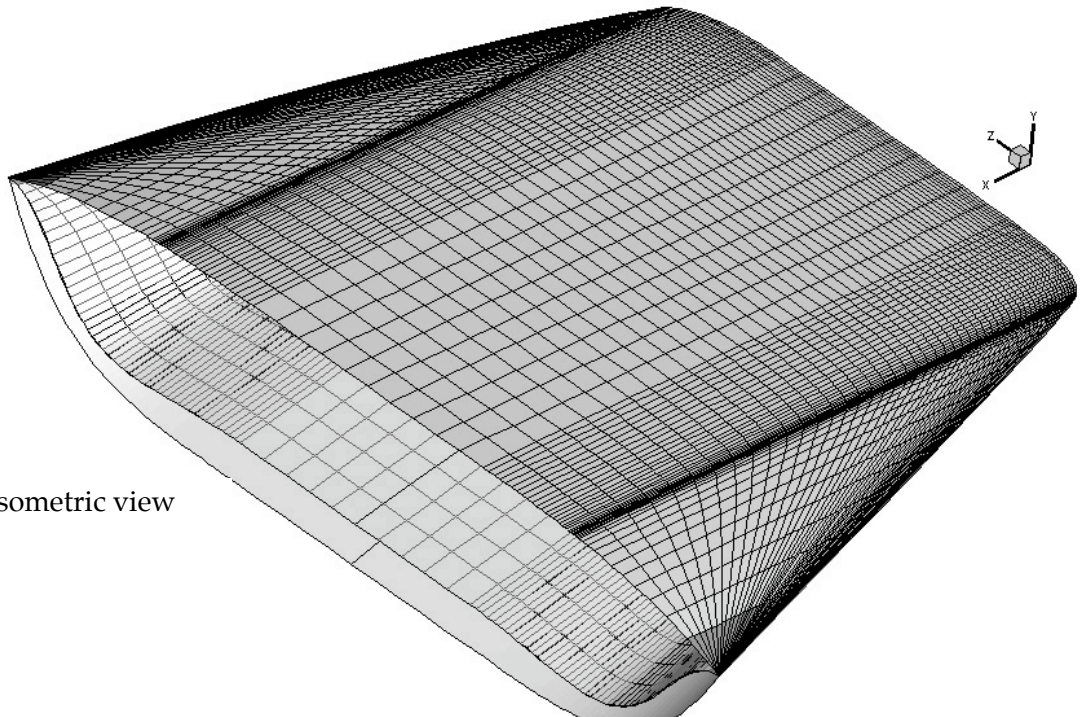


Fig. 2.12 Mach 15 osculating cones waverider

Chapter 3

Hypersonic On-Design Performances

3.1 Hypersonic Performances Prediction

The analytical solution of the osculating cones generating flowfield predicts the flowfield properties at on-design conditions, within all the shock layer of the waverider. The flowfield pressure distribution is thus known at the lower surface and upper surface (freestream surface) of the waverider. Classically¹², the design code evaluates the inviscid aerodynamic performance of the waverider by integrating numerically the pressure over each 4-sided surface element of those two surfaces. Each surface element is first split into two triangles elements, as shown on Fig. 3.1.

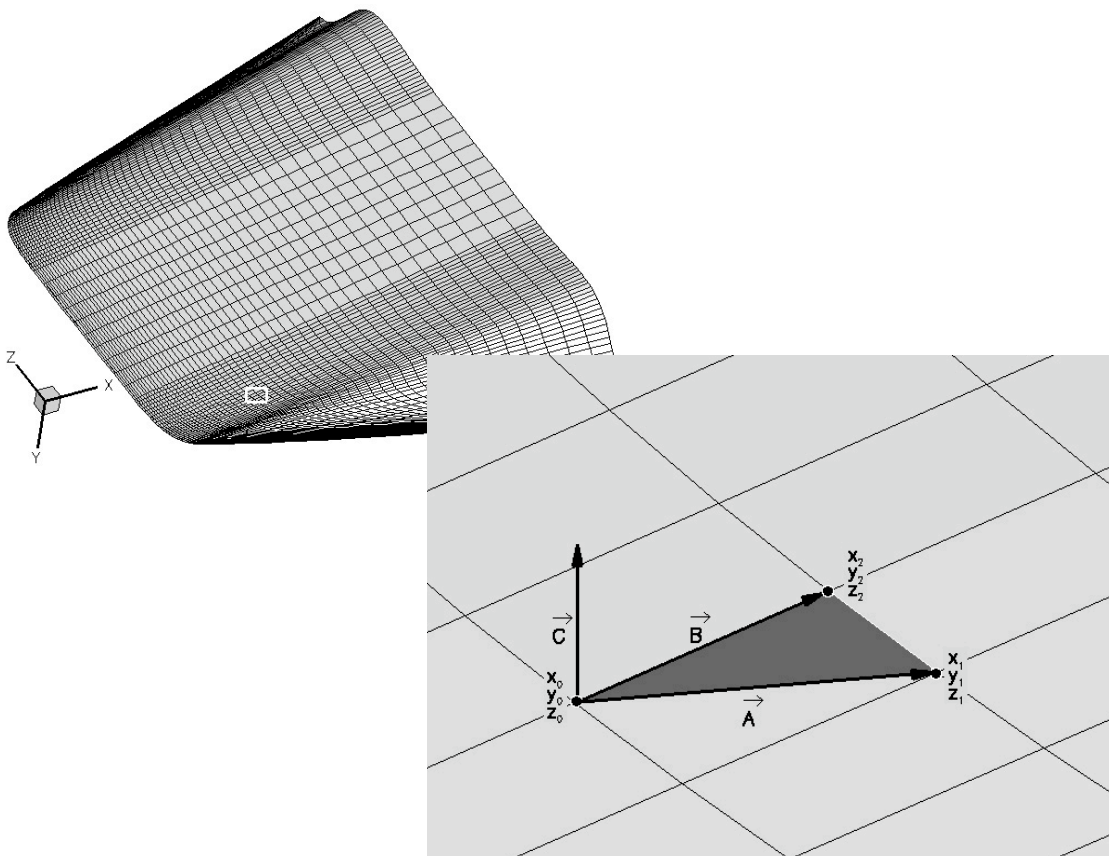


Fig. 3.1 Surface elements for force and area calculation

The wetted area of each triangle element is calculated from the cross product of its boundary vectors:

$$A_w = \frac{1}{2} \|\vec{C}\| = \frac{1}{2} \|\vec{A} \times \vec{B}\| \quad (3.1)$$

The forces acting on each triangular element is then calculated from the average of the pressure at the three corners:

$$P_{avg} = \frac{1}{3} (P_0 + P_1 + P_2) \quad (3.2)$$

The following relations give the lift and drag generated by the triangular element

$$L = P_{avg} A_w \frac{C_y}{\|\vec{C}\|} \quad (3.3)$$

$$D = P_{avg} A_w \frac{C_z}{\|\vec{C}\|} \quad (3.4)$$

At on-design conditions, the upper surface does not generate any drag since every surface element is aligned to the freestream direction. Thus, the total lift of the waverider is the sum of the lift created by each surface element of the lower surface and the upper surface, and the total drag is the drag generated by each surface element of the lower surface. The lift and drag coefficients are defined as follows,

$$C_L = \frac{L}{\frac{1}{2} \rho A_w V^2} \quad (3.5)$$

$$C_D = \frac{D}{\frac{1}{2} \rho A_w V^2} \quad (3.6)$$

where the total wetted area A_w is integrated numerically over the lower surface and upper surface.

3.2 Computational Method

3.2.1 Numerical Method

In order to evaluate the impact of the geometry modifications on the waverider flowfield, CFD simulations are run. The inviscid flowfield predicted by the analytical solution of the osculating cones generating flowfield is compared to the results from an inviscid CFD simulation. CFD-FASTRAN²⁹, a finite volume code, is used to solve the steady three-dimensional Euler compressible equations (see Appendix A) with a time marching scheme. Time-integration is achieved using a fully implicit scheme, repeated until the residuals decrease of at least 3 orders. Local time stepping is also used to accelerate convergence to steady state. At each time step, flux vectors are evaluated using Roe's upwind flux difference splitting, with an Osher-Chakravarthy flux limiter in order to achieve third-order spatial accuracy.

3.2.2 Computational grid

In order to perform three-dimensional CFD simulations of the flowfield around the waverider finite volume grids are constructed using an algebraic grid generator software, CFD-GEOM³⁰. The geometry of the waverider (compression surface and upper surface) is imported from the design code to the grid generator and modified in order to fulfill some grid requirements. The hypersonic on-design flow around a waverider is a hyperbolic problem, so the outer boundaries do not need to be far away from the body. The waveriders configurations investigated within this study are symmetric around the vertical plane xy , so the flow at a zero angle of attack around it is also symmetric around the same plane. To account for that planar symmetry and ease the computation, the grid can only model half of the flowfield around the waverider.

On-design waveriders configurations present the double challenge of a sharp leading edge, with a strong shock wave attached to it. The grid has to be locally refined in order to capture the solutions details at the leading edge and to sharply resolve the gradients associated with the shock wave. Cells are clustered around the leading edge of the vehicle, and around the predicted location of the shock wave. Fig. 3.2-3.3 represent the grid in the base plane of the waverider.

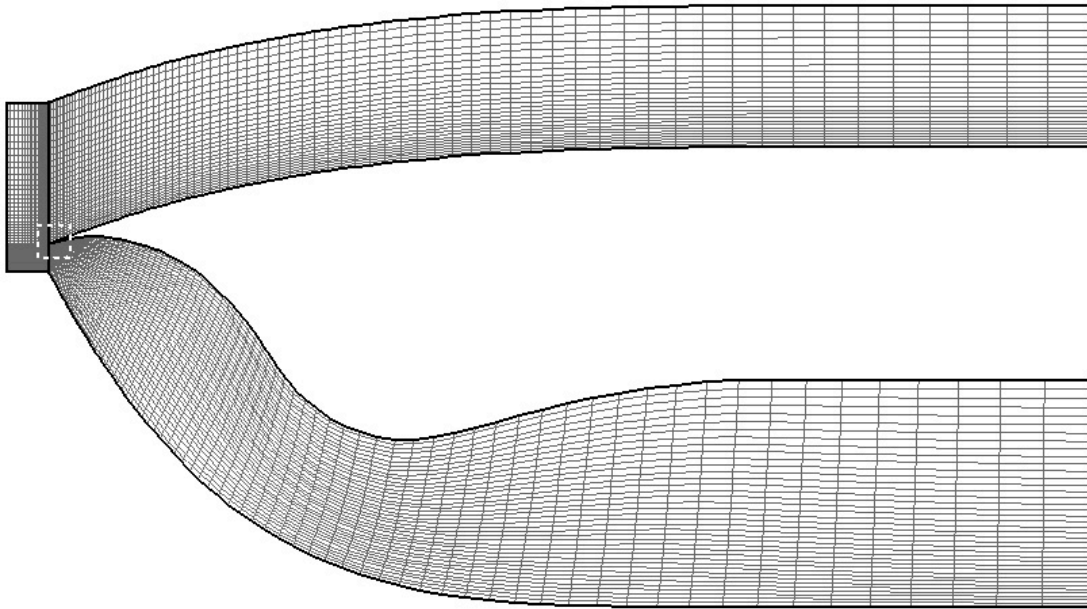


Fig. 3.2 Computational grid in the base plane

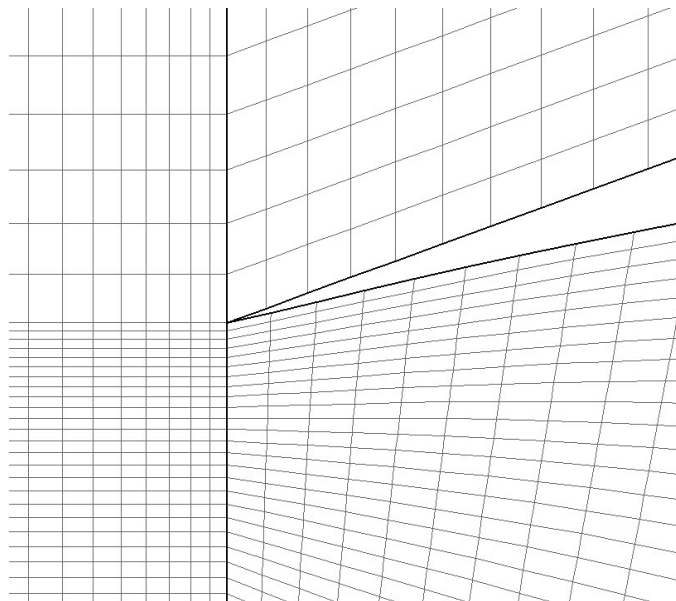


Fig. 3.3 Magnified grid near sharp leading edge

The computational grids are shock-fitted in order to capture precisely the flowfield, and get an accurate map of the flowfield distribution underneath the waverider. In addition the grids are also relatively fine in order to achieve high accuracy: 100x100x70 points (see Fig. 3.4-3.5).

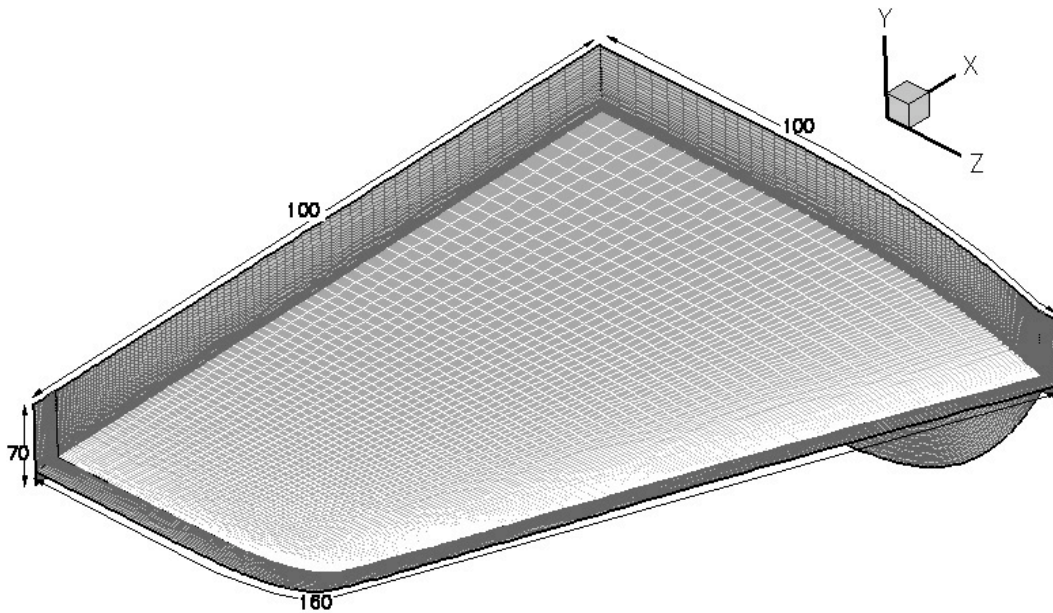


Fig. 3.4 computational grid, top view

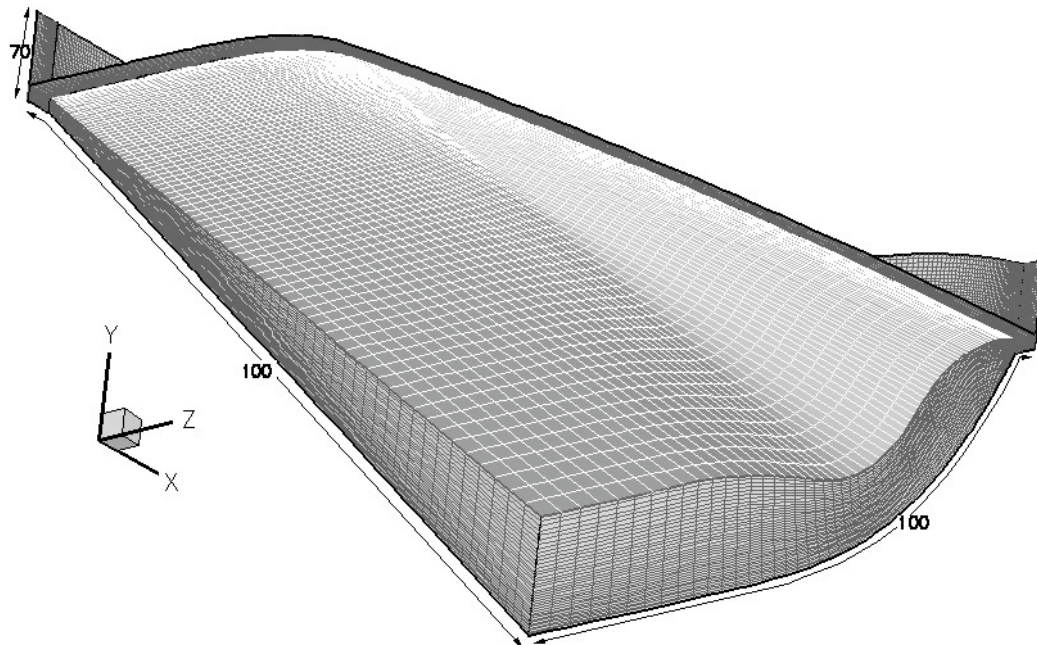


Fig. 3.5 Computational grid, bottom view

3.2.3 Boundary conditions and initial conditions

“Inlet” boundary conditions with a fixed mass flow rate are applied to the surfaces located upstream of the waverider. For all other farfield boundaries “Inflow-Outflow” boundary condition is used: the inlet flow conditions are used if the flow is entering the domain; extrapolated conditions from the interior of the grid to the boundary are calculated if the flow is leaving the domain. The wake boundaries are imposed as “Outlet” with extrapolated exit conditions: flow variables are extrapolated to the exit boundary from the interior of the domain. The waverider body is modeled as two adiabatic walls (no heat flux through the wall), and the symmetry planes by the “symmetry” boundary condition. The boundary conditions imposed for the CFD numerical model are represented in Fig. 3. 6-3.7.

Initial conditions are set for all simulations as the freestream conditions.

3.2.4 Solutions convergence criteria

The solutions were allowed to converge until the L_2 norm of the density residual dropped at least by three orders of magnitude. The change in lift, and drag had also to be less than 10^{-3} over 100 iterations.

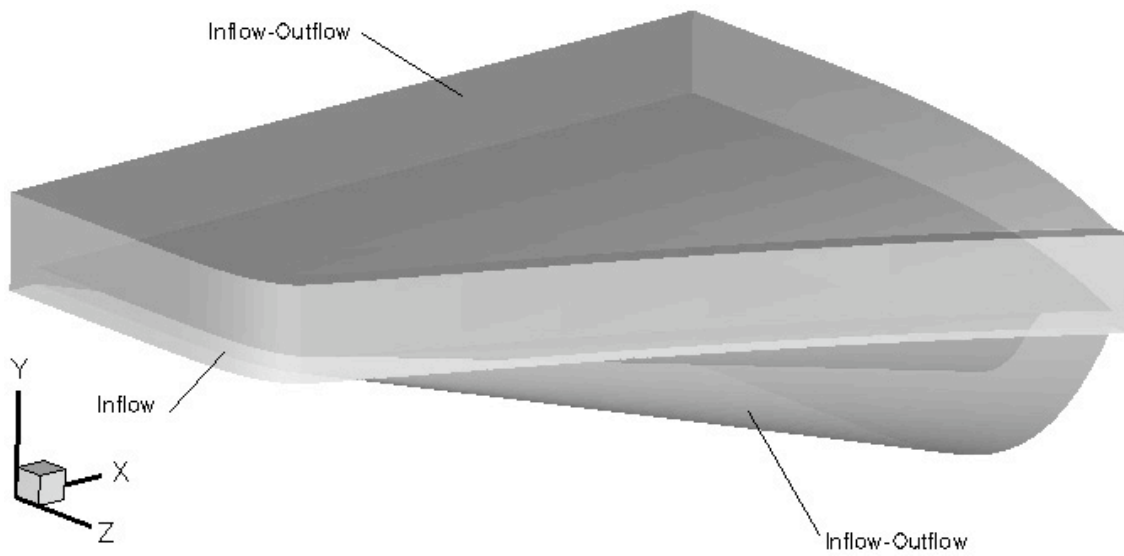


Fig. 3.6 Boundary conditions, front view of the computational grid

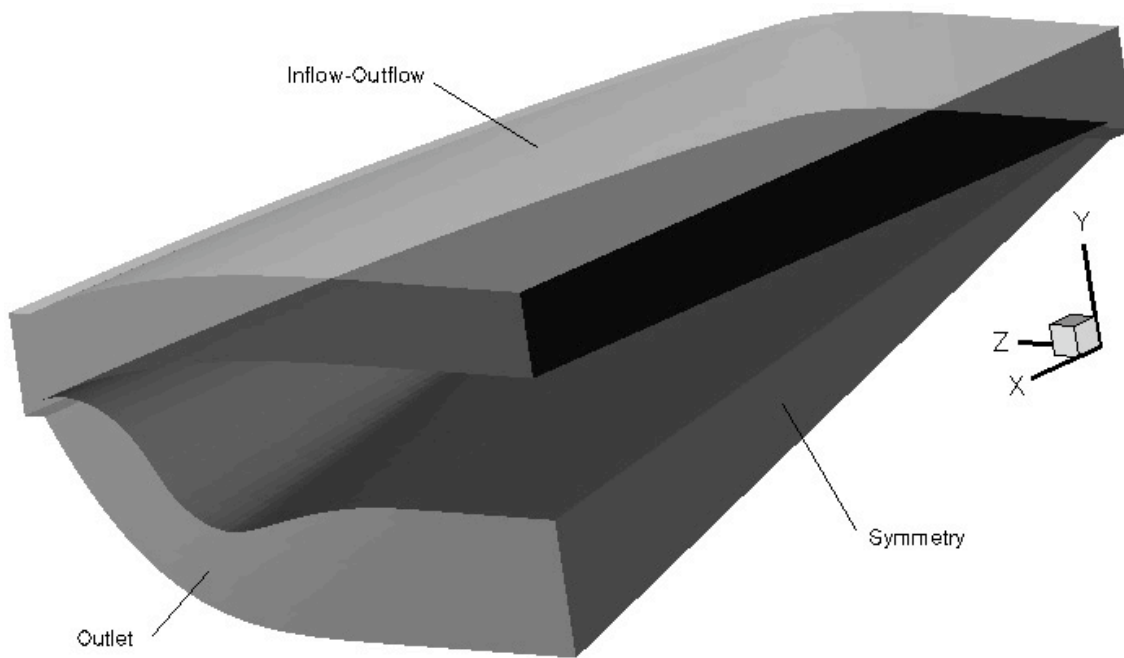


Fig. 3.7 Boundary conditions, rear view of the computational grid

3.3 CFD Simulations

3.3.1 Wedge-Derived Waverider M=6

Geometry Derivation

The wedge-derived waverider generates a portion of a planar shock wave, and is a limiting case of the osculating cones waverider- the waverider is derived from a SWPC with a constant infinite radius of curvature. The on-design prescribed conditions are given in Table 3.1. The waverider generated from the prescribed USPC, and SWPC in the base plane is presented in Fig. 3.8.

Table 3. 1 Design conditions of a Mach 6 waverider

M	6.0
\square	17°
<i>Length</i>	5 m
<i>Flight Altitude</i>	28.37 km
P	1528 .49 Pa
T	224.894 K
U	1803.62 m.s ⁻¹

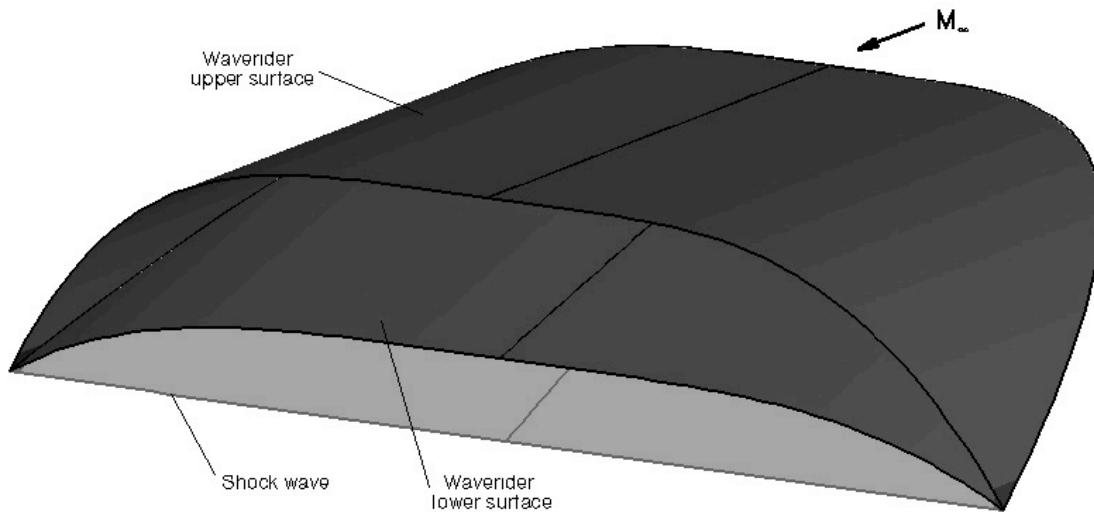


Fig. 3.8 Mach 6 wedge-derived waverider

Flowfield Distribution

The analytical solution for the wedge-derived waverider predicts a uniform flowfield behind the shock wave. The uniform flowfield properties are derived from the oblique shock relations at the prescribed design conditions.

For this waverider configuration, the CFD simulation matches exactly the prediction. The shock wave is captured accurately by the present computational method, as it is spread on only a relatively small distance. As expected from the analytical solution, the shock is attached to the leading edge of the waverider all along the geometry. The shock layer (i.e. zone enclosed between the shock wave and the lower surface of the waverider) flowfield is uniform, and matches exactly the predictions of the generating flowfield, as it can be observed on the comparison of the normalized pressure contours plots between the analytical solution and the Euler simulation (see Fig. 3.9).

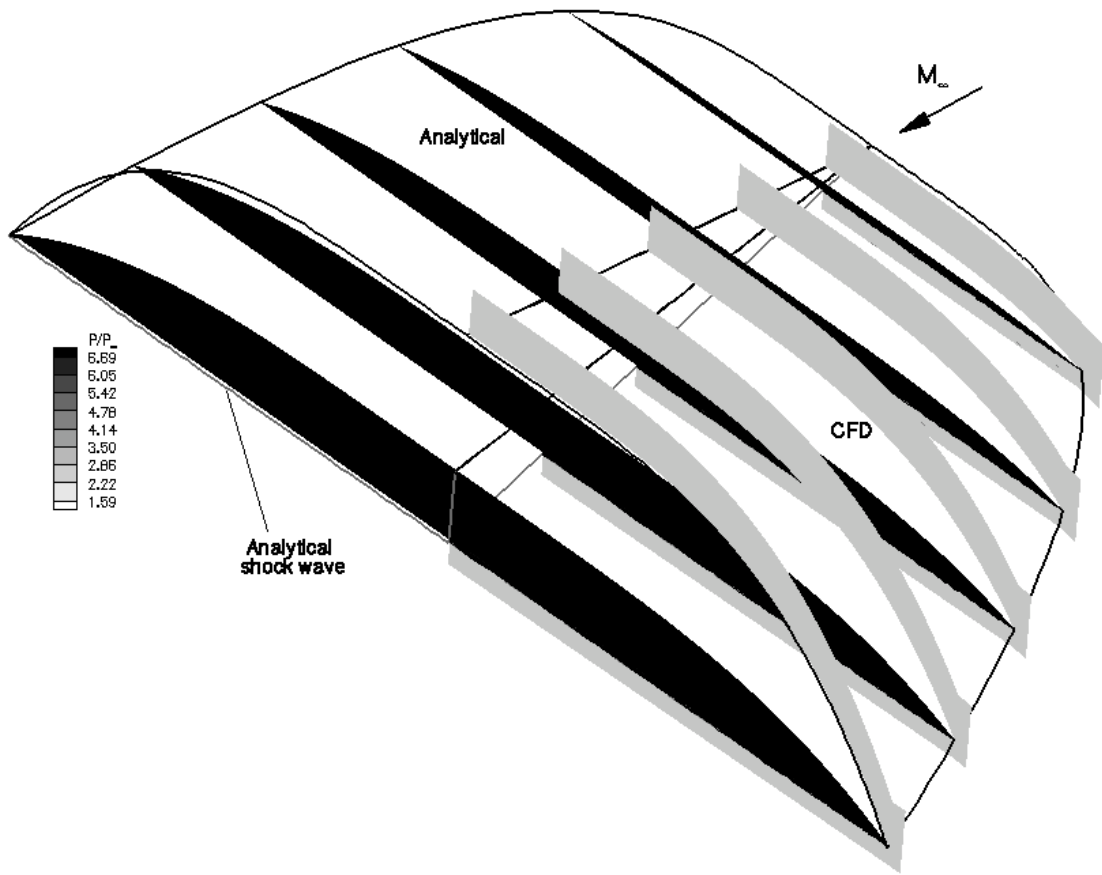


Fig. 3.9 Comparison of normalized pressure contours over Mach 6 waverider

Aerodynamic Performance

The inviscid on-design aerodynamic performance of the waverider is investigated by comparing the values predicted by the analytical solution from the design code, and the CFD Euler results. Table 3.2 summarizes those results at the on-design Mach number of 6. The lift and drag coefficients, and L/D ratio exhibit an error less than 0.1%, which demonstrates the perfect agreement between the Euler CFD simulation and the analytical inviscid prediction from the design code. Those results confirm also the previously observed agreement between the analytical prediction and the CFD solution for the flowfield distribution.

Table 3.2 Aerodynamic performance of a Mach 6 waverider

	Design	CFD	% diff.
C_L	0.11835	0.11818	0.085
C_D	0.04225	0.04219	0
L/D	2.80143	2.80092	0.018

3.3.2 Cone-Derived Waverider M=6

Geometry Derivation

A cone-derived waverider generates a shock wave which is a portion of a conical shock wave, and is a limiting case of the osculating cones waverider- the waverider is derived from a SWPC with a constant finite radius of curvature. The on-design prescribed conditions are given in Table 3.3. It is to be noted that here the shock wave angle β is the conical shock angle, contrary to the previous case where β was the wedge shock angle. The waverider generated from the prescribed USPC, and SWPC is presented in Fig. 3.10.

Table 3.3 Design conditions of a Mach 6 waverider

M	6.0
β	30°
<i>Waverider Length</i>	5 m
<i>Flight Altitude</i>	28.37 km
P	1528.49 Pa
T	224.894 K
U	1803.62 m.s ⁻¹

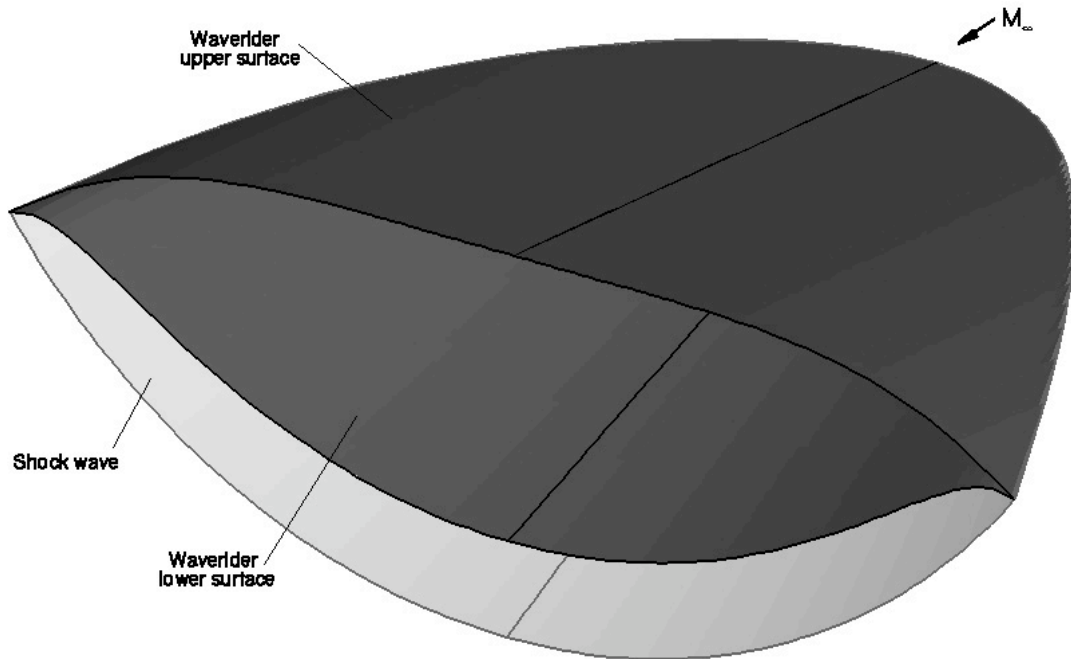


Fig. 3.10 Mach 6 cone-derived waverider

Flowfield Distribution : Euler Simulation

The analytical solution for the cone-derived waverider predicts a portion of conical flowfield behind the shock wave. The analytical flowfield distribution of the waverider is derived from the generating cone shock layer.

The Euler simulation agrees very well qualitatively and quantitatively with the analytical solution. The shock wave is captured over a very short distance, and thus the associated gradients can also be calculated accurately by the CFD solution. The comparison of the normalized pressure contours in Fig. 3.11, exhibits that the CFD confirms the prediction of the analytical solution, as the shock wave is properly attached along the entire leading edge of the waverider. In Fig. 3.12-3.14, the normalized pressure range is narrowed down to a smaller range, and compared at the lower surface of the waverider, and at different cross-section planes. The flowfield resulting from the Euler simulation matches very closely the analytical

solution, as the waverider generates a section of conical flow almost identical to the prescribed generating flowfield.

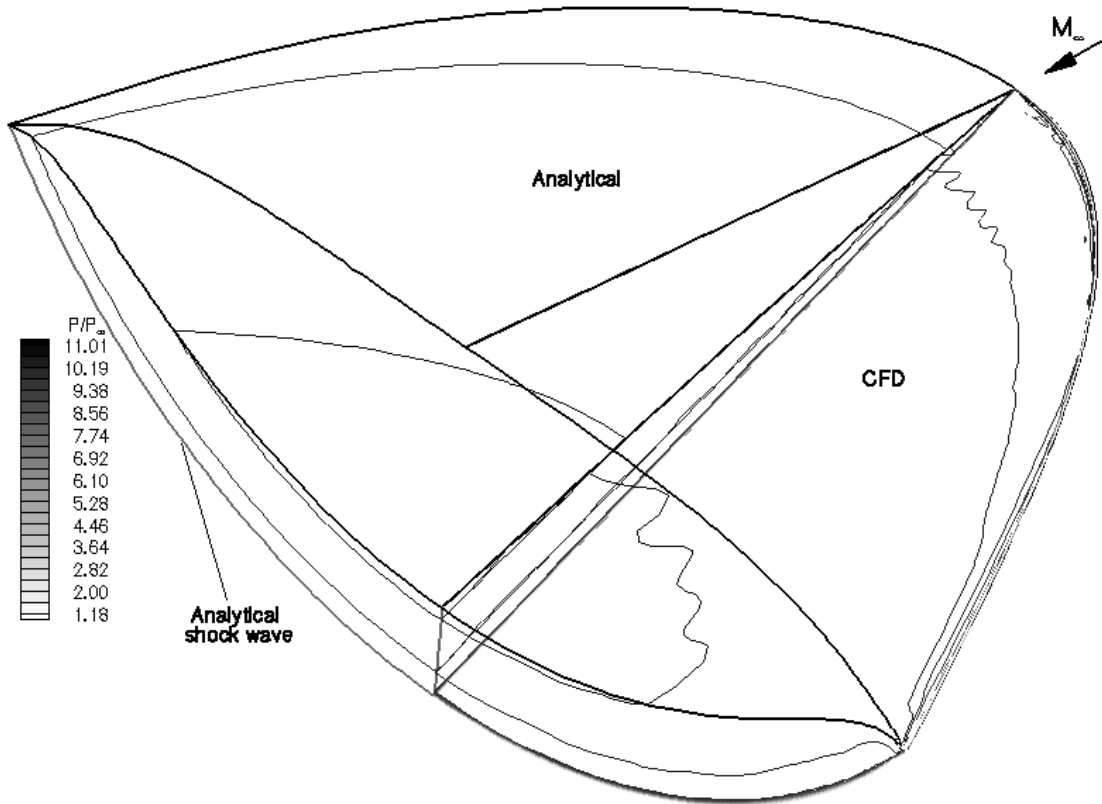


Fig. 3.11 Comparison of normalized pressure contours over Mach 6 waverider, Euler simulation

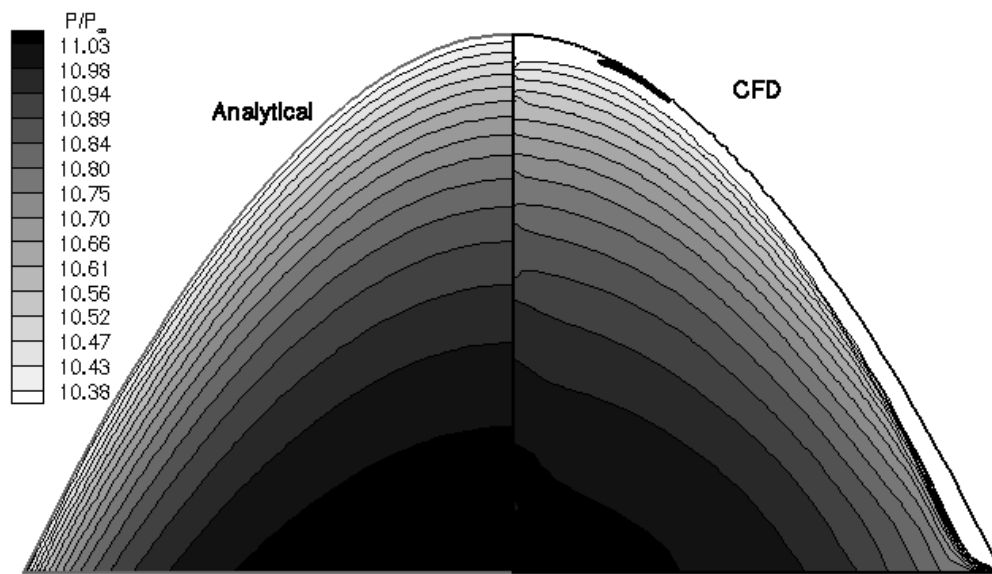


Fig. 3.12 Comparison of normalized pressure contours over lower surface of Mach 6 waverider, Euler simulation

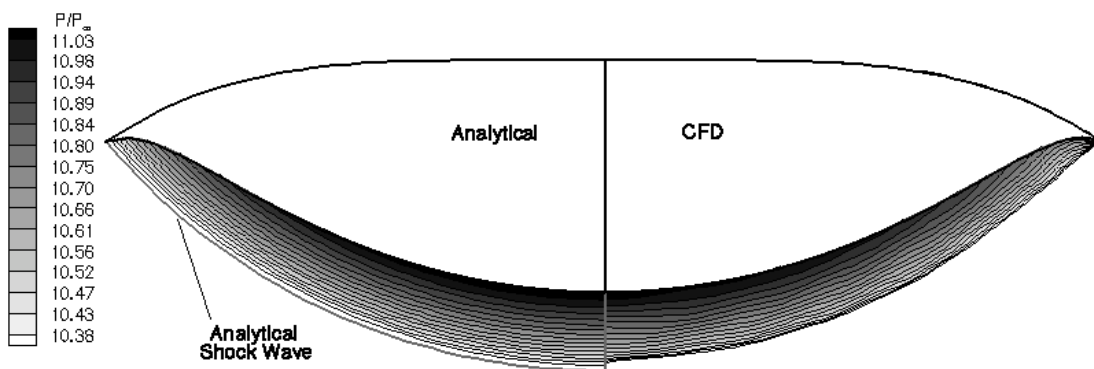


Fig. 3.13 Comparison of normalized pressure contours over Mach 6 waverider, base plane, Euler simulation

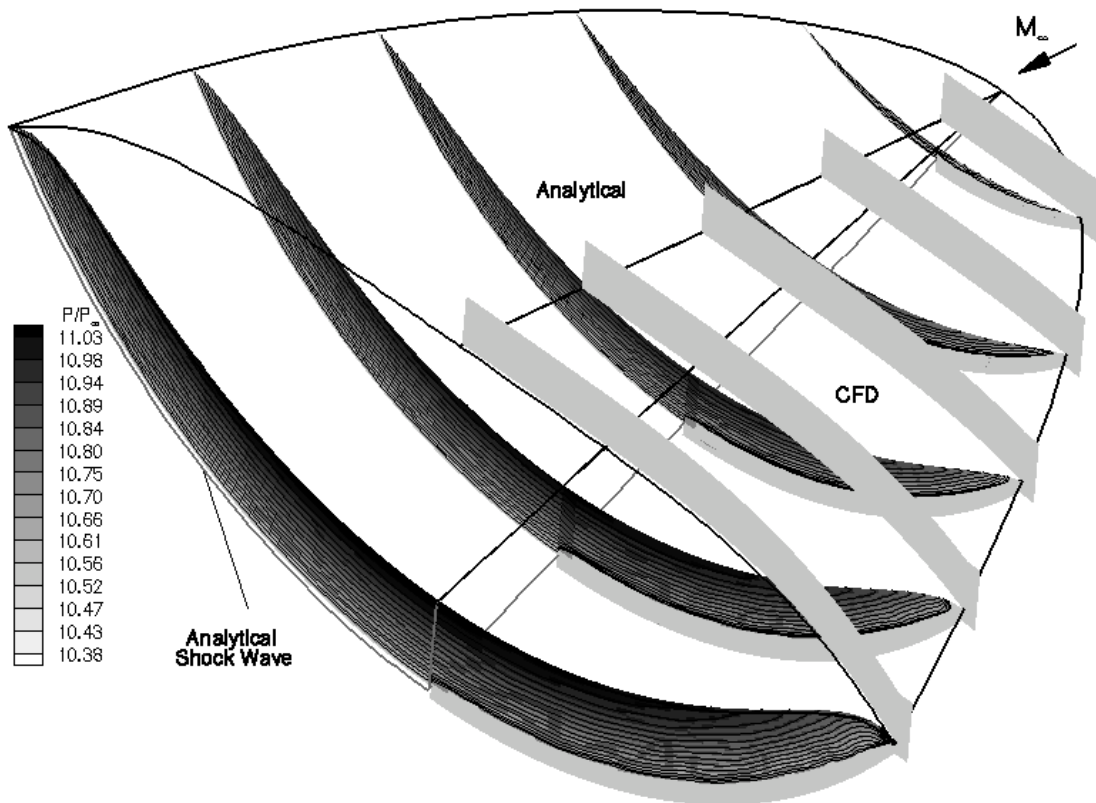


Fig. 3. 14 Comparison of normalized pressure contours over Mach 6 waverider, Euler simulation

Aerodynamic Performance : Euler simulation

As expected from the close agreement of the pressure distribution between the Euler simulation and the analytical prediction, the L/D match also very well (within 0.05%), as shown in Table 3.4.

Table 3.4 Comparison of aerodynamic performance of a Mach 6 waverider, Euler simulation

	Design	CFD	% diff.
C_L	0.18141	0.18089	0.276
C_D	0.08827	0.08806	0.227
L/D	2.05524	2.05427	0.049

Flowfield Distribution: Navier-Stokes Simulation

The normalized pressure distribution from the CFD simulation with viscous conditions is close to the inviscid analytical solution. From the isometric view on Fig. 3.15, it can be observed that the shock wave is captured over a small distance by the computational method. Furthermore, the location of the shock wave is matching the prescribed inviscid conditions. The viscous CFD results show that the shock is attached to the entire leading edge of the geometry. This demonstrates the validity of the waverider design at realistic flowfield conditions, even if the technique is based on the inviscid flow theory.

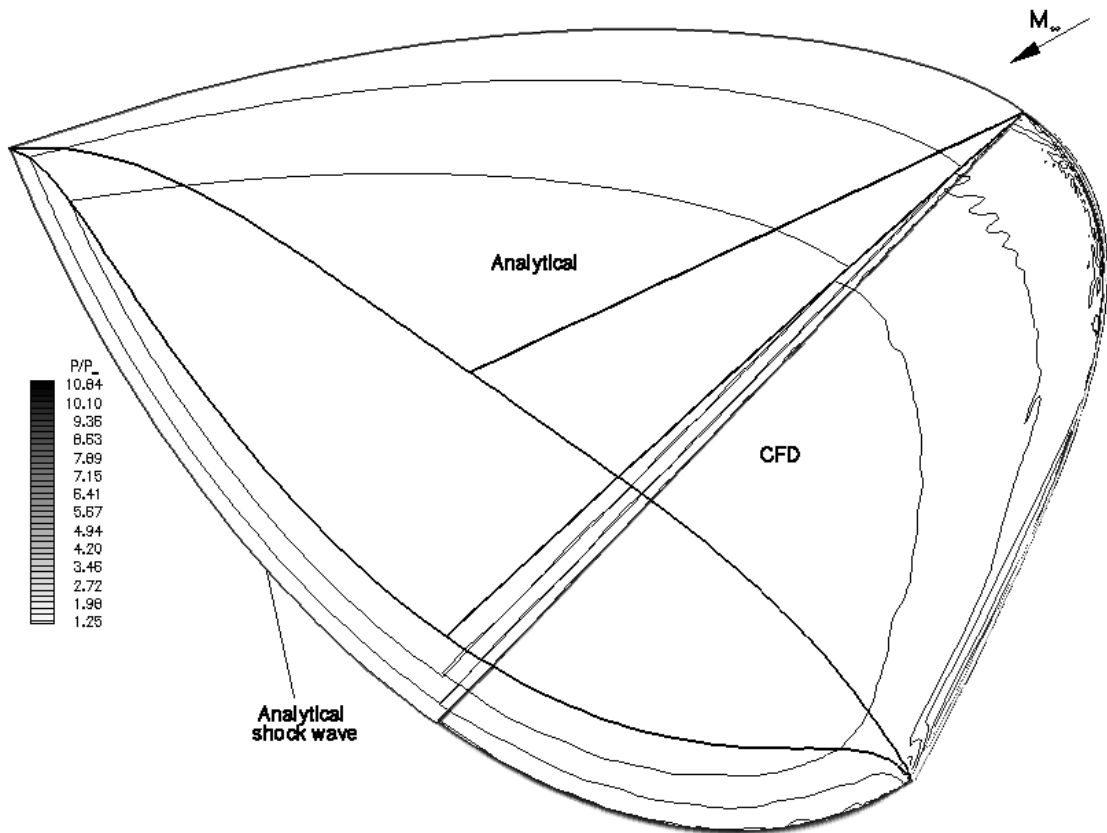


Fig. 3.15 Comparison of normalized pressure contours over Mach 6 waverider, Navier-Stokes simulation

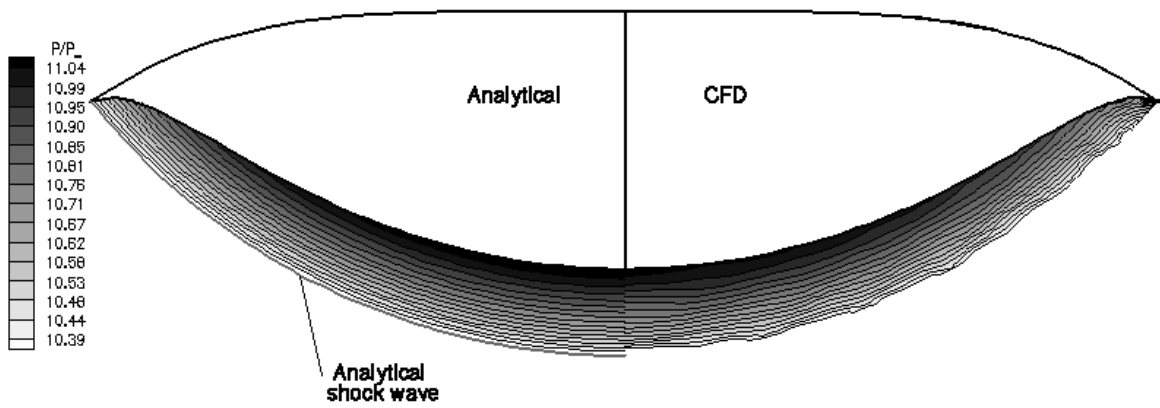


Fig. 3. 16 Comparison of normalized pressure contours over Mach 6 waverider, base plane, Navier-Stokes simulation

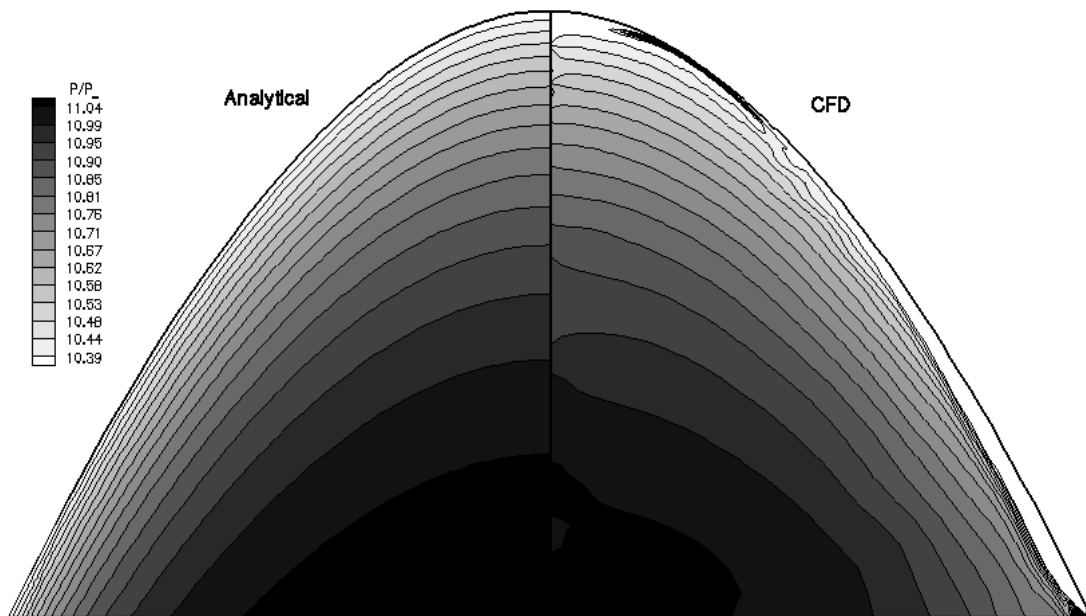


Fig. 3.17 Comparison of normalized pressure contours over Mach 6 waverider, lower surface, Navier-Stokes simulation

The normalized pressure contours at the base plane (see Fig. 3.16), and over the lower surface of the waverider (see Fig. 3.17) show again a good agreement between the analytical inviscid solution and the viscous CFD results. However, comparing those contours to the inviscid CFD results, it can be seen that the viscous run is further away from the prescribed flowfield distribution than the inviscid run. This is easily explained by the fact that the prescribed generating flowfield of the waverider is derived from the inviscid flowfield theory within each osculating cones stripe.

Aerodynamic Performance: Navier-Stokes simulation

The aerodynamic performance (see Table 3.5) from the viscous CFD simulation agrees very closely to the analytical inviscid solution. This correlates the previous comparison of the flowfield distribution, as the Navier-Stokes results and the analytical results are qualitatively matching. The addition of the viscous terms in the equations solved by the CFD code results in supplementary terms added to the integrated performance: the magnitude of the lift and drag coefficient is more important than the inviscid CFD performance.

Table 3.5 Comparison of aerodynamic performance of a Mach 6 waverider, Navier-Stokes simulation

	Design	CFD	% diff.
C_L	0.18141	0.18065	0.421
C_D	0.08827	0.08829	0.002
L/D	2.05524	2.04607	0.448

Given that the objective was to compare the prescribed inviscid flowfield, to the CFD corresponding solution, and that as observed inviscid and viscous simulations are quite close for waverider configurations, the following CFD simulations presented were run only at inviscid conditions.

3.3.3 Osculating Cones Waverider M=3

Geometry Derivation

As it was explained in Sec. 2.2, for this work the osculating cones waveriders are all derived from a geometrically similar SWPC. Waveriders are inversely designed in order to generate a shock planar at the centerline section, and curved (power-law curve) at the outboard section. Those shapes exhibit high gradients in the shock wave curvature, which results in extreme azimuthal pressure gradients. The two Mach 3 osculating cones waverider geometries (with and without pressure gradients corrections for the lower surface) derived by the design code at the following design conditions (see Table 3.6) were presented in Fig. 2.9.

Table 3.6 Design conditions of a Mach 3 waverider

M	3.0
\square	30°
<i>Waverider Length</i>	2.65 m
<i>Flight Altitude</i>	20.06 km
P	5480.32 Pa
T	216.65 K
U	885.127 m.s ⁻¹

Flowfield Distribution

The prediction for the shock wave generated by the waverider agrees very well with the CFD results for both the corrected and non-corrected waverider configuration. As it can be observed on Fig. 3.18, with the chosen computational method, the shock wave is captured over a very small distance. Contrary to previous waverider studies, the sharp gradients associated with the shock wave are exhibited by the CFD solution. Indeed for this work, the grid has been designed to be clustered at the predicted shock wave location. The CFD results confirm the attachment of the shock wave all along the leading edge of the waverider. The position of the analytical shock and the shock resulting from the Euler simulation is identical.

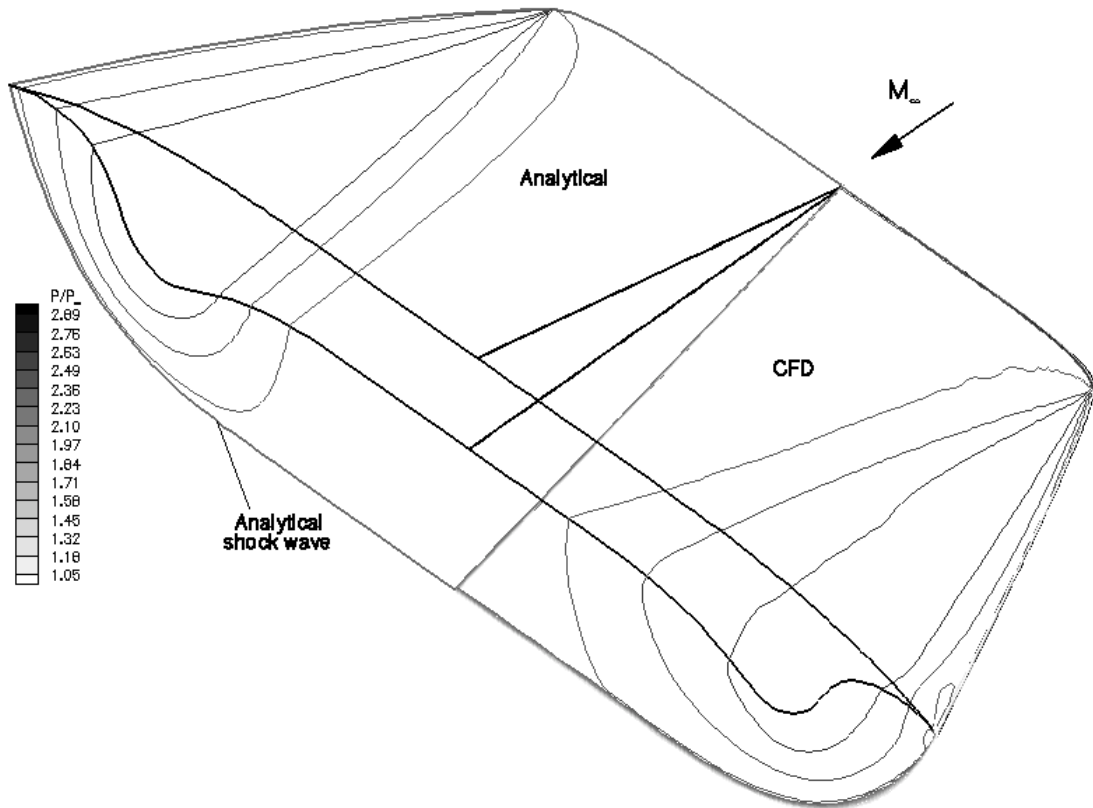


Fig. 3.18 Comparison of normalized pressure contours over Mach 3 waverider

The pressure contours are smeared off in the azimuthal direction. This results from the azimuthal pressure gradients that are quite large for the chosen shock shape. Those gradients are especially significant at low-Mach numbers, as it was already observed in this work for the derivation of low Mach numbers waveriders, in the previous chapter.

The shock is slightly detached from the leading edge of the waverider toward the end of the geometry. This trend observed both for the corrected and non-corrected waverider geometries result most probably from the resolution of the grid which is highly stretched in the streamwise direction in this area.

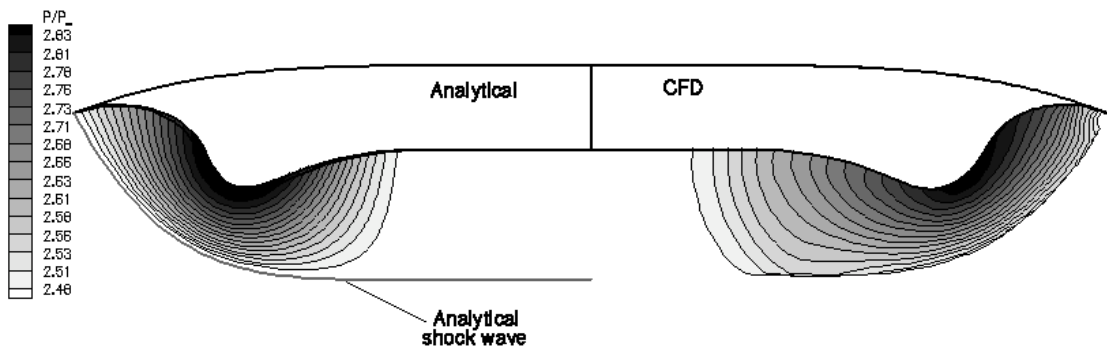


Fig. 3.19 Comparison of normalized pressure contours over Mach 3 modified waverider, base plane

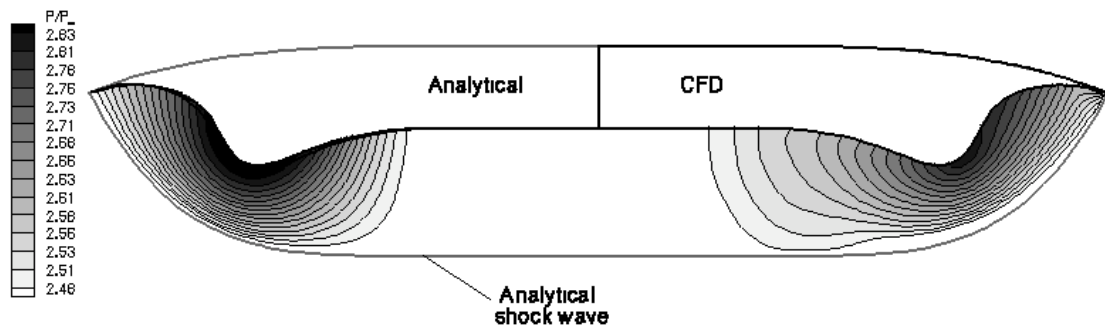


Fig. 3.20 Comparison of normalized pressure contours over Mach 3 non-modified waverider, base plane

As seen on Fig. 3.19, for the corrected configuration the normalized pressure distributions do not match exactly. This is in fact inherent to the way the analytical solution of the flowfield distribution is calculated by the design code. As the method modifies the lower surface- depending on the local magnitude of the pressure gradients, the flowfield compression resulting from that very surface is consequently also modified. The resulting changes in the pressure distribution are not be predicted by the code. In other terms, the analytical flowfield distribution is simply given by the osculating cones stripes flowfield distribution. However even with that mismatch of flowfield distributions for the analytical solution, the agreement with the CFD results is still pretty good. The pressure contours are smeared depending on the local pressure gradients: high-pressure contours tend to expand toward lower-pressure areas.

From the comparison of the CFD simulations presented in Fig. 3.20, it is observed that the osculating cones waverider without corrections generates a flowfield distribution which is also affected by the azimuthal pressure gradients, but which is also quantitatively further away from the prescribed flowfield in the base plane.

Form a vehicle integration standpoint, those figures show the importance to take into account the azimuthal pressure gradients at low Mach numbers. As observed, the supposed uniform section of the flow-, which is to be the flow entering the engine, is strongly affected by those pressure gradients. The flow is not uniform for almost half the cross section of the inlet.

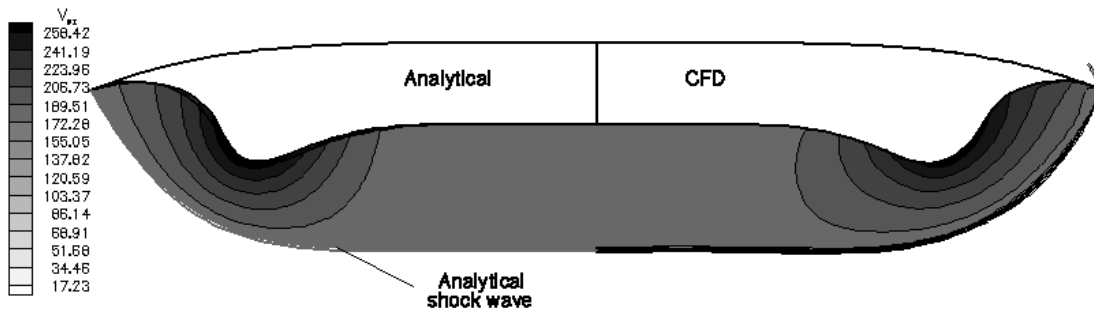


Fig. 3.21 Comparison of azimuthal velocity contours over Mach 3 modified waverider, base plane

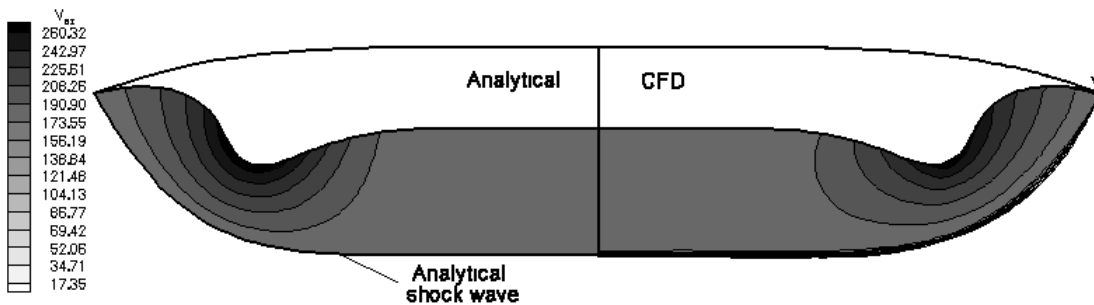


Fig. 3.22 Comparison of azimuthal velocity contours over Mach 3 non-modified waverider, base plane

The trends observed for the pressure contours are confirmed by the azimuthal velocity contours in Fig. 3.21-3.22. Remembering the Euler equation, the difference between the analytical and CFD azimuthal velocity contours gives indeed a quantitative indication of the azimuthal pressure gradients.

The normalized pressure contours over the lower surface also show that the present osculating cones waverider design method tend to generate geometries for which the flowfield distribution is qualitatively and quantitatively closer to the prescribed flowfield distribution. In particular, it can be observed in Fig. 3.23-3.24 that the high-pressure zone is better reproduced for the waverider with corrections.

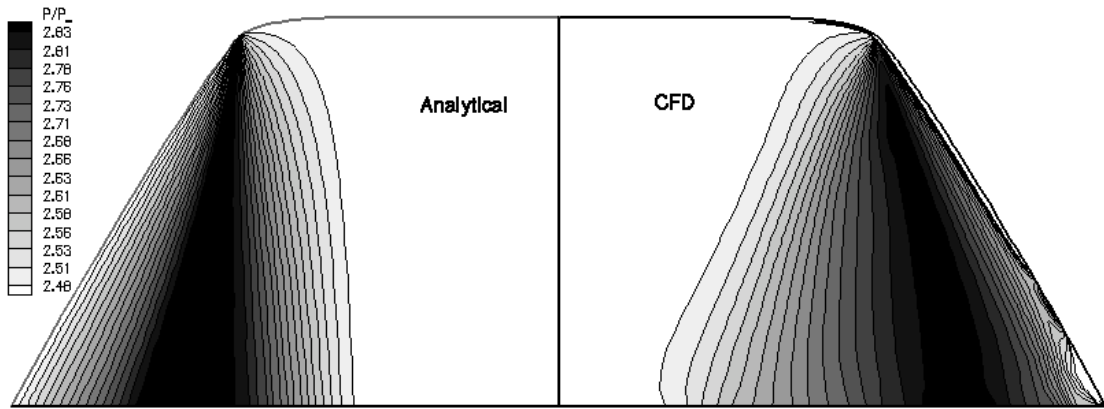


Fig. 3.23 Comparison of normalized pressure contours over lower surface of Mach 3 modified waverider

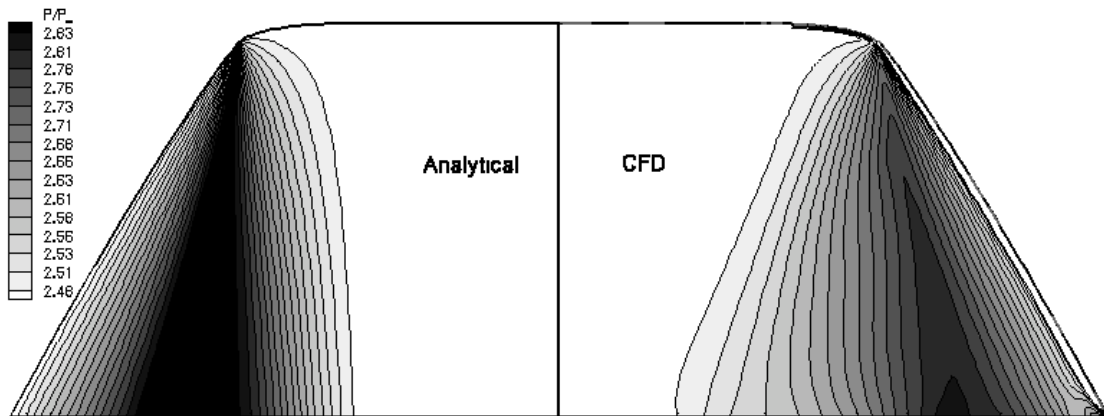


Fig. 3.24 Comparison of normalized pressure contours over lower surface of Mach 3 non-modified waverider

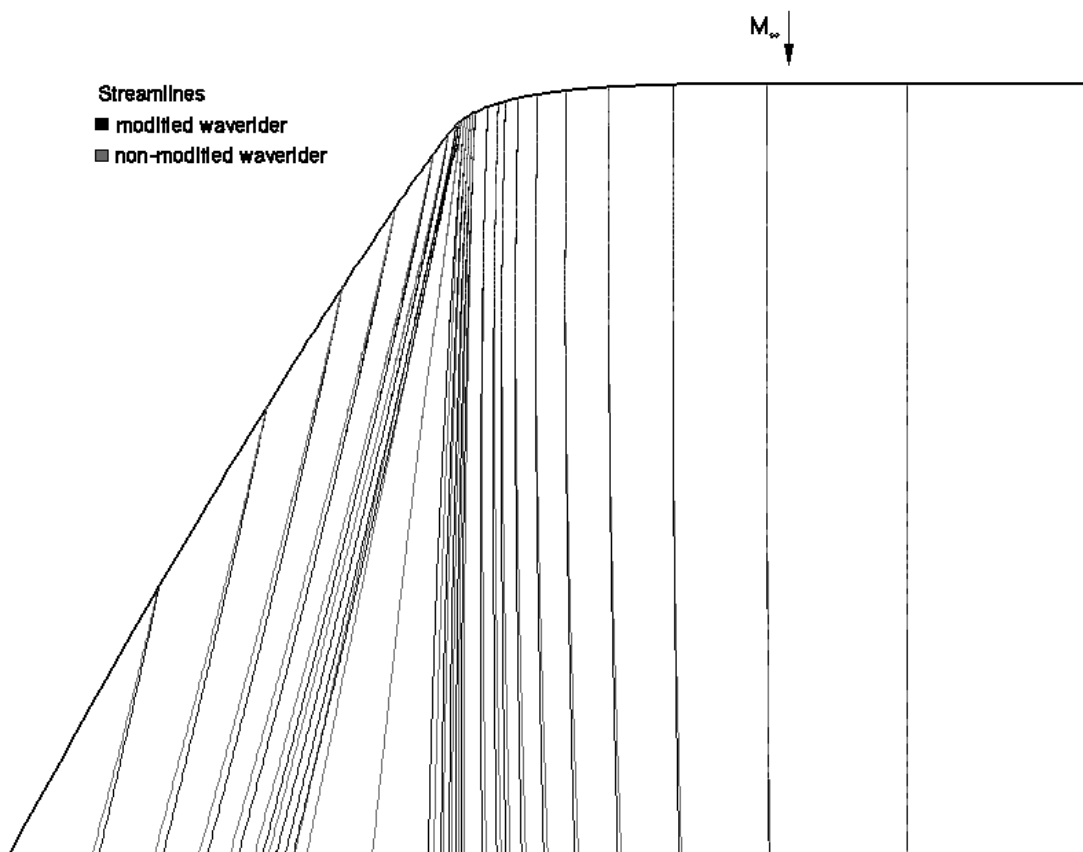


Fig. 3.25 Streamlines at the lower surface of a Mach 3 waverider

The results observed on the normalized pressure contours plots are confirmed by the streamlines tracing at the lower surface presented in Fig. 3.25 for the CFD solution for both the modified and non-modified waverider configuration. The streamlines tend to be moved from the high-pressure regions toward the lower-pressure regions according to the CFD results. For the present osculating cones design, the streamlines are less pushed away from their prescribed analytical location than for the previous design configuration. Especially in the inboard part of the geometry, the streamlines diverge less from their prescribed osculating planes position.

Aerodynamic Performance

For the present design method, the CFD and the analytical solution for the modified osculating cones waverider design show some discrepancy (2 % error for C_L). This discrepancy was explained previously, as the code does not predict the modified pressure distribution. However the agreement is still pretty good, and L/D ratios differ only by 0.9% (see Table 3.7).

For the waverider without pressure-gradients corrections, the comparison between CFD and the design C_L , C_D , and L/D show a very close agreement (less than 0.4% error).

The L/D of the corrected osculating cones waverider is slightly less than the L/D of the non-corrected osculating cones waverider (-1.17%). As it was observed previously on Fig. 3.23, the present design method generates geometries for which the compression surface is reaching higher pressure levels than waveriders designed without azimuthal pressure corrections. Consequently, the lift and drag are also higher (2.18% for C_L and for 3.39% C_D), but there is a light loss for the L/D as the gain in drag is more important (see Table 3.7-3.8).

Table 3.7 Comparison of aerodynamic performance of a Mach 3 waverider with lower surface corrected for pressure-gradients

	Design	CFD	% diff.
C_L	0.11934	0.12178	-1.999
C_D	0.05074	0.05128	-1.043
L/D	2.35142	2.37492	-0.989

Table 3.8 Comparison of aerodynamic performance of a Mach 3 waverider with lower surface non-corrected for pressure-gradients

	Design	CFD	% diff.
C_L	0.11932	0.11919	0.112
C_D	0.04976	0.0496	0.333
L/D	2.39773	2.40306	0.222

3.3.4 Osculating Cones Waverider M=6

Geometry Derivation

The two Mach 6 osculating cones waverider geometries (with and without pressure gradients corrections for the lower surface) derived by the design code at the following design conditions (see Table 3.9) were presented in Fig. 2.10.

Table 3.9 Design conditions of a Mach 6 waverider

M	6.0
α	17°
<i>Waverider Length</i>	5.0 m
<i>Flight Altitude</i>	28.37 km
P	1526.99 Pa
T	224.901 K
U	1803.65 m.s ⁻¹

Flowfield Distribution

The normalized pressure contours from the CFD solution and the analytical solution agree very well quantitatively and qualitatively (see Fig. 3.26). With the chosen computational method, the shock wave generated by the waverider is captured precisely, over a small distance. For the present CFD results, the shock wave is attached all along the leading edge and the location of the shock wave matches the prediction. The spreading in the azimuthal direction of the pressure contours is less than for the Mach 3 waverider. As the Mach number increases the flow tends to become unidirectional in the streamwise direction, as a result the influence of azimuthal pressure gradients becomes less important.

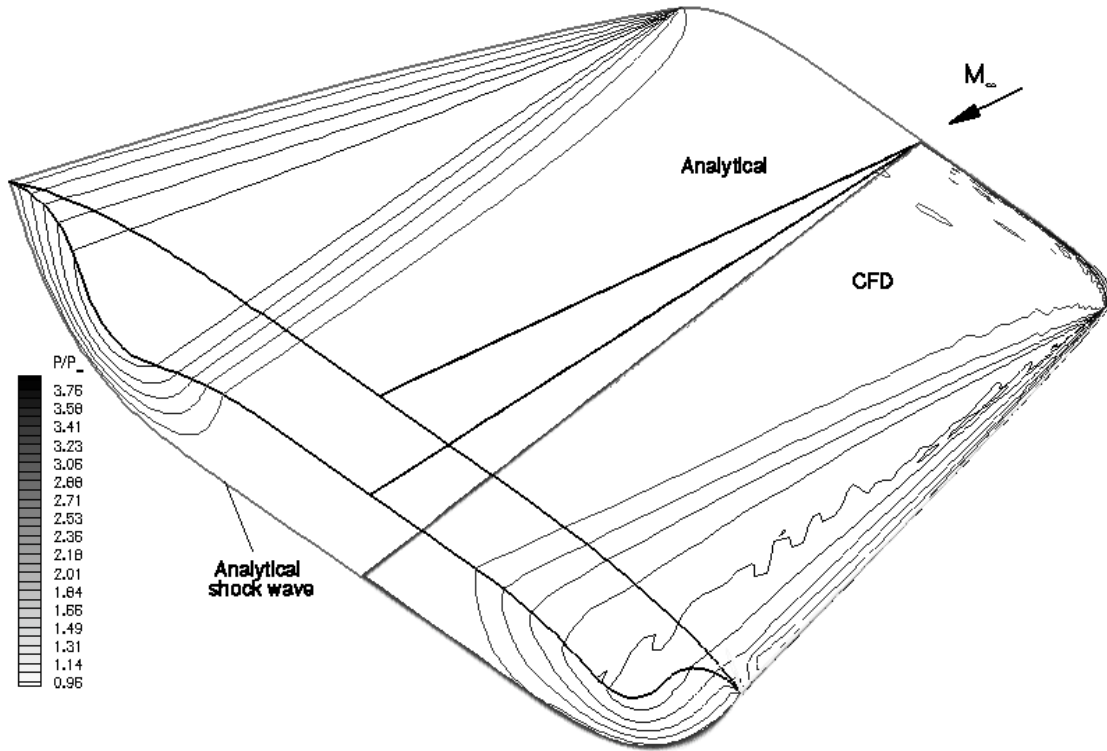


Fig. 3.26 Comparison of normalized pressure contours over Mach 6 waverider

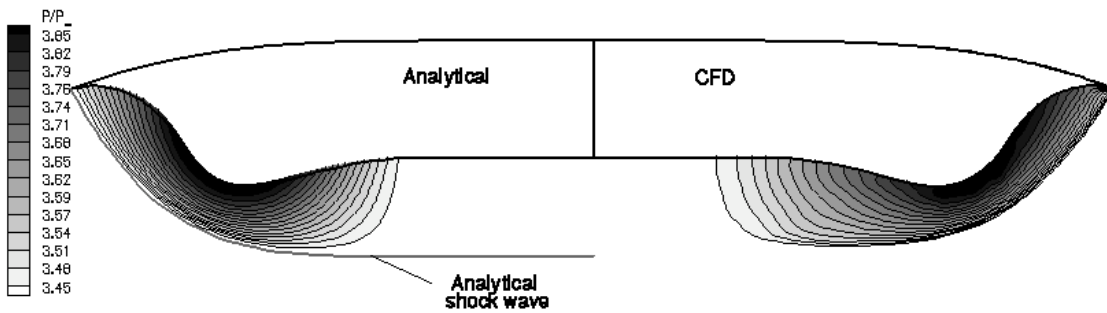


Fig. 3.27 Comparison of normalized pressure contours over Mach 6 modified waverider, base plane

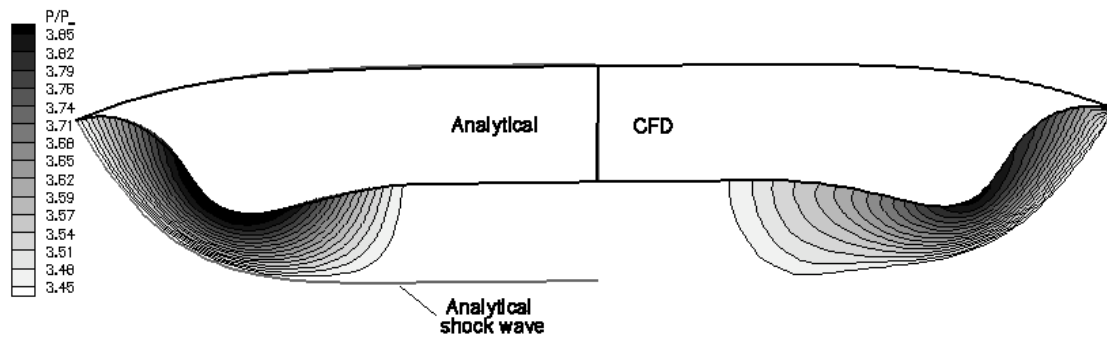


Fig. 3.28 Comparison of normalized pressure contours over Mach 6 non-modified waverider, base plane

From the normalized pressure contours in the base plane in Fig. 3.27-3.28, it can be observed that the flowfield around the present waverider design matches more precisely the flowfield distribution of the analytical solution than the previous osculating cones waverider methods. Compared to the previous case, the Mach number independence starts to prevail in that case. The differences between the waverider flowfields generated by the two different methods are much less perceptible than for the Mach 3 waveriders presented before.

The contours of azimuthal velocity in the base plane plotted on Fig. 3.29 –3.30 underlines the previously observed trends. The shock wave location is matching between CFD and analytical solutions for the two waveriders configurations. Qualitatively, the modified waverider is generating a flowfield closer to the prescribed conditions by the design code than the non-modified waverider.

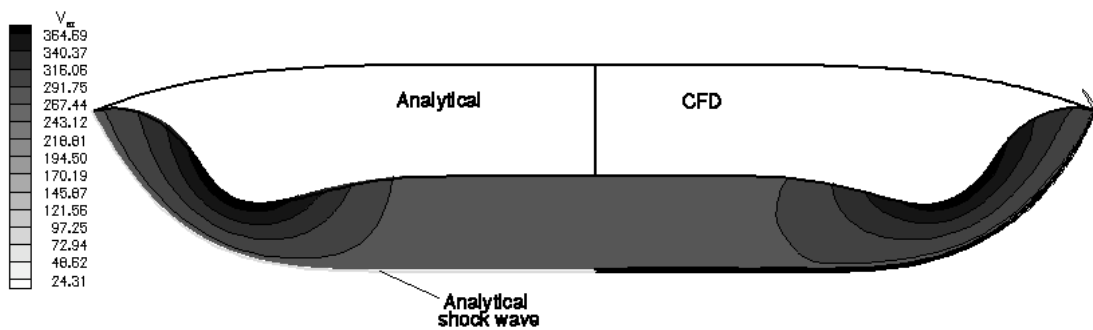


Fig. 3.29 Comparison of azimuthal velocity contours over Mach 6 modified waverider, base plane

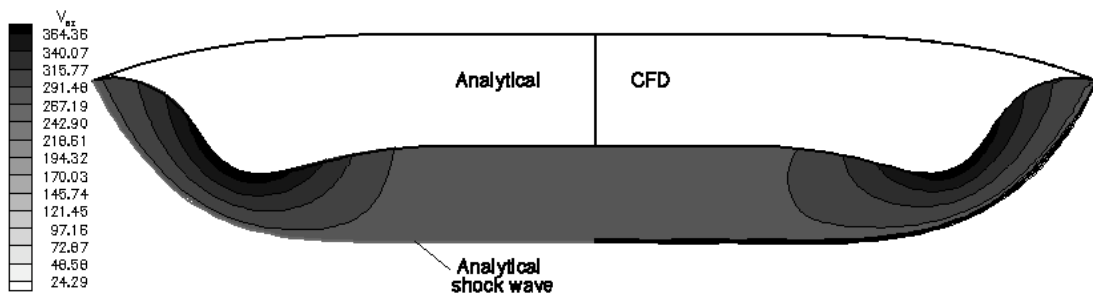


Fig. 3.30 Comparison of azimuthal velocity contours over Mach 6 non-modified waverider, base plane

The lower surface pressure contours (see Fig. 3.31-3.32) show the same trends than the previous case. The present modified osculating cones waverider design is matching qualitatively and quantitatively the analytical prescribed flowfield more closely than the previous designs.

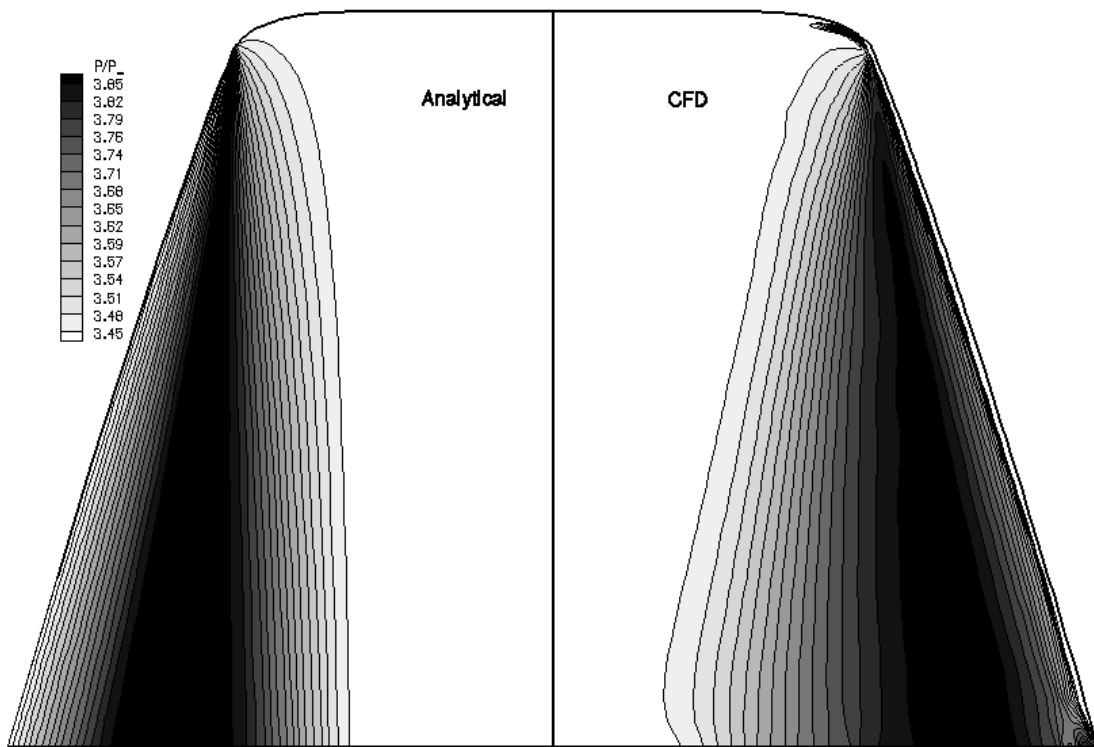


Fig. 3.31 Comparison of normalized pressure contours over lower surface of Mach 6 modified waverider

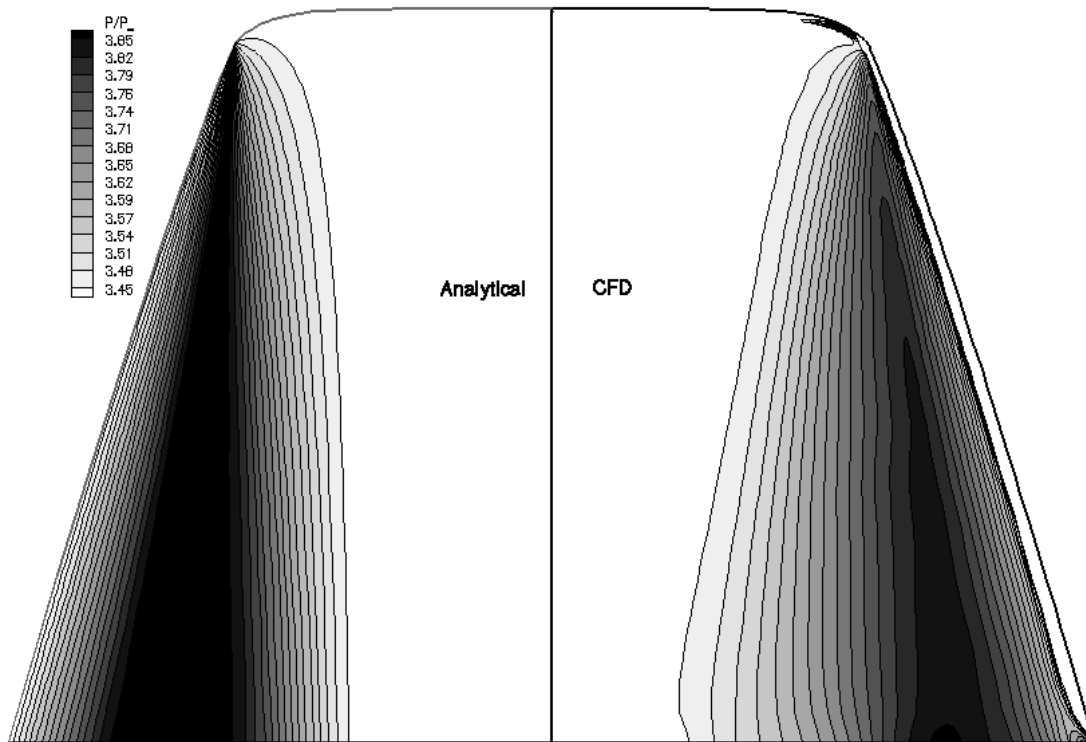


Fig. 3.32 Comparison of normalized pressure contours over lower surface of Mach 6 non-modified waverider

From the streamlines tracing presented in Fig. 3.33, it can still be observed that the streamlines are still slightly pushed outside their prescribed osculating planes. Indeed for those higher Mach number waverider configurations, the two streamlines maps are quite similar. The existence of azimuthal pressure gradients, demonstrated in the plot of the lower surface pressure contours, is dominated by the strong directional flowfield in the freestream direction. Thus the impact of those gradients is quite moderate on the streamlines, as seen on the CFD plots. Furthermore, those figures correlate the observations made in the previous chapter about the derivation of the waverider geometries: the modifications on the lower surface of the waverider (streamsurface) are minimal beginning at Mach 6.

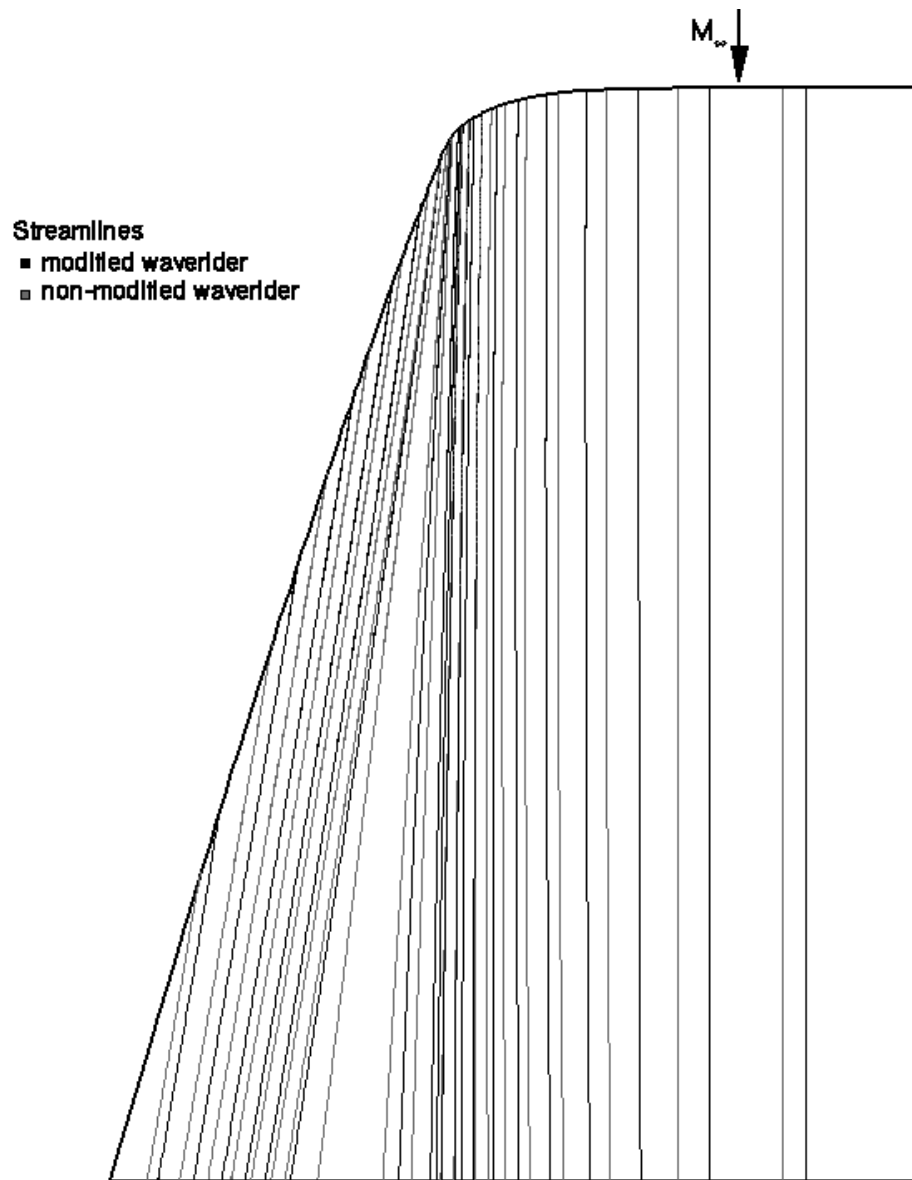


Fig. 3.33 Streamlines at the lower surface of a Mach 6 waverider

Aerodynamic Performance

As mentioned for the previous case, the errors between the CFD solution and the predicted analytical solution are higher for the present design than for previous osculating cones waverider design. However the error induced in the analytical code to calculate aerodynamic performance is fading away with increasing Mach number, as for this case the agreement is quite good, and L/D ratios differ only by 0.4% (see Table 3.10).

For the waverider without pressure-gradients corrections, the CFD aerodynamic performance matches almost exactly the analytical one (see Table 3.11).

The L/D ratio of the present osculating cones waverider design is slightly less than the L/D ratio of the previous osculating cones design (-0.66%). As pointed out previously, the influence of pressure gradients is here fading away. Also the two different design methods generate geometries very similar and consequently aerodynamic performance matches very closely.

Table 3.10 Aerodynamic performance comparison of a Mach 6 waverider with lower surface corrected for pressure gradients

	Design	CFD	% diff.
C_L	0.04905	0.04958	-0.106
C_D	0.01264	0.01272	-0.665
L/D	3.88139	3.8971	-0.402

Table 3.11 Aerodynamic performance comparison of a Mach 6 waverider with lower surface non-corrected for pressure gradients

	Design	CFD	% diff.
C_L	0.04905	0.04895	0.196
C_D	0.01251	0.01248	0.254
L/D	3.92065	3.9230	-0.061

3.3.5 Osculating Cones Waverider M=10

Geometry Derivation

The two Mach 10 osculating cones waverider geometries (with and without pressure gradients corrections for the lower surface) derived by the design code at the following design conditions (see Table 3.12) were presented in Fig. 2.11.

Table 3.12 Design conditions of Mach 10 osculating cones waverider

M	10.0
\square	17°
<i>Waverider Length</i>	5.0 m
<i>Flight Altitude</i>	35.14 km
P	563.483 Pa
T	236.892 K
U	3085.18 m.s ⁻¹

Flowfield Distribution

The normalized pressure contours from the CFD solution and the analytical solution agree well (see Fig. 3.34). The shock wave is captured in the azimuthal direction over a small distance, which is a result of the grid clustering at the predicted location of the shock wave. According to the CFD results, the shock is attached along the entire leading edge of the waverider and the location of the shock matches the prediction. The spreading in the azimuthal direction of the pressure contours is less than for the Mach 6 waverider, which underlines the predominant influence of increasing Mach number on the flowfield. As the Mach number goes up the flow become dominated by the flow in the freestream direction.

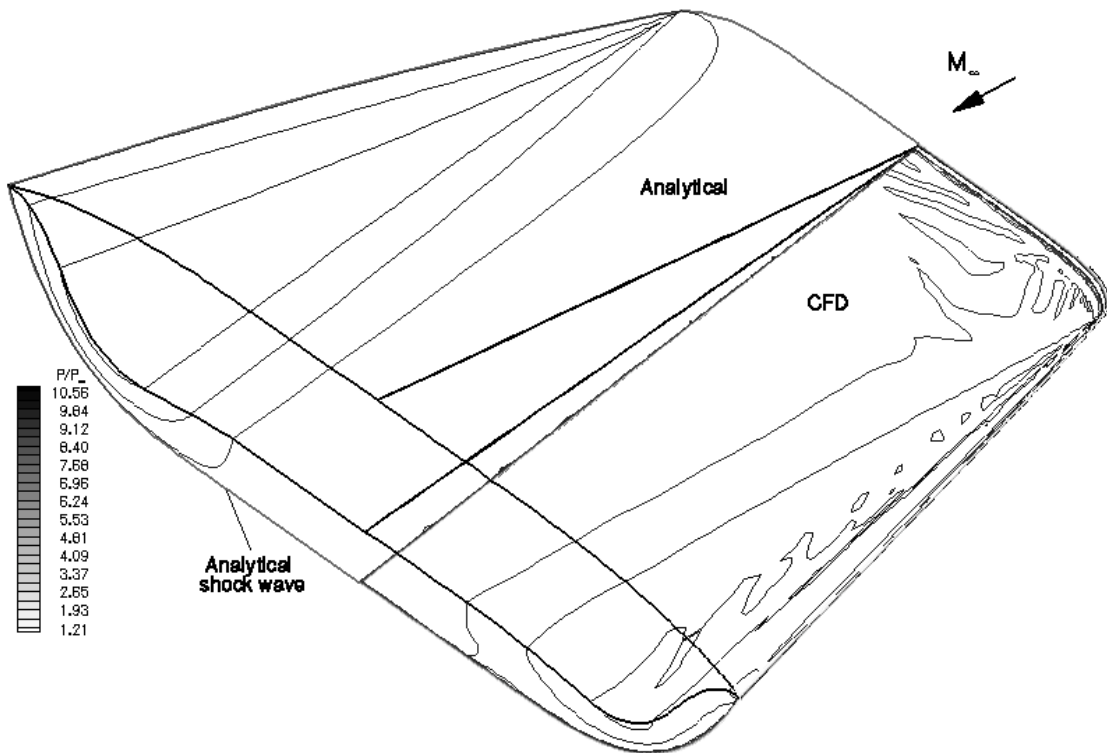


Fig. 3.34 Comparison of normalized pressure gradients over Mach 10 modified waverider

For this high Mach number configuration, the pressure contours display some dispersion errors for the sections of the flowfield located right after the shock wave. The Euler equations would certainly require a grid of higher resolution in order to capture the map of the pressure distribution more precisely in those areas. It is also possible that the high entropy change throughout the shock wave at such high Mach numbers causes numerical dissipation introduced by the entropy fix is used along with the Roe's scheme in order to make the solution converge.

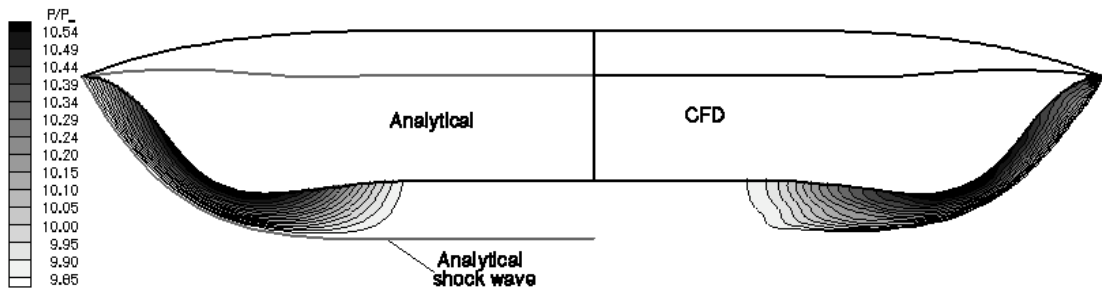


Fig. 3.35 Comparison of normalized pressure contours over Mach 10 modified waverider, base plane

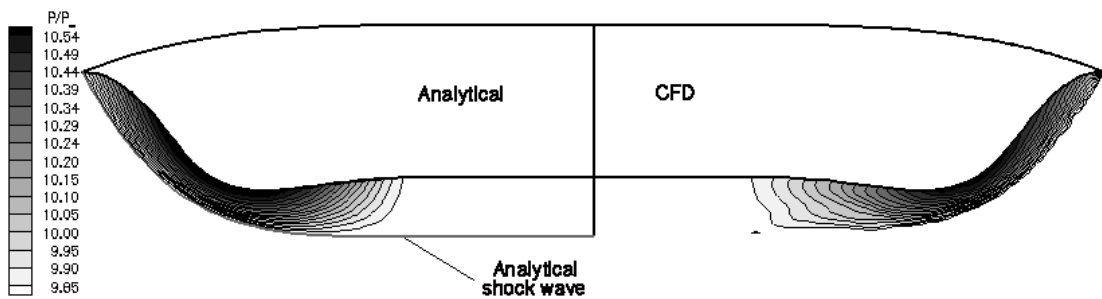


Fig. 3.36 Comparison of normalized pressure contours over Mach 10 non-modified waverider, base plane

The pressure contours in the base plane (see Fig. 3.35-3.36) match very closely, and the differences between the present osculating cones design method and previous design method are imperceptible.

The azimuthal velocity contours (see Fig. 3.37-3.38) show very similar results for both modified and non-modified waverider configurations. The shock wave from the CFD solution is matching its predicted analytical location, and is captured over a small distance.

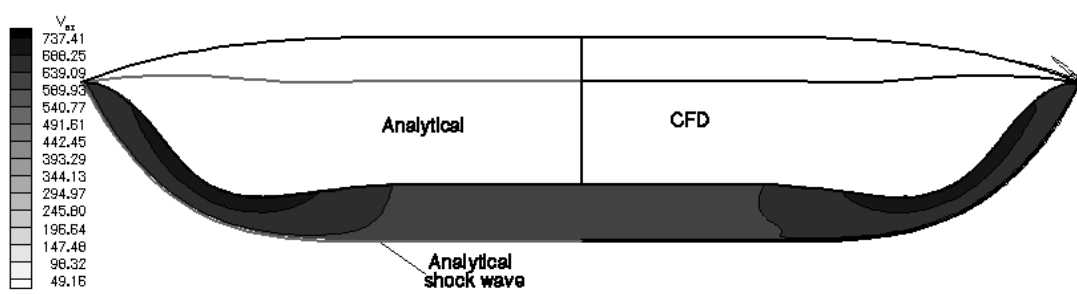


Fig. 3.37 Comparison of azimuthal velocity contours over Mach 10 modified waverider, base plane

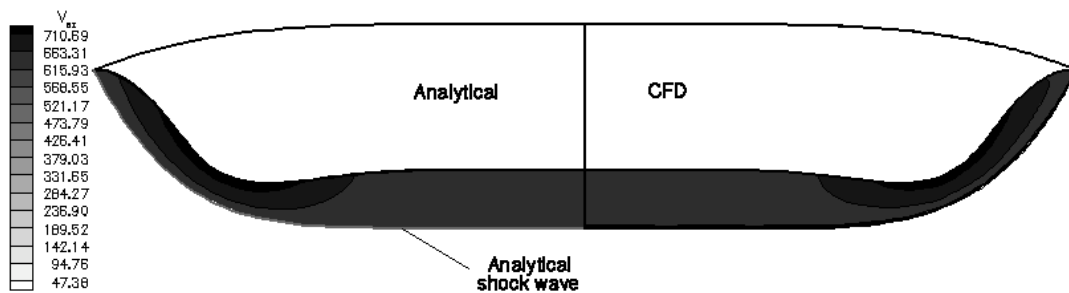


Fig. 3.38 Comparison of azimuthal velocity contours over Mach 10 non-modified waverider, base plane

From the comparison of the normalized pressure over the lower surface of the waveriders (see Fig. 3.39-3.40), it can be noticed that for the current design the flow is numerically dispersed right behind the shock wave. Most probably, there is some numerical dissipation in the CFD simulation which is the cause of those dispersions. However qualitatively, the flowfield distribution is very close to the analytical solution.

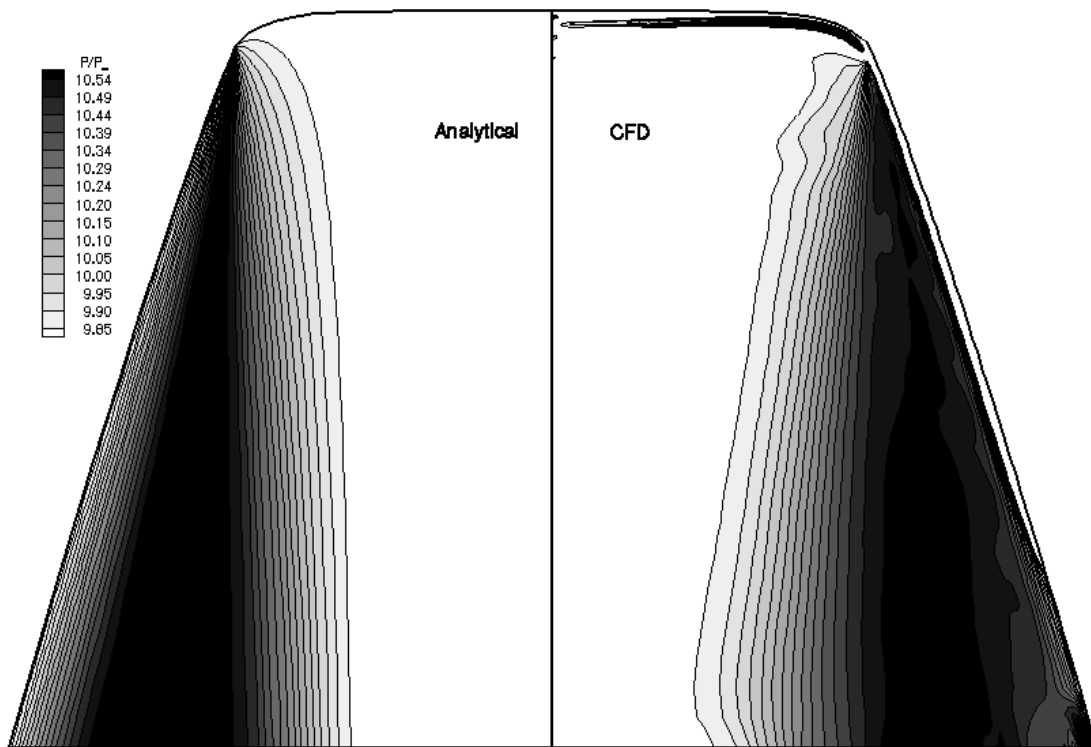


Fig. 3. 39 Comparison of normalized pressure contours over lower surface of Mach 10 modified waverider

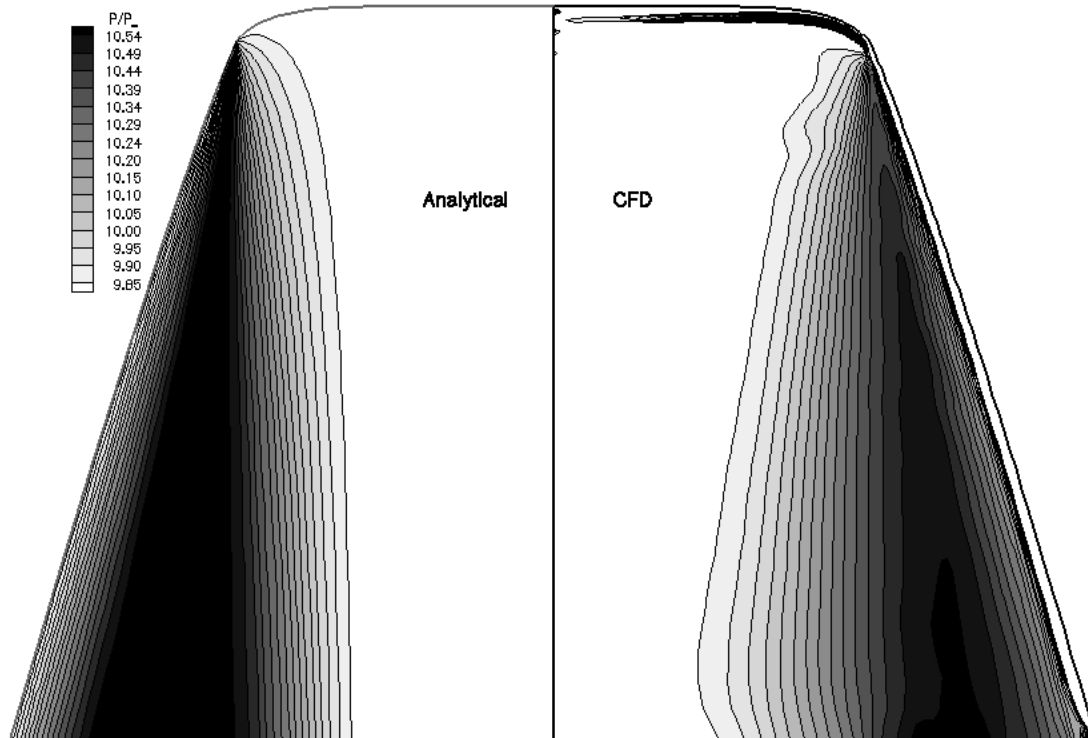


Fig. 3.40 Comparison of normalized pressure contours over lower surface of Mach 10 non-modified waverider

With such high Mach numbers, the magnitude of the azimuthal velocity is becoming small enough compared to the freestream direction velocity so that the flow is almost not deflected anymore outward the osculating planes. Indeed the streamlines do not present any perceptible differences between the two different waverider configurations presented in Fig. 3.41. Those results confirm the derivation of the waverider geometries presented in the previous chapter: the modified and non-modified configurations are almost geometrically similar.

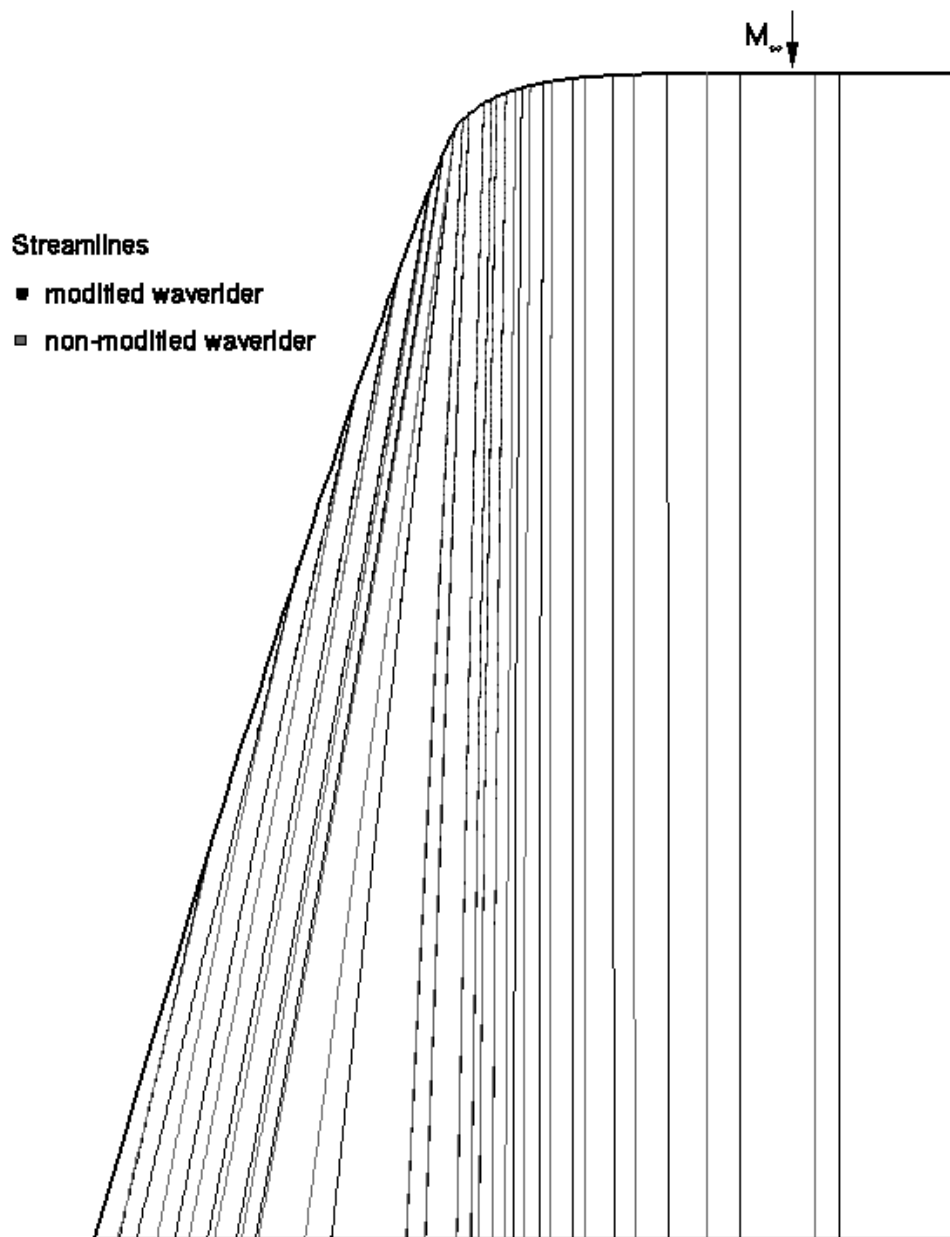


Fig. 3.41 Streamlines at the lower surface of a Mach 10 waverider

Aerodynamic Performance

Aerodynamic performance from the CFD simulation agrees very well for both configurations with the predicted performance (see Table 3.13). The differences observed previously between the flowfield distribution of the analytical solution and the Euler simulation do not have an impact on the integrated performance.

With this high Mach number osculating cones waverider configuration, the performance of the present design method is getting very close to the previous design methods (see Table 3.13-3.14). This is also a natural consequence of the similarity of the two geometries produced by the design code. (L/D agree within 0.3%).

Table 3.13 Aerodynamic performance of Mach 10 waverider with lower surface corrected for pressure gradients

	Design	CFD	% diff.
C_L	0.06204	0.06219	-0.229
C_D	0.01658	0.01661	-0.185
L/D	3.74258	3.74434	-0.047

Table 3.14 Aerodynamic performance of Mach 10 waverider with lower surface non-corrected for pressure gradients

	Design	CFD	% diff.
C_L	0.06204	0.06186	0.297
C_D	0.01652	0.01647	0.293
L/D	3.75625	3.75601	0.006

3.3.6 Osculating Cones Waverider M=15

Geometry Derivation

The two Mach 15 osculating cones waverider geometries (with and without pressure gradients corrections for the lower surface) derived by the design code at the following design conditions (see Table 3.15) were presented in Fig. 2.12.

Table 3.15 Design conditions of Mach 15 waverider

M	15.0
\square	17°
<i>Waverider Length</i>	5 m
<i>Flight Altitude</i>	35.14 km
P	252.412 Pa
T	253.009 K
U	4782.6 m.s ⁻¹

Flowfield Distribution

In the azimuthal direction the shock wave is well captured by the computational solution, as the shock is spread only over a small distance, and is attached to the entire leading edge of the geometry (see Fig. 3.42).

However, as for the Mach 10 osculating cones waveriders, some numerical dispersion from the analytical solution is observed in the CFD results for the portion of the flowfield located right after the shock wave. The pressure contours are dispersed, and a high-pressure region is appearing at the front part of the waverider.

Those discrepancies appear to increase with increasing Mach number, as the CFD-FASTRAN inviscid solver reaches its validity limit. This artificial numerical compression region enables the solver to process the high flowfield gradients associated with this high Mach number case.

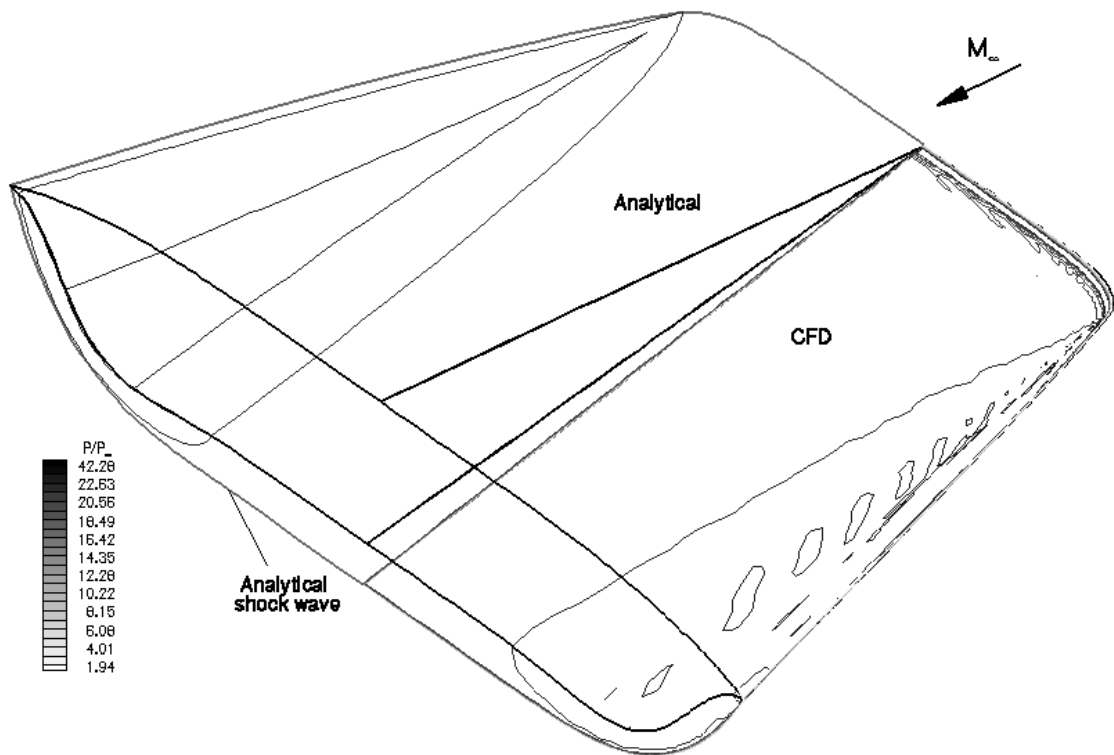


Fig. 3.42 Comparison of normalized pressure contours over Mach 15 waverider

In the base plane (Fig. 3.43-3.44), the normalized pressure contours agree perfectly between the analytical solution and the Euler simulation. From a vehicle integration standpoint, the CFD simulation confirms that at such high Mach number the osculating cones waverider design provide a uniform flow at the inlet of the engine.

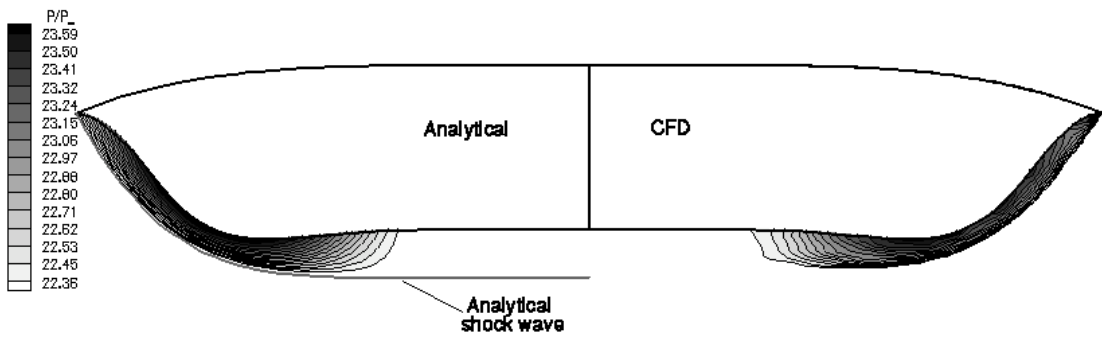


Fig. 3.43 Comparison of normalized pressure contours over Mach 15 modified waverider, base plane

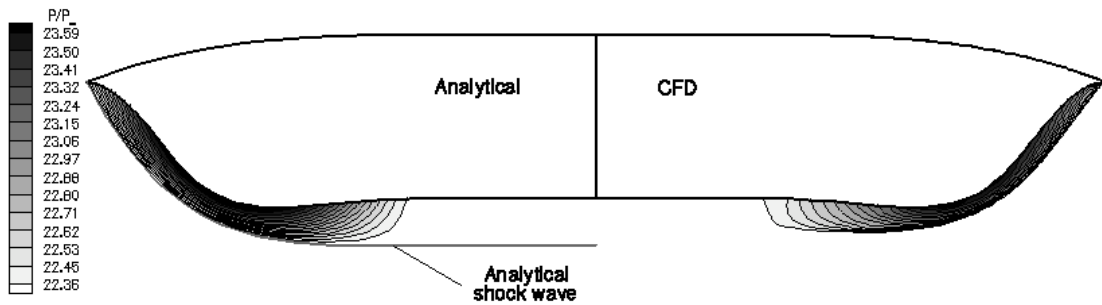


Fig. 3.44 Comparison of normalized pressure contours over Mach 15 non-modified waverider, base plane

As noted in Fig. 3.45-3.46, the CFD and the analytical technique produce the same flowfield distribution as for the azimuthal velocity. Also, those plots do not show any difference between the two different configurations (modified and non-modified).

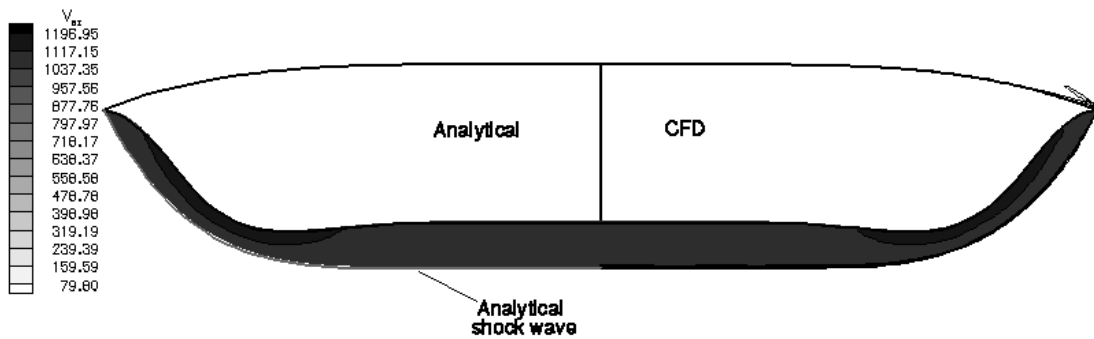


Fig. 3.45 Comparison of azimuthal velocity contours over Mach 15 modified waverider, base plane

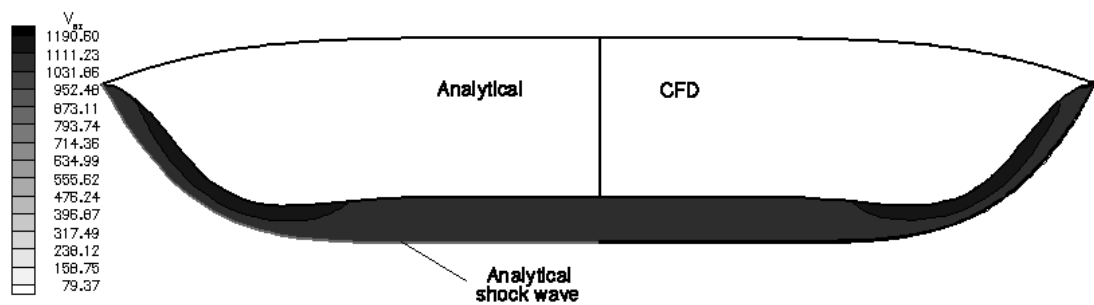


Fig. 3.46 Comparison of azimuthal velocity contours over Mach 15 non-modified waverider, base plane

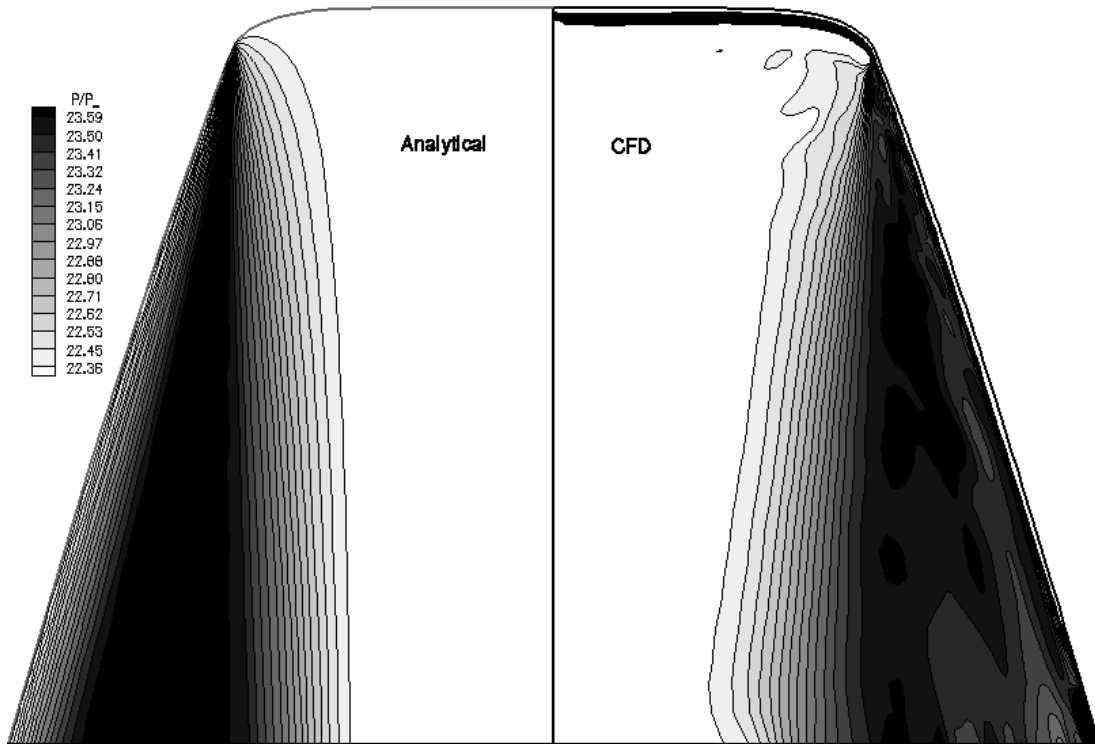


Fig. 3.47 Comparison of normalized pressure contours over lower surface of Mach 15 modified waverider

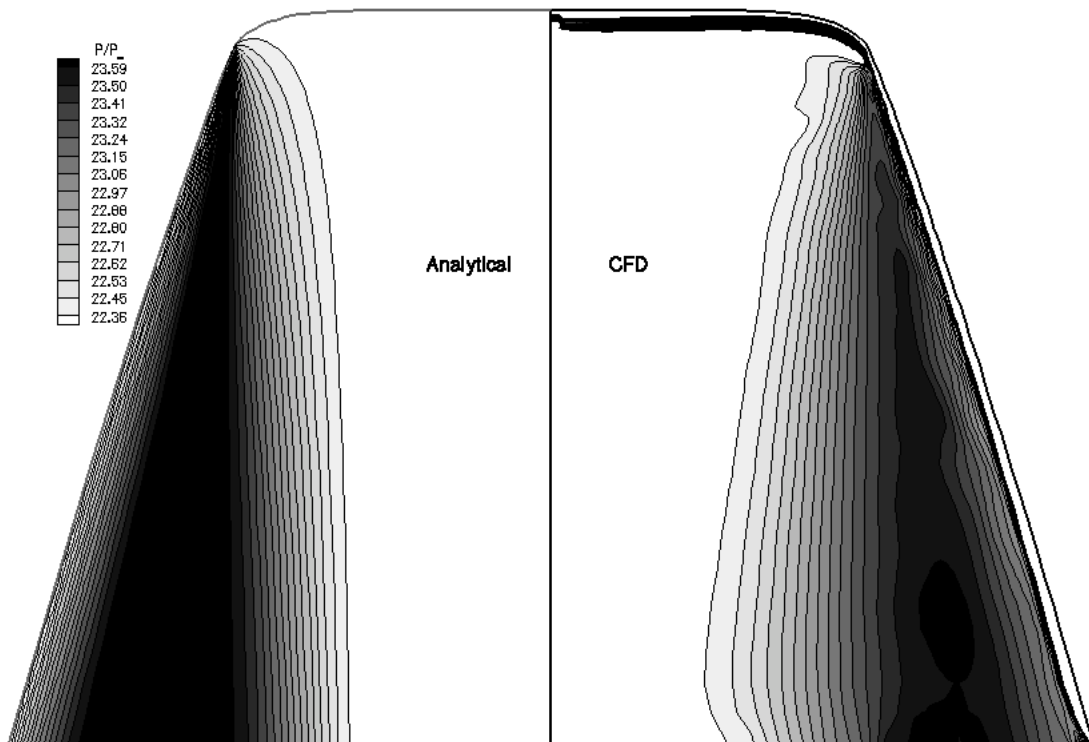


Fig. 3.48 Comparison of normalized pressure contours over lower surface of Mach 15 non-modified waverider

The lower surface normalized pressure distribution of the waveriders (see Fig. 3.47-3.48) agrees qualitatively well between the analytical solution and the CFD simulation. As pointed out before, the zone located close to the leading edge show numerical dispersion both for the present design and the previous design methods. A high-pressure region is also appearing in the Euler simulation at the front part of the vehicle.

Aerodynamic Performance

Aerodynamic performance from the Euler simulation agrees very well for both designs with the analytical predicted performance (see Table 3.16-3.17).

The two geometries generated by the two different design methods are almost similar, and consequently aerodynamic performance is close to being identical (L/D ratios agree within 0.03%).

Table 3.16 Aerodynamic performance of Mach 15 waverider with lower surface corrected for pressure gradients

	Design	CFD	% diff.
C_L	0.06603	0.06596	0.116
C_D	0.01786	0.01783	0.140
L/D	3.6975	3.69846	-0.026

Table 3.17 Aerodynamic performance of Mach 15 waverider with lower surface non-corrected for pressure gradients

	Design	CFD	% diff.
C_L	0.06603	0.06575	0.437
C_D	0.01782	0.01774	0.452
L/D	3.70597	3.7065	-0.014

Chapter 4

Summary and Conclusions

In the present work a new osculating cones waverider design technique has been developed. This method avoids assumptions made in the previous osculating cones waverider design methods. Previous techniques assumed that the cross-flow was minimal, so that the design was simplified by neglecting the azimuthal pressure gradients for the derivation of the generating flowfield of the waverider. This assumption uncouples the derivation of the flowfield within each of the spliced osculating cone stripe along the shock wave surface of the waverider. The present method integrates the azimuthal pressure gradients for the derivation of the flowfield of each conical stripe.

A design code was developed in order to derive waverider shapes following the present so-called “modified osculating cones waverider” technique. This tool was also to predict on-design aerodynamic performance. CFD simulations have been performed to validate the new design method, and also in order to map precisely the flowfield distribution around the waveriders.

A class of geometrically similar osculating cones waveriders (adapted for RBCC integration) has been derived with the modified osculating cones method. Overall, only small modifications were observed on the streamlines geometries, resulting in a moderate impact of the azimuthal pressure gradients corrections on the lower surface of the waveriders. For the most extreme configuration (waverider with on design Mach number of 3), the streamlines at the lower surface of the non-modified waverider present a deviation of several degrees from the streamlines of the modified waverider design, especially in the region of high azimuthal pressure gradients. Overall, for the different studied configurations, the modified waveriders

are quite similar to the waveriders derived with the previous osculating cones waverider method, with a decreasing effect of the modifications with increasing Mach number. This effect is characteristic of hypersonic flow for which the Mach number independency rules high Mach numbers flowfields. The differences between the corrected and non-corrected configurations are observed in the regions of high gradients of the shock wave curvature-, which are the regions of high-pressure gradients. As the Mach number increases the flow becomes predominated by the flow in the freestream direction, and the effect of azimuthal pressure gradients on the flowfield becomes minimal so that the streamlines tend to remain in their original osculating plane. From the comparison of the different geometries, it is concluded that above Mach 10 the azimuthal pressure gradients can be neglected without impacting the geometry of the waverider.

The Euler simulations have confirmed the predicted flowfield distribution and aerodynamic performance of the osculating cones waverider geometries for both previous and present design techniques. From the CFD results, it was observed that, contrary to previous waverider studies, the shock wave is captured accurately by the chosen computational method. The clustering of the computational grid at the predicted location of the shock wave enables the CFD code to seize, over a small distance, the high gradients in the flowfield variables associated with the shock. At low on-design Mach numbers, the CFD solution for the modified osculating cones waverider configuration matches qualitatively and quantitatively more closely the prescribed analytical flowfield than the CFD solution for the non-modified osculating cones waverider configuration. For all the CFD simulations run in that study, the normalized pressure contours are agreeing very closely to the prescribed pressure contours. Consequently the aerodynamic performance predicted by the design code and the aerodynamic performance calculated by the CFD code are matching very closely. However some discrepancies have been observed at high

Mach numbers, which is as a result of numerical dissipation happening because of the high gradients across the shock wave. Even considering those discrepancies, the present work has produced accurate CFD results for the waverider flowfield, and close agreement for the aerodynamic performance between CFD and the analytical solution. The streamlines tracing confirmed the trends observed for the derivation of the waverider geometries presented in that study. As a general rule, the geometry of the streamlines is not strongly affected by the azimuthal pressure gradients, even for extreme gradients cases. At high on-design Mach number (above 4-5), the magnitude of the deflection of the streamlines outward their original osculating planes is minimal.

In this study, both the geometry derivation from the design code, and the CFD simulations validate the assumption of negligible azimuthal pressure gradients at high hypersonic Mach numbers.

From a vehicle integration standpoint, this study has shown the influence of the azimuthal pressure gradients on the inlet plane flowfield distribution. At low Mach numbers, those gradients have to be taken into account since the flow entering the inlet will not be uniform.

As already mentioned before for high hypersonic Mach numbers this work has confirmed that the geometry of the streamlines were not perceptibly affected. The geometry of the lower surface of waveriders for such configurations is thus not strongly impacted by the corrections incorporated within the present osculating cones waverider design. This study has thus validated the assumption made for the previous osculating cones waverider method: the azimuthal pressure gradients along the waverider geometry are negligible at sufficiently high Mach number (over Mach 4-5). In particular, the waveriders designed in the framework of those previous studies are also validated.

Appendix A

Euler Equations

The steady three-dimensional Euler compressible equations can be written in the generalized coordinates and conservative form as:

$$\frac{\partial \hat{Q}}{\partial t} + \frac{\partial \hat{F}}{\partial \bar{x}} + \frac{\partial \hat{G}}{\partial \bar{y}} + \frac{\partial \hat{H}}{\partial \bar{z}} = 0$$

$$\hat{Q} = Q/J$$

$$\hat{F} = (\bar{x}F + \bar{y}G + \bar{z}H)/J$$

$$\hat{G} = (\bar{x}F + \bar{y}G + \bar{z}H)/J$$

$$\hat{H} = (\bar{x}F + \bar{y}G + \bar{z}H)/J$$

$$Q = \begin{bmatrix} \bar{\rho} \\ \bar{\rho} \bar{u} \\ \bar{\rho} \bar{v} \\ \bar{\rho} \bar{w} \\ \bar{e} \end{bmatrix} \quad F = \begin{bmatrix} \bar{\rho} \bar{u} \\ \bar{\rho} \bar{u}^2 + \bar{p} \\ \bar{\rho} \bar{u} \bar{v} \\ \bar{\rho} \bar{u} \bar{w} \\ (\bar{e} + \bar{p}) \bar{u} \end{bmatrix} \quad G = \begin{bmatrix} \bar{\rho} \bar{v} \\ \bar{\rho} \bar{v} \bar{u} \\ \bar{\rho} \bar{v}^2 + \bar{p} \\ \bar{\rho} \bar{v} \bar{w} \\ (\bar{e} + \bar{p}) \bar{v} \end{bmatrix} \quad H = \begin{bmatrix} \bar{\rho} \bar{w} \\ \bar{\rho} \bar{w} \bar{u} \\ \bar{\rho} \bar{w} \bar{v} \\ \bar{\rho} \bar{w}^2 + \bar{p} \\ (\bar{e} + \bar{p}) \bar{w} \end{bmatrix}$$

Where the primitive variables are non-dimensionalized as follows:

$$\bar{\rho} = \rho / \rho_0$$

$$\bar{u} = u / \sqrt{u^2 + v^2 + w^2}$$

$$\bar{e} = e / \left[\rho_0 \left(u^2 + v^2 + w^2 \right) \right]$$

$$\bar{v} = v / \sqrt{u^2 + v^2 + w^2}$$

$$\bar{p} = p / \left[\rho_0 \left(u^2 + v^2 + w^2 \right) \right]$$

$$\bar{w} = w / \sqrt{u^2 + v^2 + w^2}$$

$$\bar{x} = x / \text{length}$$

$$\bar{y} = y / \text{length}$$

$$\bar{z} = z / \text{length}$$

Bibliography

¹ O'Neil, M. K. L., and Lewis, M. J., "Design Tradeoffs on Scramjet Engine Integrated Hypersonic Waverider Vehicles ", *Journal of Aircraft*, Vol. 30, No. 6, 1993, pp. 943-952.

² Lobbia, M., and Suzuki, K., "Numerical Investigation of Waverider-Derived Hypersonic Transport Configurations", *AIAA Paper 2003-3804*, Jun. 2003.

³ Lewis, M. J., and McDonald, A. D., "Design of Hypersonic Waveriders for Aeroassisted Interplanetary Trajectories", *Journal of Spacecraft and Rockets*, Vol. 29, No. 5, 1992, pp. 653-660.

⁴ Strohmeyer, D., Eggers, T., and Haupt, M., "Waverider Aerodynamics and Preliminary Design for Two-Stage-to-Orbit Missions, Part 1", *Journal of Spacecraft and Rockets*, Vol. 35, No. 4, 1998, pp. 450-458.

⁵ Heinze, W., and Bardenhagen, A., "Waverider Aerodynamics and Preliminary Design for Two-Stage-to-Orbit Missions, Part 2", *Journal of Spacecraft and Rockets*, Vol. 35, No. 4, 1998, pp. 459-466.

⁶ Nonweiler, T.R.F., "Aerodynamic Problems of Manned Space Vehicles", *Journal of the Royal Aeronautical Society*, Vol. 63, pp. 521-528, 1959.

⁷ Nonweiler, T. R. F., "Delta Wings of Shape Amenable to Exact Shockwave Theory", *Journal of the Royal Aeronautical Society*, Vol. 67, p. 39, 1963.

⁸ Jones, J.G., "A method for Designing Lifting Configurations for High Supersonic Speeds Using the Flow Fields of Non-Lifting Cones", Royal Aircraft Establishment, Report 2674, Mar. 1963.

⁹ Rasmussen, M., "Waverider Configuration Derived from Inclined Circular and Elliptic Cones", *Journal of Spacecraft and Rockets*, Vol. 17, No. 6, 1980, pp. 537-545.

¹⁰ Bowcutt, K.G., Anderson, J.D., and Capriotti, D.P., "Viscous Optimized Hypersonic Waveriders", *AIAA Paper 87-0272*, Jan. 1987.

¹¹ Corda, S., and Anderson, J.D., "Viscous Optimized Hypersonic Waveriders Designed from Axisymmetric Flow Fields", *AIAA Paper 88-0369*, Jan. 1988.

¹² Takashima, N., and Lewis, M. J., "A Cone-Wedge Waverider Configuration for Engine-Airframe Integration", *Journal of Aircraft*, Vol. 32, No. 5, pp. 1142-1144, 1995.

¹³ Sobieczky, H., Dougherty, F., and Jones, K.D., "Hypersonic Waverider Design from Given Shock Waves", First International Hypersonic Waverider Symposium, University of Maryland, College Park, MD, Oct. 1990.

¹⁴ Takashima, N., *Optimization of Waverider-Based Hypersonic Vehicle Design*. PhD dissertation, Dept. of Aerospace Engineering, University of Maryland, 1997.

¹⁵ Yoon, B.-H., *Computational Analysis of Hypersonic Flow Past Elliptic-Cone Waveriders*. PhD dissertation, Dept. of Aerospace Engineering, University of Oklahoma, 1990.

¹⁶ Stecklein, G., and Hasen, G., "Numerical Solution of Inviscid Hypersonic Flow around a Conically-Derived Waverider", *AIAA Paper 92-0305*, Jan. 1993.

¹⁷ Lin, S.-C., and Shen, M.-C., "Navier-Stokes Simulation of a Cone-Derived Waverider with Multi-Directional Curvature", *AIAA Paper 96-0313*, 1996.

¹⁸ Cockrell, C. E., and Huebner, L. D., and Finley, D. B., "Aerodynamic Performance of and Flowfield Characteristics of Two Waverider-Derived Hypersonic Cruise Configurations", *AIAA Paper 95-0736*, 1995.

¹⁹ Lobbia, M., *A Framework for the Design and Optimization of Waverider-Derived Hypersonic Transport Configurations*. PhD dissertation, Dept. of Aeronautics and Astronautics, University of Tokyo, Feb. 2004.

²⁰ Miller, R.W., et al., "Experimental Verification of the Osculating Cones Method for Two Waverider Forebodies at Mach 4 and Mach 6", *AIAA Paper 98-0682*, Jan. 1998.

²¹ Graves, R.E., and Argrow, B.M., "Aerodynamic Performance of an Osculating-Cones Waverider at High Altitudes", *AIAA Paper 2001-2960*, Jun. 2001.

²² O'Brien, T.F., *RBCC Engine-Airframe Integration on an Osculating Cone Waverider Vehicle*. PhD dissertation, Dept. of Aerospace Engineering, University of Maryland, 2001.

²³ Rasmussen, M., *Hypersonic Flow*, John Wiley & Sons, Inc., New York, 1994.

²⁴ Anderson, J. D., *Modern Compressible Flow*, 2nd edition, McGraw-Hill, 1990.

²⁵ Center, K.B., Sobieczky, H. and Dougherty, F.C., "Interactive Design of Hypersonic Waverider Geometries", *AIAA Paper 91-1697*, Jun. 1991.

²⁶ Jones, K.D, Sobieczky, H., Seebass, A. R. and Dougherty, F.C., "Waverider Design for Generalized Shock Geometries", *Journal of Spacecraft and Rockets*, Vol. 32, No. 6, 1995, pp. 957-963.

²⁷ Jones, K.D., and Center, K.B., "Waverider Design Methods for Non-Conical Shock Geometries", *AIAA Paper 2002-3204*, Jun. 2002.

²⁸ *US Standard Atmosphere*, 1976, US Government Printing Office, Washington DC, 1976.

²⁹ CFD-FASTRAN User Manual, Version 2003, CFD Research Corporation, 2003.

³⁰ CFD-GEOM User Manual, Version 2003, CFD Research Corporation, 2003.